RF Spatial Combining and Field Control in Dielectric Media

by

Patrick Bluem

B.S., University of Colorado Boulder, 2014

M.S., University of Colorado Boulder, 2016

A thesis submitted to the

Faculty of the Graduate School of the

University of Colorado in partial fulfillment

of the requirements for the degree of

Doctor of Philosophy

Department of Electrical and Computer Engineering

2019

This thesis entitled:

RF Spatial Combining and Field Control in Dielectric Media

written by Patrick Bluem

has been approved for the Department of Electrical and Computer Engineering

_____

Zoya Popović

_____

Taylor Barton

Date _____

The final copy of this thesis has been examined by the signatories, and we find that both the content and the form meet acceptable presentation standards of scholarly work in the above mentioned discipline.

Bluem, Patrick (Ph.D., Electrical Engineering)

RF Spatial Combining and Field Control in Dielectric Media

Thesis directed by Professor Zoya Popović

Recent developments in higher static magnetic field MRIs have allowed for increased sensitivity and improved imaging compared to current clinical MRIs due to the inherent low SNR of nuclear magnetic resonance. Ultra-high field MRI promises to improve medical imaging technology with higher SNR, increased parallel imaging performance, and higher spectral dispersion. With the decrease in wavelength inside of the imaging volume, standing waves develop and decrease the high homogeneity required for accurate diagnosis of medical problems. Additionally, at higher operating frequencies the bore becomes a loaded waveguide which supports propagating modes.

This thesis focuses on the development of circularly polarized patch probes for traveling wave MRI at small-bore 16.4 T, wide-bore 7 T and 10.5 T systems with boundary modification structures to improve field coupling and homogeneity. The attenuation of the wave in the unloaded portion of the waveguide becomes an issue with available RF systems as the excitation is placed away from the imaging volume. Additionally, boundary modifying structures are developed to improve coupling and SNR inside of the imaging volume. These boundary modifying structures placed around the imaging volume can be relatively simple and provide an increase in field homogeneity. To improve the relatively poor received spatial coverage of the single patch probe, an additional array is developed with interdigitated capacitor probes at 10.5 T. Multiple excitations can be combined with various relative magnitude and phase excitations, known as B1 shimming. These two techniques can be combined to drastically increase the field coverage inside of an imaging volume. The techniques proposed for cavity excitations in MRIs can be translated to microwave heating systems that convert waste to carbon-rich fuel. Recent military interest in the development of waste-to-fuel techniques have used pyrolysis and incineration, however, these approaches are relatively large due to the necessary supporting infrastructure to operate them.

Dedication

To my parents Hans and Patricia Bluem, thank you for all of the support over the years.

Acknowledgments

I would like to thank Prof. Zoya Popović for giving me the opportunity and funding to attend graduate school. I am thankful for all of the guidance and knowledge she has provided throughout the course of my graduate education. I would also like to thank Dr. Pierre-Francois Van de Moortele and Dr. Gregor Adriany at the Center for Magnetic Resonance Research, University of Minnesota for all of the assistance with access to the scanners, imaging, and data processing. Without their help this Ph.D would not have been possible. I would like to thank Dr. Andrew Kiruluta at Harvard University for his help on the project. I would also like to thank my committee, Prof. Dejan Filipović, Prof. Taylor Barton, and Prof. Dimitra Psychogiou from the University of Colorado Boulder and Prof. Robert Caverly from Villanova University. I would like to thank NSF for funding the MRI research and DARPA for funding the research on microwave conversion of waste-to-fuel. To the past and present members of the RF & Microwave Research Group, thank you for the helpful discussions and for keeping the time in the lab enjoyable.

Contents

Appendices

List of Tables

List of Figures

Chapter 1

Introduction

Contents

1.1 Application Motivation

The research described in this thesis develops approaches to EM simulations and design of loaded overmoded waveguides and cavities as applied to ultra-high field magnetic resonance imaging (MRI) and microwave waste management. The two examples are illustrated in Fig. 1.1, showing an excitation scheme for an anatomically correct human body model and an example of a possible setup for a microwave heating system.

Since its invention in the 1970s and first medical usage in the 1980s, MRI has been a crucial diagnostic tool in medicine, used for a broad range of diagnostics, from analyzing blood flow to finding tumors. Typical clinical MRI uses 1.5 and 3 T superconducting electromagnets for the

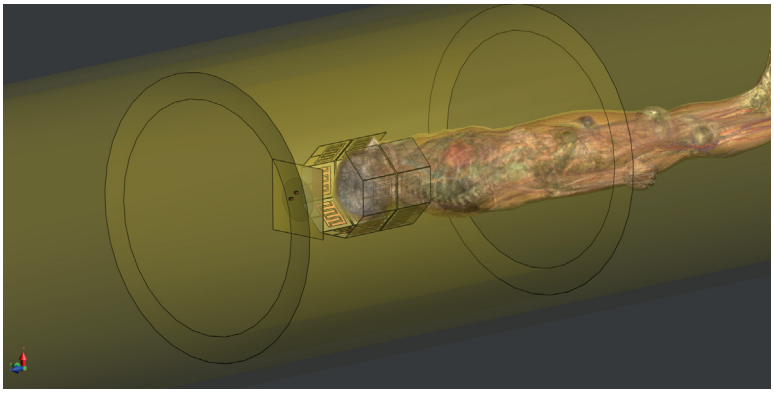

(a)

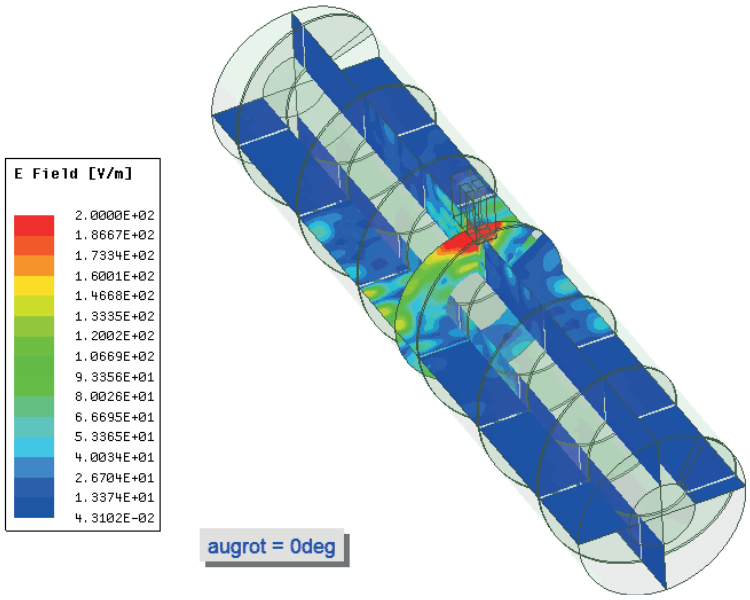

(b)

Figure 1.1: Example applications addressed in the thesis (a) anatomically correct human body model, *Duke*, in the simulated MRI setup and (b) possible example setup of a microwave waste to fuel conversion system with a rotating auger for field and material mixing.

static magnetic field. Large body coils are often used for the RF excitation with region-specific receive coils due to the low frequency required for clinical systems. In recent years, higher field systems have become of interest due to the inherent increase in SNR and improved parallel imaging performance. With the increase in static field, the necessary RF excitation frequency increases, Table 1.1 and standing waves develop in typical imaging volumes. The Larmor frequency is the RF frequency required to precess the spins of the atoms for nuclear magnetic resonance imaging, scaling linearly with B_0, the DC magnetic field. This RF excitation is known as B_1^+ and is a transverse circular polarized magnetic field, which will tip the spins a certain amount proportional to the applied field, known as flip angle.

Table 1.1: Larmor Frequencies at Various Field Strengths for H^1 Proton Imaging

DC Magnetic Field	Larmor Frequency
1.5 T	64 MHz
3 T	128 MHz
7 T	297 MHz
10.5 T	447 MHz
16.4 T	698 MHz

In this work, patch probes are designed to excite specific field distributions inside of a target volume, tailored to improve magnetic field uniformity and SNR for MRI. With lower field systems, magnetostatic theory can be used to design an excitation that produces a homogeneous field inside of an imaging volume. However, with high field systems, the excitation is determined by the modes supported by the waveguide created by the imaging volume. This thesis addresses multiple designs that help improve the fields excited in both phantoms and human body models using various methods, including multiple feeds that combine RF power in the imaging volume. For this work, measurements were taken at the Center for Magnetic Resonance Research (CMRR), University of Minnesota, Minneapolis, Minnesota.

Another use of spatial combining of fields inside of large dielectric medium inside of an electrically large structure is microwave heating. As the waste is heated the electrical and thermal properties change. For a closed loop adaptive system, these parameters need to be monitored to

maintain efficient and effective operation. The electric field is desired to be as uniform as possible in some cases and targeting specific areas in others. The field distribution can be varied by modifying the phase and magnitude of each excitation source using superposition. Depending on the geometry of the target volume, solely varying relative magnitudes and phasing might not result in sufficient control of the field distribution, and modification of the boundary conditions close to the cavity walls can used as an additional design parameter. One common use of a cavity modifier to improve the field distribution is a mode mixer in a microwave oven. This object turns on the top of the microwave oven to modify the boundary conditions along the wall, intending to improve the field distribution and improving the field uniformity food.

From supporting thousands of soldiers to a squad, waste management is a large concern. Logistically, waste takes up valuable space in a large encampment or base. For troops on the move, improper disposal of waste can be a safety concern where troops can be tracked. Currently, incineration is a popular method of waste disposal, however, these systems are generally very large and do not scale. On ships, this can involve burning expensive jet fuel and in the field, a simple fire. A microwave system can utilize different methods of power excitation, whether it is solid state amplifiers or a larger magnetron, and different cavity sizes to scale according to the need without leaving a trace. Additionally, the disposal can be controlled to improve heating times and duration to leave a valuable carbon rich fuel that could be used for various other applications. With a significant variation in waste material properties, proper microwave excitations can be challenging due to the anisotropy of the mixture and can lead to uneven or undesired excitations. With multiple excitations and material monitoring, this problem can be reduced or even alleviated.

The loaded bore waveguide (MRI) and loaded cavity (waste management) are simulated with full-wave EM commercial software. Primarily Ansys HFSS, a finite element modeling full-wave solver, is leveraged for 3D simulations of the various volumes. By using tetrahedrals with curvilinear edges, the models can be simulated with a high degree of accuracy, however, the necessary computational resources can become fairly high. Additionally, FEM requires the solving of a linear system of equations and matrix inversion and due to this, cannot be accelerated well. In order

to interface with an anatomically correct human body model, the simulation setup is shifted to Sim4Life, a finite-difference time-domain (FDTD) full-wave solver. FDTD requires the use of rectangular voxels to solve Maxwell's equations directly on a given grid. Using this method, matrix inversion is unnecessary and allows for GPU acceleration of the solver, drastically increasing the speed from 30 Mcells/s with a CPU to 2300 Mcells/s with a GPU.

1.2 Magnetic Resonance Imaging

1.2.1 Background

In the late 1940s, it was discovered that atomic nuclei can absorb weak radio frequency (RF) energy when its magnetic moment is oriented inside of a strong external magnetic field. This is referred to as Nuclear Magnetic Resonance (NMR) [1]. The nuclei will then rotate according to the Bloch equations, as follows,

$$\frac{d\vec{M}}{dt} = \gamma\vec{M} \times \vec{B} \tag{1.1}$$

$$\frac{d\vec{M}}{dt} = \gamma\vec{M} \times \vec{B}_{ext} + \frac{1}{T_1}(M_0 - M_z)\hat{z} - \frac{1}{T_2}\vec{M}_{\perp} \tag{1.2}$$

$$M_0 \simeq \frac{1}{4}\rho_0\frac{\gamma^2\hbar^2}{kT}B_0 \qquad (protons,\, \hbar\omega_0 \ll kT) \tag{1.3}$$

where γ (rad/(sT)) is the gyromagnetic ratio, $\vec{M}$ (A/m) is the net magnetization, B_{ext} (T) is the applied external magnetic field, M_0 (A/m) is the equilibrium magnetization, M_z (A/m) is the longitudinal magnetization, $\vec{M}_{\perp}$ (A/m) is the transverse magnetization, ρ_0 (N/m^3) is spin density (protons per unit volume), $\hbar$ (Js) is Planck's constant, k (J/K) is Boltzmann's constant, T (K) is temperature, and B_0 (T) is the static magnetic field. The atomic spins will orient themselves in the direction of the applied static magnetic field. These nuclei will resonate and precess at a frequency, known as Larmor Frequency, given by,

$$\omega = \gamma\, B_0 \qquad or \qquad f = \frac{\gamma}{2\pi} B_0 \tag{1.4}$$

Precession is defined as a rotating body spinning around a central axis. For NMR, this is the magnetic moment rotating around an external magnetic field, Fig. 1.2. The necessary excitation is a right-handed circular polarization commonly denoted B_1^+. The angle that the magnetization is tipped, or flipped, is known as flip angle. In the expanded Bloch equation (1.2), the nuclei will relax over two different time constants, T_1 (s), the spin-lattice relaxation, and T_2 (s), the spin-spin relaxation. In other words, T_1 is due to the proton wanting to reach its lowest energy state, naturally lying parallel to the external magnetic field. The interaction between protons will lead to local magnetic field variation and as such reduce the transverse magnetization over the time constant T_2. A more realistic value for the transverse relaxation is T_2^* and equal to,

$$\frac{1}{T_2^*} = \frac{1}{T_2} + \gamma \Delta B_0 \tag{1.5}$$

and in a perfect system, this will be equal to T_2. Due to inhomogeneities in the static magnetic field, the relaxation is generally less than the ideal, natural value. The consequence of this varying relaxation rate is a dephasing of the magnetic spins, however, it can also be leveraged for different types of imaging, such as functional MRI.

In the early 1970s, it was discovered that NMR could be applied to medicine due to the different relaxation times of tissues and tumors [2] as shown in the expanded Bloch equation in (1.2). Further, if a spatially varying magnetic field is applied to an imaging volume instead of a constant, static magnetic field, a RF pulse can be used to create a spatially varying NMR excitation. This spatially varying excitation allows for a 3D slice selection, and thus diagnostic Nuclear Magnetic Resonance Imaging (NMRI) was born [3] and later Lauterbur and Mansfield co-won the Nobel Prize in 2003.

The imaging of hydrogen (H^1) protons has been a key fundamental in MRI, where $\frac{\gamma}{2\pi}$=42.58 MHz/T, due to the abundance of water molecules inside of tissues. The low resulting energy due to the precession of the atomic spins associated with MRI results in a low signal-to-noise ratio (SNR),

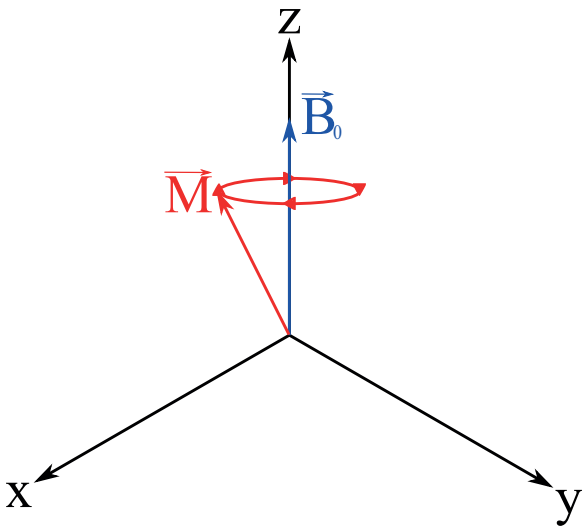

Figure 1.2: Simple representation of the Bloch equation showing longitudinal and transverse magnetization and precession around the static magnetic field, B_0.

reducing the overall contrast and resolution that can be obtained in MR images. The amplitude of the signal received,

$$signal \propto \frac{\gamma^3 B_0^2 \rho_0}{T} \tag{1.6}$$

is shown to be proportional to the gyromagnetic ratio, DC magnetic field, spin density ρ_0, and temperature. Furthermore, the SNR can be shown to be equal to [4],

$$SNR = \frac{\kappa\gamma^2 B_0^2}{\gamma\sqrt{B_0^2 + 3B_{0,low}^{3/2}\sqrt{B_0}}} \approx \kappa\gamma B_0 \tag{1.7}$$

where κ is a system scaling factor from a low-field system, $B_{0,low}$, where the electronics dominate the noise. Thus, the SNR can increase linearly with the static field. The overall increase in SNR allows for the increase in spatial resolution due to the ability to create higher field gradients, contrast-to-noise ratio, and parallel imaging performance. However, the increase comes at a high cost, impacting both safety and homogeneity of the magnetic field. The possible induced voltage due to movement can be larger ($emf = -\frac{\partial \vec{B}}{\partial t}$), leading to safety concerns with patients and technicians. Additionally, while SNR increases due to B_0 increase, the frequency does as well as shown in Table 1.2. The wavelength inside of a water volume ($\varepsilon_r = 81$) decreases from 52 cm at 1.5 T to 7.5 cm at

Table 1.2: Larmor Frequencies at Various Field Strengths for H^1 Proton Imaging

DC Magnetic Field	Larmor Frequency
1.5 T	64 MHz
3 T	128 MHz
7 T	297 MHz
10.5 T	447 MHz
16.4 T	698 MHz

10.5T and even further to 4.8 cm at 16.4 T, creating standing waves inside of any imaging volume larger than the wavelength.

In MRI, clinical images are formatted as a black and white image in the Digital Imaging and Communications in Medicine (DICOM) format. This format is a linear scale of post-processed data from any pulse sequencing. Two pulse sequences used in this research are the gradient recalled echo (GRE) and absolute flip angle imaging (AFI). The GRE sequence is popular as it uses the gradient coil to re-orient the spins instead of waiting for the magnetization to naturally decay, resulting in quicker imaging. Flip angle is the amount the applied transmit RF pulse is able to rotate the spin,

$$\alpha = \gamma B_1 t_p \tag{1.8}$$

where t_p is the pulse duration. The absolute flip angle imaging sequence is useful to measure the transmit efficiency of the RF excitation. The DICOM image is typically a multiplication of both of the transmit and receive profile of the RF excitation. In order to properly compare the experiments to the simulations, the efficiency ($\mu T/\sqrt{W}$) needs to be calculated using the AFI sequence to separate the transmit from the receive profile. The images are typically aligned in 3 plane cuts, the sagittal (typically YZ-plane), coronal (typically XZ-plane), and the axial (typically XY-plane) as shown in reference to a human in Fig. 1.3.

In order to characterize the system, various phantoms can be used for different effects. A phantom is an object used as stand-in for organic tissue to characterize the operation of systems for imaging. The simplest, and used in the majority of this thesis, is a cylindrical bottle phantom, Fig. 1.4a. This phantom is usually filled with de-ionized (DI) water, creating a worst case scenario

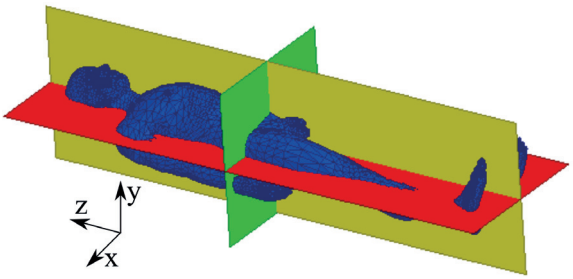

Figure 1.3: Plane definitions for sagittal (yellow), coronal (red), and axial (green) cross-sections.

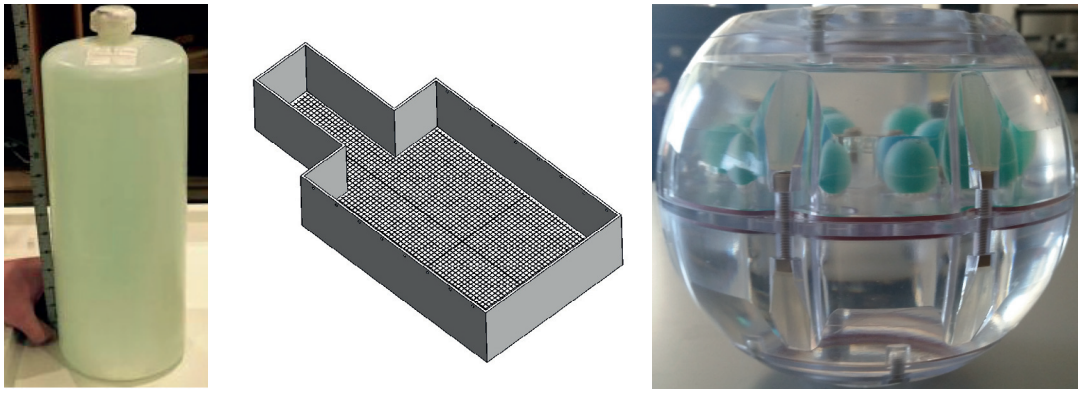

(a) (b) (c)

Figure 1.4: (a) Large bottle phantom, (b) ASTM 2182 phantom, and (c) NIST system phantom.

of excitation inhomogeneities due to its simplicity. The ASTM 2182 phantom, Fig. 1.4b, is a tetrahedral representation of a human head and torso generally filled with a gel to represent human biological tissues. This phantom is primarily used for characterization and compliance of passive and active implantable medical devices. The last type of phantom is a complex system phantom, e.g. Fig. 1.4c, composed of different shapes to characterize a system for a given form factor. Some examples are large spheres or breast shapes composed of many layers of various materials to measure various parameters such as distortions, inhomogeneities, and T_1 and T_2 weightings.

1.2.2 Clinical MRI

There are 5 main components of an MR scanner: the static magnet, gradient coil, patient table, computer control, and RF coil. The static magnet provides the B_0 as discussed previously. Its role is to orient the proton spins longitudinally, typically the Z-axis. The gradient coil serves the same

role at all field magnitudes. Its purpose is to shift the field slightly so there is no longer an isotropic B_0, but a $B_{ext}(X, Y, Z)$ to allow for slice selection. This also allows for quicker imaging as protons not localized to the current slice do not precess at the same angle and will reach a relaxed state faster, or never actually deviate from the relaxed state. The patient table is movable to allow a patient or imaging volume to be moved into the magnet and imaging region placed iso-center of the magnet. The computer controls the whole system as shown in the simplified block diagram Fig. 1.5a. This portion is a complex combination of frequency synthesizers, analog to digital and digital to analog converters, RF drive, power circuitry, magnet controls to improve the static field homogeneity, and complex processing in order to view the medical images. The last component and the focus of this thesis is the RF coil/excitation. In reality, there will be multiple coils and multiple excitations that must be accounted for. Often there is a not a single corporate feed for all components in order to allow for relative phasing between elements to account for changes in imaging volumes. The relative magnitude and phasing between elements of the transmit is known as B_1 shimming. This is similar to the concept of B_0 shimming which is done to homogenize the static field for a given imaging region. Currently, this is typically done electronically with coils, however, classically this was done with metal shims to passively alter the field. The latter portions of this thesis will focus heavily on the topic of B_1 shimming to homogenize the RF excitation.

In low field MRI the bore and excitation can be considered as a quasistatic system due to the low frequency RF excitation required at 1.5 and 3 T. Often, large bird cage body coils, Fig. 1.5b, are integrated inside of a scanner under a plastic cover Fig. 1.5c. These are typically used in transmit only applications, due to the distance from the imaging volume, with region specific receive coils placed closer to the target volume [4,6–8]. With smaller region specific coils, such as head and knee birdcage coils, the coil can be operated in both a transmit and receive fashion. This requires a fast high power transmit receive (T/R) switch to separate the power amplifier and low noise amplifier. Power amplifiers for MRI are typically in the kilowatt range, and high isolation is needed between the transmit chain and the high sensitivity low noise amplifier. Simultaneous transmit and receive would improve performance, however, magnet-based circulators cannot be used.

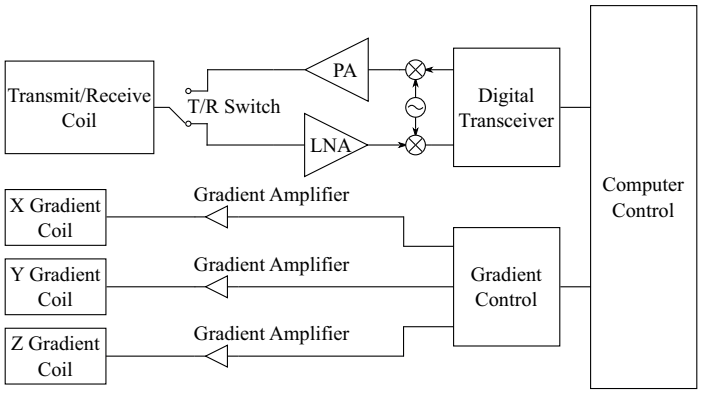

(a)

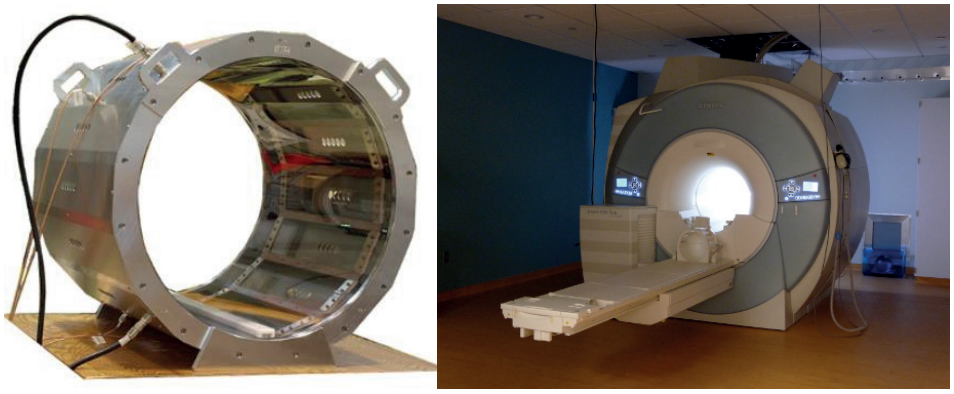

(b) (c)

Figure 1.5: (a) Simplified block diagram of the MR excitation using a T/R coil. (b) Typical low field birdcage body coil [5]. (c) Clinical 3T MRI at the Center for Magnetic Resonance Research.

1.2.3 Ultra-High Field MRI

The motivations for using high DC magnetic flux density ($B_0 > 3\,\mathrm{T}$) include increased SNR [9], allowing for improved spatial resolution [10], [11], better parallel imaging performance and potential for improved contrast [12]. With the increase in static magnetic field, small-bore MRIs, with internal diameters as small as 4 cm, have been primarily used for small-animal research and spectroscopy. Additionally, as superconductor technology improves and the desire for higher-field wide-bore systems increases, increasingly higher field systems are created. In 1999, the first 7 T MRI was installed with a 90 cm diameter bore. A few years later, 9.4 T machines would continue the research, however, much of the focus remained on 7 T. 7 T would become integral for pre-clinical research, targeting mainly the head. In 2017, the FDA cleared the first 7 T MRI to be installed for

clinical use [13]. The highest field, wide-bore system currently operational is a 10.5 T MRI, and in December 2017, the first human was imaged with this system.

The wide-bore, ultra-high field MRI becomes an over-moded waveguide when loaded with a high dielectric imaging volume. The decrease in wavelength causes standing waves to form inside of the imaging volume, resulting in a change in methodology for RF coil design. Lower field systems, and lower field excitations, can utilize a quasi-static approximation to design large, capacitive bird-cage coils Fig. 1.5b. These whole body coils can be useful for exciting a given segment of the imaging volume, but must be tuned according to the loading. Often, receive specific coils are used to pick up the small field response over a targeted region of interest. However, this approach is only valid when the wavelength is significantly larger than the volume.

As the static field increases, the excitations become smaller and require a different design. Current 7 T transmit schemes include dipoles [14], combination of the two with magnetic wall filters [15], microstrip radiators such as in Fig. 1.6 [16–18], standard patch antennas [19–22], and coaxial waveguide [23]. The shorter wavelength at 10.5 T results in a smaller excitation probe that can be matched to the loaded bore. For improved spatial coverage in ultra-high field systems, microstrip arrays (e.g. [17]) replace the quasi-static bird cage excitation of lower field systems. A few different methodologies have been used for microstrip radiator arrays. Simple straight parallel microstrip lines are not effective, since the B-field generated is not balanced across the whole line. One method to improve the uniformity across the line uses a trapezoidal shape [16] to tailor the field to be uniform across the line. A high degree of isolation is also desired between elements, which is typically achieved with decoupling networks using lumped capacitors and inductors [24], however, this technique can lead to a large separation between elements or small component values at high fields that may not be realizable. Another method to improve coupling to the imaging volume is adding more elements, however, the close proximity of elements reduces isolation. [17] alternates between first and second harmonic microstrip elements to increase the number of elements to 16, with a simultaneous increase in the number of elements and the isolation. With array-like excitations, a high degree of isolation is challenging to obtain due to the close proximity of the

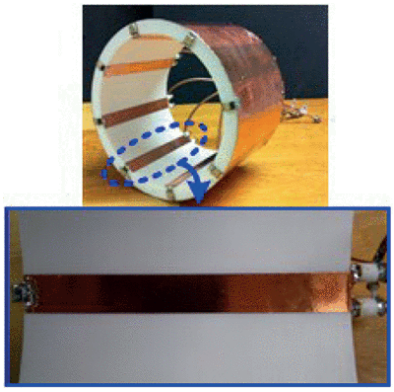

Figure 1.6: Shielded microstrip array for 7 T head imaging at the Center for Magnetic Resonance Research [16]

elements. However, element design can be chosen to reduce the near-field $\vec{E}$ in the lateral direction towards other elements. The decrease in wavelength at 10.5 T assists in this effort with a 3 dB lower coupling coefficient at the closest possible spacing compared to 7 T [25]. A reduction in the $\vec{E}$ is additionally critical to reduce the absorbed electric field, or specific absorption rate (SAR), in the imaging volume. The overall power absorbed is limited by the IEC 60601-2-33 standard where the averaged peak spatial SAR of constant-mass 10 g volumes must not exceed 3.2 W/kg. Any power in the electric field will be lost transmit efficiency and result in the reduction of image quality. This is also critical with medical implants inside of patients where an induced electric field will cause localized heating around the implant and burn the patient.

NMR can also be excited and detected using long-range coupling with traveling waves, demonstrated by several research groups over the past few years, e.g. [20]. One benefit of this approach is more uniform coverage of samples that are larger than the wavelength of the NMR signal as shown in Fig. 1.7a. For small volumes, like a human leg, traveling MRI can be useful and have reasonable homogeneity. Unfortunately, as the volume expands, such as the chest phantom in Fig. 1.7b, homogeneity is poor, but the coverage is still high.

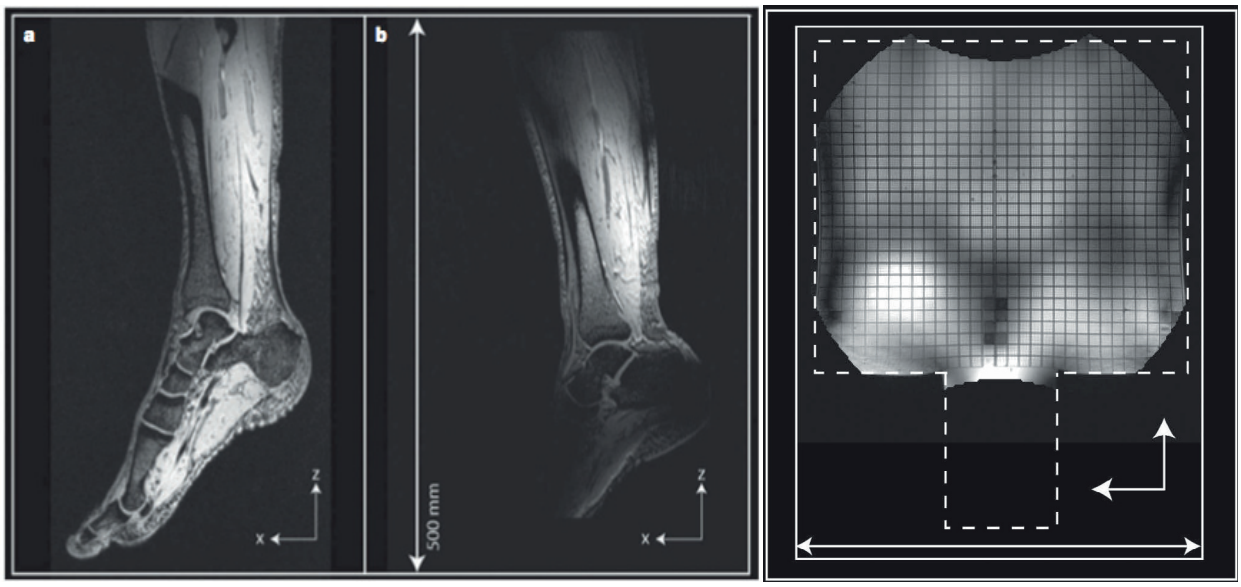

(a) (b)

Figure 1.7: Traveling wave MRI demonstrated by [20]

1.2.4 Traveling-Wave MRI

Traveling-wave MRI has been successfully demonstrated at various field strengths, including wide-bore 7 T and 9.4 T [20, 26–28] and small-bore animal 16 T and 21.1 T systems [29]. Current clinical machines and small-bore systems do not support traveling waves unless high dielectric inserts [30] or coaxial transmission lines [31] are added for mode propagation. The addition of dielectric loading [23, 32, 33] or multiple excitations [21] can be used in ultra-high field systems to help improve homogeneity, however, these solutions can be large and heavy. One of the largest issues with traveling-wave MRI is that the circular polarized probe is both the transmit and the receiving element. As the atoms radiate their energy isotropically, the low spatial distribution of the receive probes results in a significant loss of energy.

With the increase in field-strength, the necessity for high resolution, accurate modeling becomes more apparent. With work pioneered by [34] and [35], accurate human body models are being developed by several research institutions. One such institution is IT'IS in Zürich, Switzerland that develops a whole Virtual Population of 10 human body models with over 300 bones and

tissues modeled to an accuracy of 0.5x0.5x0.5 mm^3 [36]. An accurate body model is critical for engineers to design excitations such that the field as homogenized as possible for the lowest specific absorption rate (SAR) possible. For MRI, the typical quantity explored is a peak spatial SAR averaging over 10 g cubes (psSAR10g) according to the IEC 60601-2-33.

This thesis focuses on fixing the inhomogeneity of the B_1 RF excitation inside of the imaging volume using unconventional excitations. As previously described, the excitations for ultra-high field systems are focused towards near-field microstrip or dipole elements placed on top of or very close to the imaging volume. The proximity of the elements to the imaging volume will increase the coupling and transmit efficiency, but limits the effect of additional boundary structures to modify the field distribution inside of the volume. Larger, microstrip patch-based probes resembling more traditional antennas are implemented farther away from the imaging volume to observe the effect of larger traveling wave patch elements. The use of a traveling-wave probe can still create a balanced current distribution across the patch which is critical for improving homogeneity.

The geometric barrel distortions shown in the DICOM and efficiency plots and black speckles in the efficiency plots are other hardware and software issues that are not addressed in this thesis as they are fixed with different systems, such as B_0 shimming and post-processing.

1.3 Microwave Heating

1.3.1 Coking

Heating coal in an oven at 1000° creates what is known as metallurgical coke, which is composed primarily of carbon and is used as a fuel in high-volume applications such as smelting iron. The process of heating coal, known as coking, emits ammonia, carbon monoxide, hydrogen sulfide, hydrogen cyanide, sulfur oxides, and nitrogen oxides [37]. Historical "beehive" ovens, Fig. 1.8, used some of these gases to continue the combustion process while venting the rest through a chimney. These have been primarily replaced by by-product coke ovens which re-direct these gases to another process for reuse [38]. Similarly, oil can be heated to high temperatures to create petroleum coke.

Figure 1.8: Historic beehive coke ovens from the 19th century built by Osgood in Redstone, Colorado.

In 2010, the US alone had the capability to produce 129,000 tons of coke per day [39]. Coke can also be used to synthesize gases, such as syngas, a synthetic gas that can increase the efficiency of electricity generation due to its decreased lower heating value (120 btu/scf) compared to natural gas (950 btu/scf) [40]. Syngas can be converted using the Fischer-Tropsch process to a stable hydrogen-rich wax to be used in hydrogen fuel cells [41]. While coke is typically made from coal or oil, other plentiful carbon-rich sources, such as wood, can be used to generate coke and charcoal and reduce the CO2 emissions compared to burning coal [42]. This process can be extended to waste management as a significant portion of trash contains carbon, however, the coke yield will most likely be reduced. Instead of incinerating waste, useful by-products can be created for re-use with this controlled process and harmful emissions can be well controlled in a contained microwave cavity.

1.3.2 Military Waste Management

Current methods for waste management in the military depend on the type of waste and platform. For example, the US Navy is permitted to throw certain materials overboard ships [43], [44], e.g. paper rags, glass, metal, food when further than 12 nautical miles from land, ground-up food waste when further than 3 nautical miles from shore (Marpol Annex V for guidelines [45]). Usually, garbage is compressed into pucks, e.g. on the USS John C. Stennis Aircraft Carrier (as of 2011),

which "...processes approximately 100,000 lbs of plastic, 300,000 lbs of processed metal and glass, and 200,000 lbs of cardboard per month while out to sea. All of this combined is enough to equal to the weight of approximately 100 elephants" [46]. To eliminate the waste, metal/glass are shredded and dumped, plastics are melted into disks, and food remains are processed and then shredded and dumped. Cardboard is stored and recycled. An incinerator using JP-5 jet fuel is used for paper, rags and wood, wasting weight and cost related to burning jet fuel to dispose of garbage. In the case of US Navy submarines, all possible waste is eliminated prior to deployment, while on-board waste is "pumped out against the ambient sea pressure or blown out using pressurized air" [47], posing a security risk. Additionally, [47] states that "if this waste cannot be eliminated and has to be stored under Annex V, storage in the frozen food lockers appears to be the only solution."

The US Army uses BWEC (battalion-scale waste-to-energy conversion) GEM (green energy machine), which is large-scale gasification at a volume of 3 tons a day [48] which in turn uses 100 gross kW of power, with 26 kW needed to operate. This type of facility is large, battalion scale. The US Army has invested in pyrolysis (QinetiQ PyTEC system) [49] that can process 100 kg of waste per hour and "creates 25 liters of inert 'char' for every 100 kg of solid waste", contained in two 20-foot shipping containers. This is a large solution, the size of a shipping container or greater, and according to [50], a significant drawback to using this technology is being able to provide propane burners that will heat air or water or make electricity.

Other methods are burial in the field, or incineration [51]. An incinerator method referred to as TGER (tactical garbage-to-energy refinery) is being developed jointly between RDECOM, Defense Life Sciences LLC of McLean, Virginia, and a researcher team from Purdue University. Bowen Engineering Co. from Indianapolis supplied engineering and much of the equipment assembly, and Community Power Corp. in Littleton, Colorado, provided the gasifier [52]. The TGER system is a hybrid design that uses thermal gasification to produce synthetic gas, or syngas, from paper, ammunition wrappers, Styrofoam and plastic garbage, and a fermentation process to produce ethanol from a mixed waste stream of food slop and juice waste. TGER can handle nearly a ton of garbage daily and effectively run a 60 kilowatt (kW) generator. The system takes six hours to reach full

power, running on diesel during that time, and using less diesel fuel as it is brought to full power until it is down to 5 percent-from 5 gallons hourly to 1 gallon. The other 95 percent of the energy it produces comes from the waste. This concept has a goal similar to the one proposed here, but uses incineration to produce syngas, with significant radiated heat in the process. According to the Army, it is difficult to scale down, and is the size of a moving van, capable of producing one ton of useful fuel per day.

1.3.3 The Microwave Oven

Dr. Spencer from Raytheon holds the 1950 patent on the microwave oven (submitted in 1946) [53], invented when working with a magnetron and noticed that the candy in his pocket had melted. The first design used two cavity magnetrons mounted in parallel in a metallic waveguide. Raytheon demonstrated the first commercial microwave oven "Radarange" very soon after Spencer's discovery, it was 1.8 m tall, 750 lbs, and had an output power of 1.6 kW using a water-cooled permanent-magnet. The first counter top oven was developed in 1967 at a 10x reduced cost compared to the $5000 necessary to buy the Radarange. With further developments in magnetron technology, microwave ovens became standard kitchen appliances by the 1980s. This new technology found its place in chemistry, in ashing [54], wood processing [55], separation of pyrite from coal [56], and various other drying and cooking applications. Small low-power solid-state ovens are now being commercialized (Wayvtech), and semiconductor manufacturers (NXP, Infineon) are providing packaged transistors specifically for microwave cooking/heating.

Although commercial microwave ovens have been in production for nearly 70 years, off-the-shelf ovens are plagued by uneven heating. In microwave ovens, electrically large objects cause high order modes to develop, resulting in areas of concentrated electric field and as such, higher SAR. Unlike in convection ovens, with the proposed excitation systems, homogeneous heating can be improved over time as the electrical properties change during cooking. With microwave heating, the stable hydrogen-rich wax shown in [41] can be decomposed into hydrogen gases through catalytic cracking and fuel hydrogen cars. Current microwave ovens use 60-70% efficient magnetrons to excite

a roughly 1.5 ft^3 cavity. To improve the heating of the food, a rotating plate moves the item around the volume while a mode stirrer, such as the one shown in [57], modifies the boundary conditions of the cavity and shifts the modal content excited by a waveguide horn. New approaches using high power solid state amplifiers enable greater control of the modal content inside of the cavity by shifting the excited frequency and relative phasing between multiple excitations. CarbonScape, a New Zealand based company, introduced the concept of microwave coking in 2008 to create environmentally friendly "green coke", activated carbon "biochar", and contribute released gases towards bio-fuels, pharmaceutical applications, and creation of syngas or water treatment [58]. A factor that needs to also be taken into account is that microwave ovens have to meet leakage safety standards defined by the Center for Devices and Radiological Health (CDRH) of the US FDA, with a maximum power density of 1 mW/cm^2 at a distance of 5 cm from the exterior of the microwave oven [59].

In the last part of the thesis, modified microwave-oven cavities are proposed for converting carbon-rich waste to fuel.

1.4 Content and Contributions

Chapters 2-4 focus on three different ultra-high field systems, imaging a dielectric water-based phantom of $\varepsilon_r = 81$ and $\sigma_d = 0.4$ S/m. Chapter 2 presents initial research, focusing on a simple circular polarized, circular patch probe for exciting a traveling wave in a 16.4 T small-bore MRI. Due to the size limitations of the bore, a standard quadrature-fed circular patch probe could not fit inside of the region under the gradient coil. As such, an electrically small patch is developed along with additional electromagnetic boundaries to improve the coupling to the dielectric phantom. Chapter 3 expands on lessons learned and develops a excitation scheme for a wide-bore 7 T MRI. The electromagnetic boundary concept is further explored as more options are available due to the larger diameter bore. Computational questions are answered on what needs to be simulated for an accurate result. Lastly, for MRI, Chapter 4 explores the highest wide-bore magnet on the market,

the 10.5 T MRI. An additional array excitation is developed to improve on the spatial distribution of the receive elements. The work here is a culmination of all of the research for previous systems on water-phantoms, and with confidence due to experimental validation, different excitations and boundary structures are applied to an anatomically accurate human body model, *Duke* [36].

Chapter 5, introduces the use of overmoded microwave cavities for converting waste to carbon-rich fuel by heating using penetration depth of low microwave frequencies, e.g. 915 MHz and 2.45 GHz. Simulations are presented for loaded cavities similar to ones in the previous chapters, with the goal of maximizing absorption quantified by SAR. It is shown by using multiple phased probes, uniform and controlled field distribution can be obtained.

Chapter 6 presents a summary of the thesis and its contributions and directions for future work.

Chapter 2

Traveling-Wave Excitation for 16.4 T Small-Bore MRI

Contents

2.1 Experimental Setup

Experiments in this chapter are done at the Center for Magnetic Resonance Research (CMRR) at the University of Minnesota, Minneapolis, Minnesota. The small-bore setup in Fig. 2.1 shows the relevant dimensions and the position of the water phantom and patch probe. The total length of the 16.4 T superconducting magnet and bore is 332 cm, not drawn to scale in Fig. 2.1b. The gradient coil part of the bore is smaller in diameter than the outer part, the diameters being 12 cm and

(a)

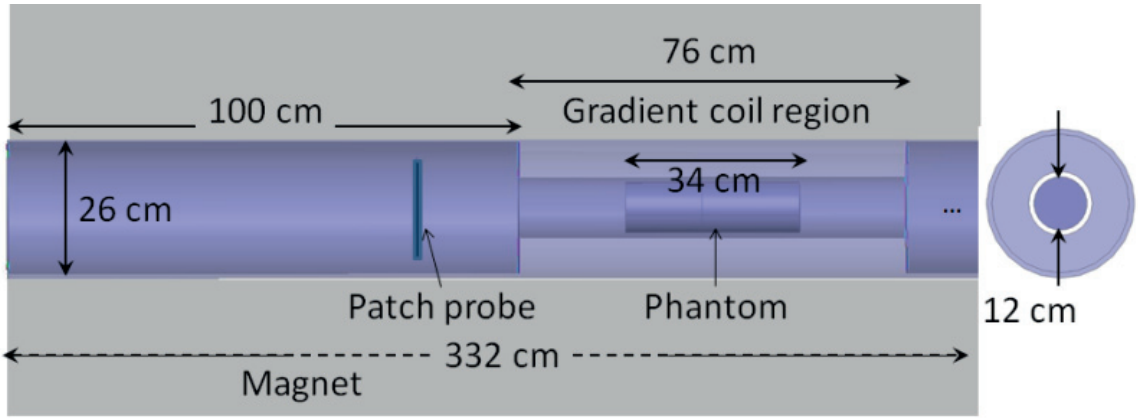

(b)

Figure 2.1: (a) Picture of the 16.4 T small-bore Varian Research MRI. (b)Sketch of 16.T small bore MRI with relevant dimensions and position of phantom shown. The traveling wave probe position can be varied inside the wider cylinder to demonstrate exposure and detection without near-field coupling. The entire magnet length is not shown for clarity, the total length being 3.32 m.

26 cm, respectively. The larger cylindrical portion to the left where the probe is placed is 100 cm long, and a similar 138 cm long portion is to the right of the gradient coil region. The inside wall of the bore is insulated. The water phantom is 34 cm long and fits snuggly in the smaller cylindrical part of the bore. The probe can be translated through the bore, which results in a change in matching, as well as variations in the excitation field in the phantom. It is fed by a 300 W power amplifier at the Larmor frequency of 698 MHz.

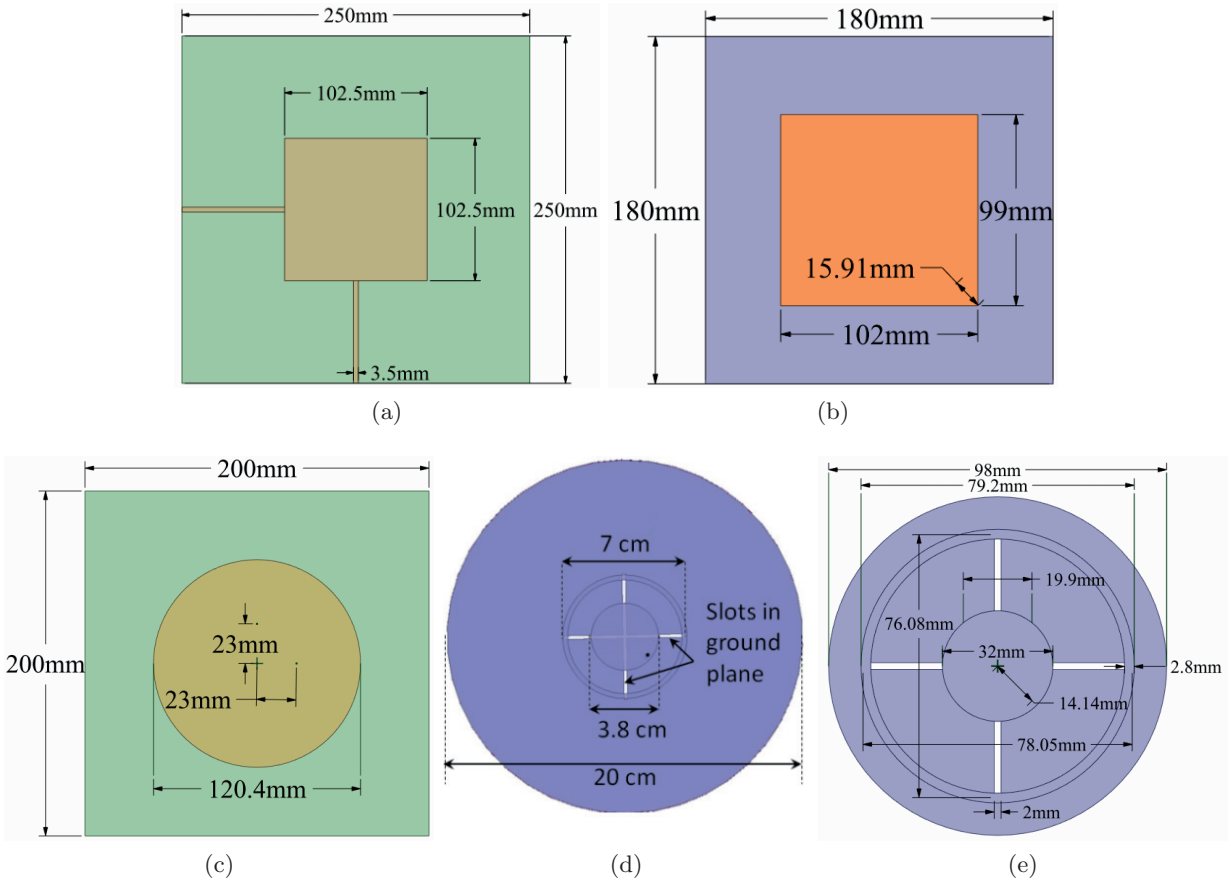

Figure 2.2: (a) Edge-fed square patch, (b) single coaxially fed rectangular patch, (c) quadrature fed coaxially fed circular patch, (d) annular ring circular patch version 1, and (e) annular ring circular patch version 2 probes for the 16.4 T small-bore MRI.

2.2 Probe Design

Due to the physically small size of the area under the gradient coil, electrically small probes must be developed. The diameter under the gradient coil is only $0.28\lambda_0$, reducing the possible probe designs. The one critical characteristic necessary of the RF probe is the ability to transmit the circular polarization necessary for the RF excitation. A few probes tested for the small-bore operation are shown in Fig. 2.2.

These probes are all designed on 62.5 mil FR-4 (ϵ_r=4.4) for operation at 698 MHz and their current distributions shown in Fig. 2.4-2.9. The figures show the current on the radiating surfaces of the patch as the phase of the input source advances over 180°. The current density should create

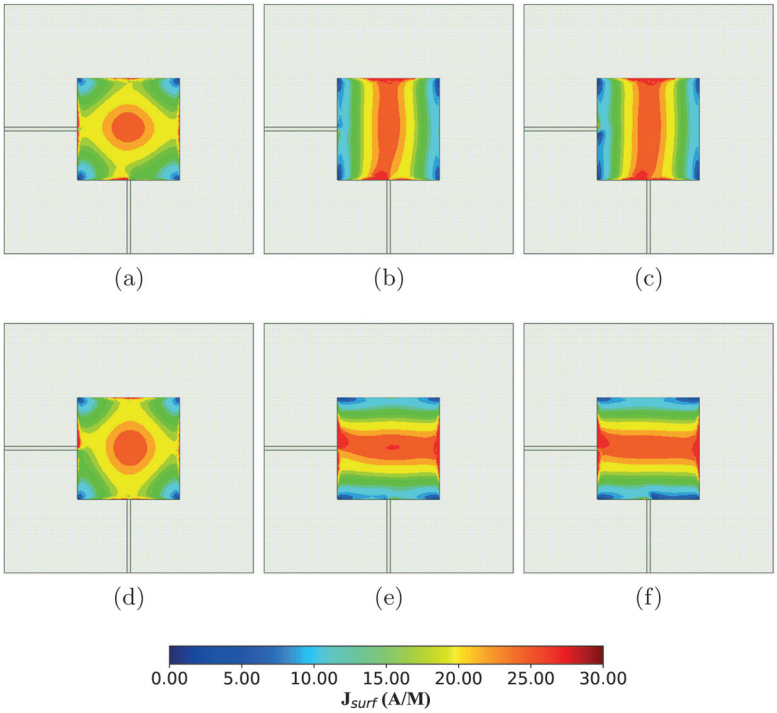

Figure 2.3: Magnitude of the current density on the edge-fed patch probe, Fig. 2.2a, as the phase advances from 0 (a) to 150 (f) degrees with a step size of 30°.

a circular polarization in the far-field if they operated as a patch antenna. The patches designed cannot be viewed as a classical antenna as they operate in a near-field condition inside of a metal pipe. Unfortunately, many patches found in literature are designed for far-field usage and at the core of the operation of the patch is a quadrature dipole operation. The vertically and horizontally polarized fields combine in the far-field to create a circular polarization, but will only create a distinct vertical and horizontal field in the near field as shown in Fig. 2.3, 2.7, 2.9. By using a single coaxial feed, Fig. 2.4, the currents become slightly circular, but the fundamental issue is the square geometry of the patch. The quadrature-fed circular patch, Fig. 2.5, remedies the issue of the circular current excitation, however, the patch is too large to fit inside of the small-diameter gradient coil.

Most electrically small patches rely on capacitively loading the currents on the patch by creating slots or simply adding capacitors. This exacerbates the non-circular nature of the current for rectangular patches and begins to disturb the currents on a circular patch. As such, many electri-

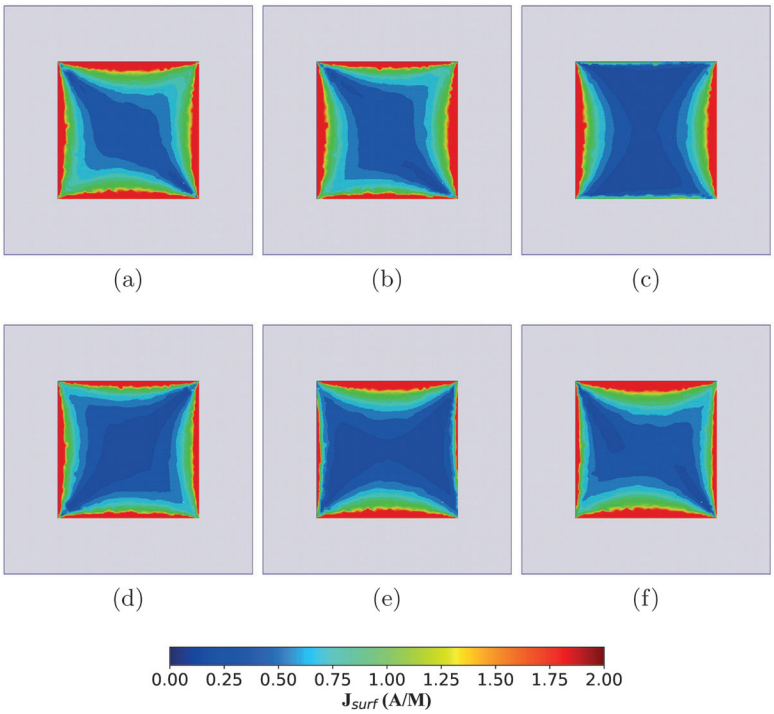

Figure 2.4: Magnitude of the current density on the single coax-fed patch probe, Fig. 2.2b, as the phase advances from 0 (a) to 150 (f) degrees with a step size of 30°.

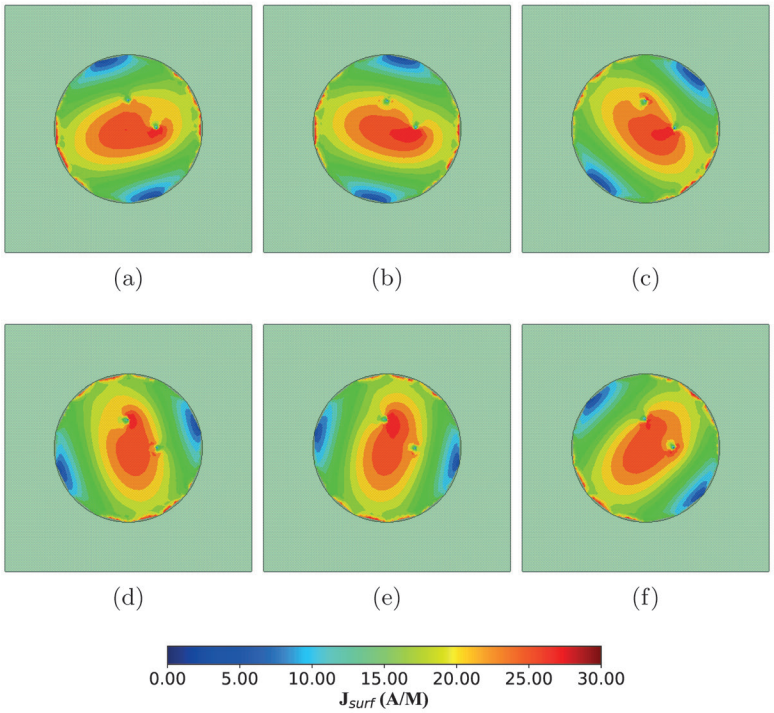

Figure 2.5: Magnitude of the current density on the quadrature fed circular patch probe, Fig. 2.2c, as the phase advances from 0 (a) to 150 (f) degrees with a step size of 30°.

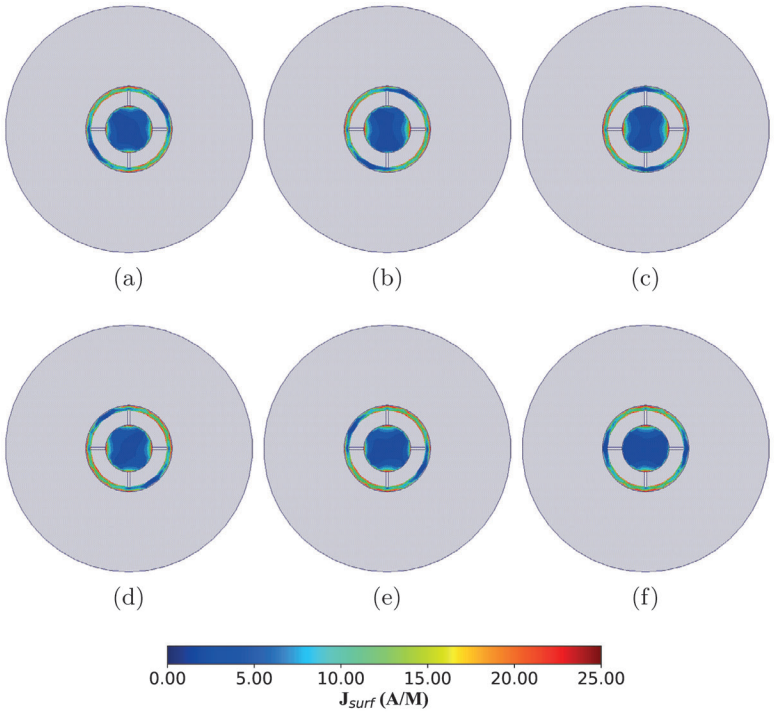

Figure 2.6: Magnitude of the current density on the top copper version 1 annular ring circular patch probe as the phase advances from 0 (a) to 150 (f) degrees with a step size of 30°.

cally small circularly polarized patches designed for small hand-held applications, such as [60], are unusable for the MRI application. The annular ring patch, on the other hand, creates an elliptical current density on the top radiating surface with a larger, Fig. 2.6, and smaller, Fig. 2.8, patch. The elliptical current density is due to the quadrature-fed dipole-like current density on the ground plane, Fig. 2.7 and 2.9.

Fig. 2.10 shows a comparison of the simulated magnetic field inside the phantom for the probe-fed rectangular patch, Fig. 2.2b, and annular ring patch, Fig. 2.2d probes. The simulations are performed for similar conditions as in the experiment. The simulations imply that the magnetic field profile is relatively independent of the type of probe that is chosen, as waveguide theory suggests. However, the location of the probe will influence the field distribution. The rectangular probe has a disadvantage because of its size, and the reduced size of the circular probe is a result of significant design efforts. In contrast to the rectangular patch probe, the circular probe is small enough and can fit in the gradient coil portion of the bore, and can also be scaled to fit inside 3 T,

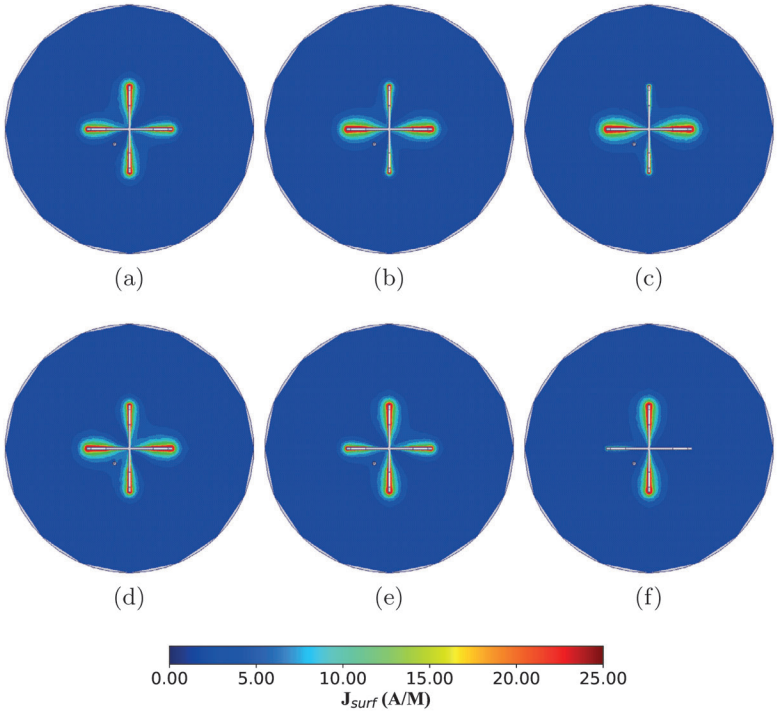

Figure 2.7: Magnitude of the current density on the ground copper version 1 annular ring circular patch probe as the phase advances from 0 (a) to 150 (f) degrees with a step size of 30°.

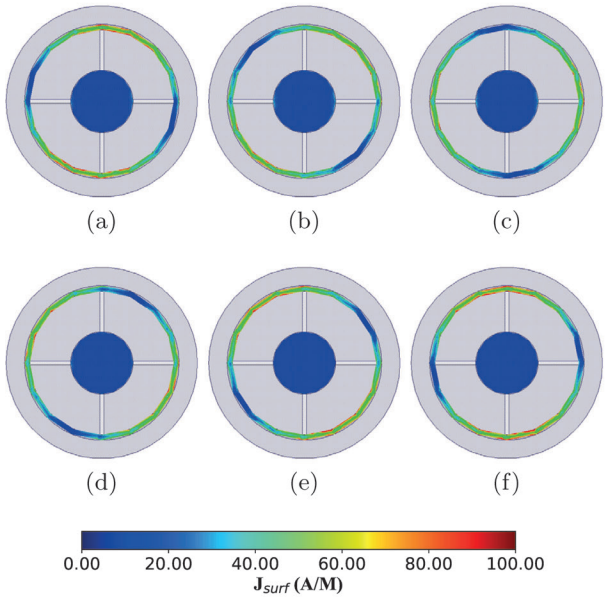

Figure 2.8: Magnitude of the current density on the top copper version 2 annular ring circular patch probe as the phase advances from 0 (a) to 150 (f) degrees with a step size of 30°.

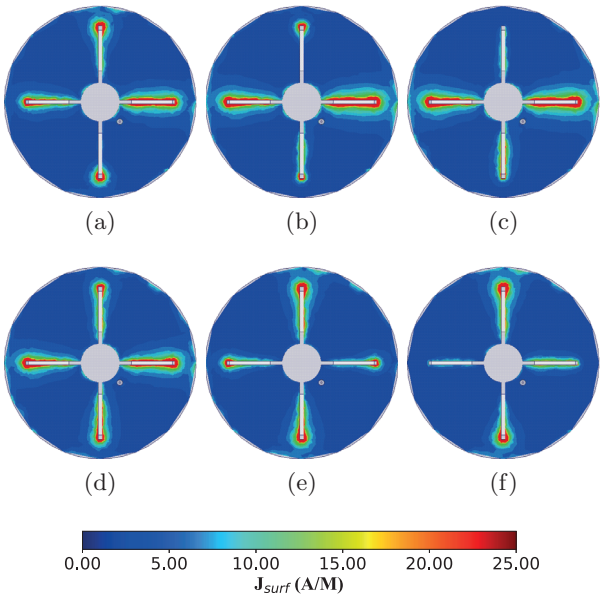

Figure 2.9: Magnitude of the current density on the ground copper version 2 annular ring circular patch probe as the phase advances from 0 (a) to 150 (f) degrees with a step size of 30°.

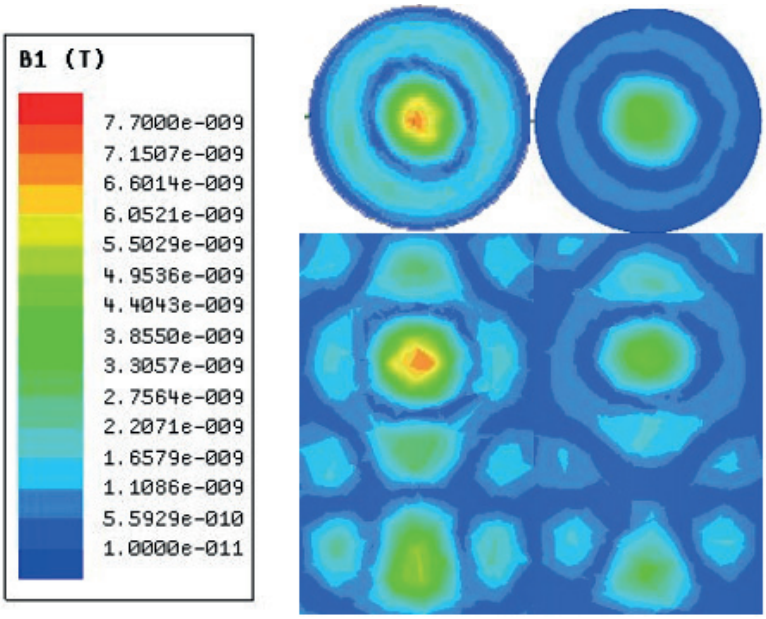

Figure 2.10: Magnitude of the transverse right handed circular-polarized B- field normalized to 1 W power input at the SMA connector of the probe for axial (top) and sagittal (bottom) simulated for the circular patch (left) and the rectangular patch (right) in HFSS.

7 T and 10 T static field MRI systems.

The probe designed for 16.4 T experiments is a single-coaxial feed slotted patch with an annular ring, Fig. 2.11. The slots on the back are centered on the patch with slightly different lengths. This results in a quadrature-fed dipole-like current on the ground plane which forces a circular current on the annular ring. This configuration allows for a 33% reduction in overall size compared to the circular and square patches. Unfortunately, this does allow the patch to radiate in both directions in free space, however, the large high dielectric constant volume inside of the bore will alter the performance and draw the fields toward the volume. For this reason, the probes must be designed using full-wave simulations (Ansoft HFSS), with the bore and phantoms taken into account. The electrically small, circular patch is designed with both a larger ground plane, Fig. 2.2d, and small ground plane, Fig. 2.2e to accommodate both the sizing of the larger diameter bore and the smaller diameter gradient coil. With the reduction in ground plane size, a circular region is cutout from the small diameter patch ground plane to improve the match of the probe. This does have a small effect on the current along the annular ring, creating a more elliptical polarization.

The phantom is simulated as a uniform dielectric cylinder with ε_r=81 and a conductivity of 0.4 S/m. The substrate is an FR4 62.5 mil thick double-sided copper printed circuit board. The patch feed is a single coaxial input as shown in Fig. 2.11, and the two 5- mm wide slots in the ground plane are 6.85 and 7.1 cm long and excite circularly-polarized waves [61].

2.3 16.4 T Long Phantom

The measured and simulated return loss, calibrated to the coaxial feed reference plane, is shown in Fig. 2.12. The patch itself had about 8 dB return loss, so a narrowband microstrip matching circuit is designed to obtain a return loss greater than 20 dB when the probe is placed in the bore. The simulations model the inside of a metal cylinder the size of the bore, and the distance to the gradient coil portion is varied to verify the traveling wave conditions. Coupling of the circularly-polarized field into the phantom is also examined in simulations by observing the transverse components of

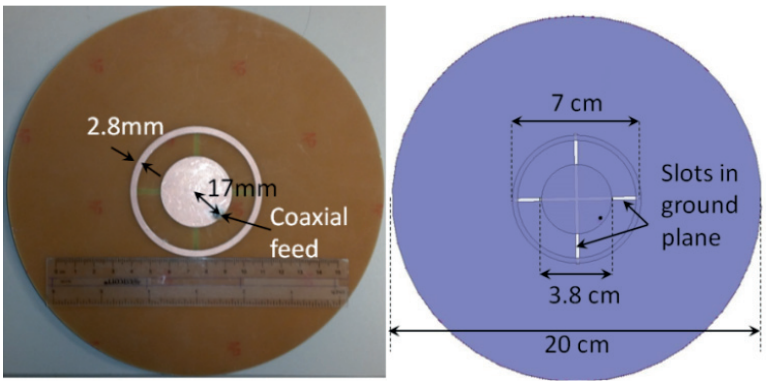

(a) (b)

Figure 2.11: (a) Photograph and (b) layout of circularly-polarized patch probe with a single coaxial feed and two slots in the ground plane that ensure circular polarization.

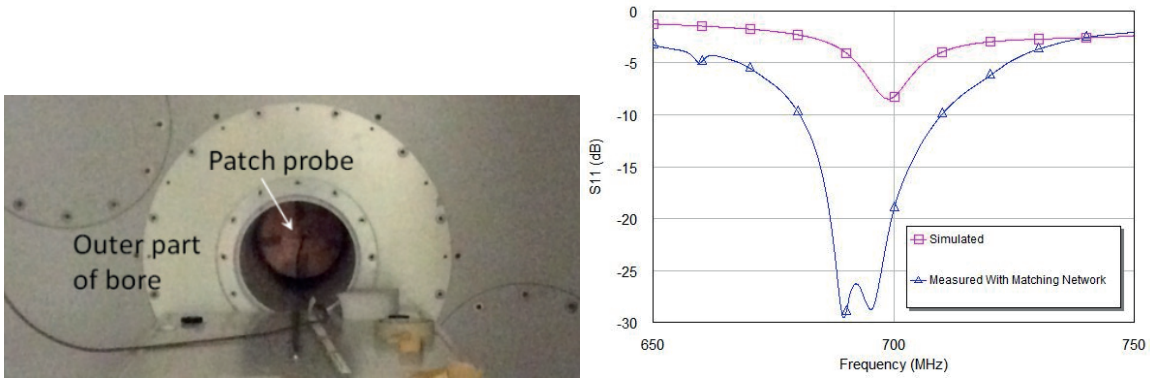

(a) (b)

Figure 2.12: (a) Photo of patch probe placed 50 cm into the bore. (b) Simulated return loss of the patch probe when placed inside the bore without a matching circuit (red) and measured return loss in the bore with an electrically short high-impedance line microstrip matching circuit connected between the coaxial cable and patch feed point.

the B-field.

The phantom used for the experiments is a dielectric acrylic tube (L=34 cm, D=9 cm) filled with deionized water or saline. Experimental results for two different coils can be seen in Fig. 2.14. Fig. 2.14a shows a measured result for a capacitively loaded near-field coil, Fig. 2.13b with high SNR around the edge, but a significant lack of field in the center of the phantom. With the patch probe placed 50 cm into the bore, as in Fig. 2.14b, MR images consistent with simulated B-field are obtained and are shown in Fig. 2.14c. The SNR of the traveling-wave excitation is poor due to

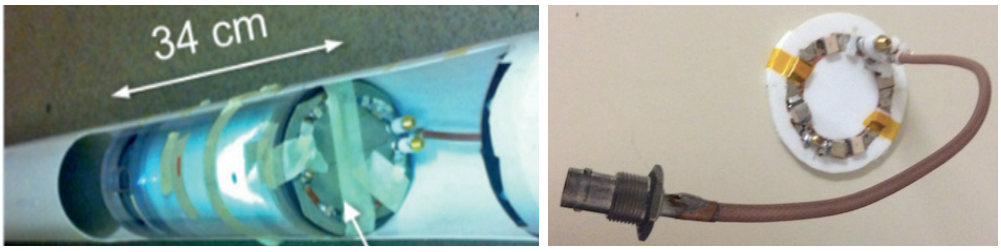

(a) (b)

Figure 2.13: (a) Dielectric phantom of length 34 cm and diameter 9 cm used for experiments. (b) Loop coil designed at CMRR for 16.4 T imaging.

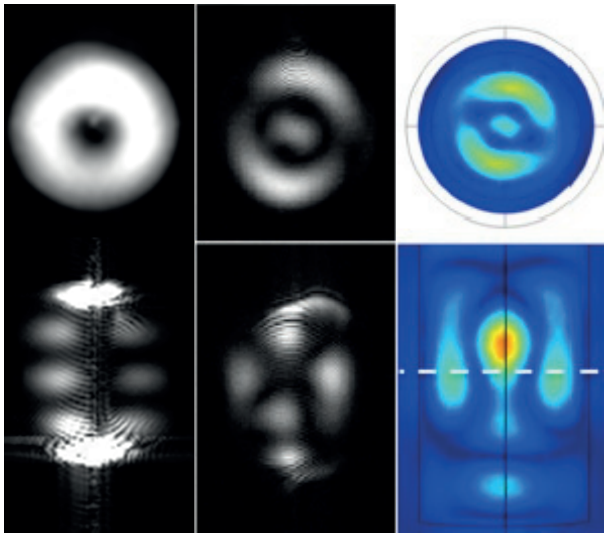

(a) (b) (c)

Figure 2.14: (a) Measured GRE images of axial (top) and sagittal (bottom) cross-sections inside the phantom with loop coil excitation. (b) GRE images with annular ring circular patch probe excitation. (c) Normalized simulated circularly polarized B-field for the sagittal and axial cuts for the annular ring circular patch probe, using COMSOL Multiphysics.

the limited power from the amplifier and the attenuation in the below-cutoff gradient coil region.

In order to improve the SNR, a cylindrical array of 3 cm wide longitudinal copper strips 2 m long and 12 cm in diameter is inserted in the bore with a goal of modifying the traveling-wave mode content in the gradient coil region, as shown in Fig. 2.15.

The longitudinal strips present an artificial electromagnetic surface and modify the boundary conditions of the metallic bore. Since they are oriented in the axial direction, the strips present a different surface impedance to the axial electric field than to the transverse field, thus modifying

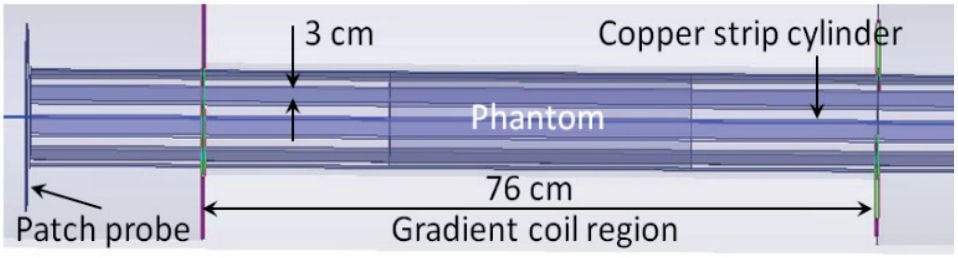

Figure 2.15: Sketch of parallel copper strip cylinder inserted into the bore and extending beyond the gradient coil region by 5 cm. The patch probe is placed at the beginning of the cylinder.

the mode profile. This can be seen in both simulations and measurements of the axial cross-section shown in Fig. 2.16a. The coronal images are in good agreement with field simulations as shown in Fig. 2.16b. For these images, the patch probe is placed 5 cm from the edge of the bore at the start of the strip cylinder. The MR images were obtained with a GRE sequence: field-of-view (FOV)=20x20 cm, repetition time (TR)/echo time(TE)=275 ms/2.1 ms, slice thickness of 1 mm for both axial and coronal slices. The high spatial frequency fringes and edge brightening correspond to artifacts due to unencoded volume of the dielectric guide that extends beyond the gradient insert.

Due to the high SNR, in addition to GRE, the first traveling wave spin-echo measurements at 16.4 T could be obtained, with an example shown in Fig. 2.17. A spin-echo sequence allows for compensation of system imperfections as it is the most robust sequence of pulses for imaging. These results demonstrate that traveling wave MRI with high SNR can be performed with proper probe exciters and bore design when the bore is small compared to the free- space wavelength of the Larmor frequency.

2.4 16.4 T Short Phantom

A shorter phantom of length 10.9 cm and diameter 9 cm is measured using the smaller annular ring circular patch probe from Fig. 2.2e and fabricated on FR4 Fig. 2.18a. The smaller ground plane allows the circular patch probe to be placed closer to the phantom, under the gradient coil region of the scanner. The experimental images obtained with the patch probe have relatively low SNR

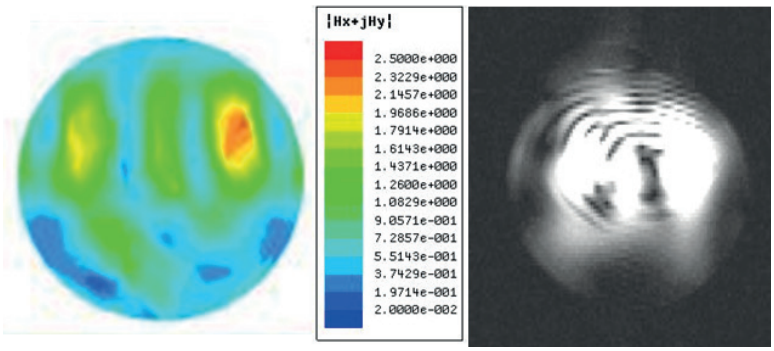

(a)

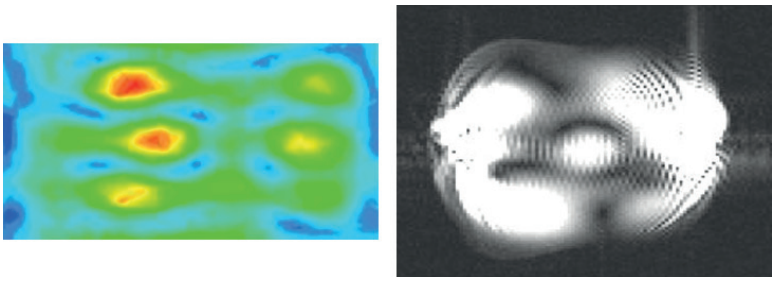

(b)

Figure 2.16: Magnitude of the simulated transverse right handed circular- polarized H-Field normalized to 1 W power input at the SMA connector of the probe (left) and MR images (right) taken with the patch probe and metal strip cylinder inserted in the bore, at a specific cross-section of the phantom for (a) axial and (b) coronal cross- sections. The SNR is increased seven-fold compared to the images in Fig. 2.14c

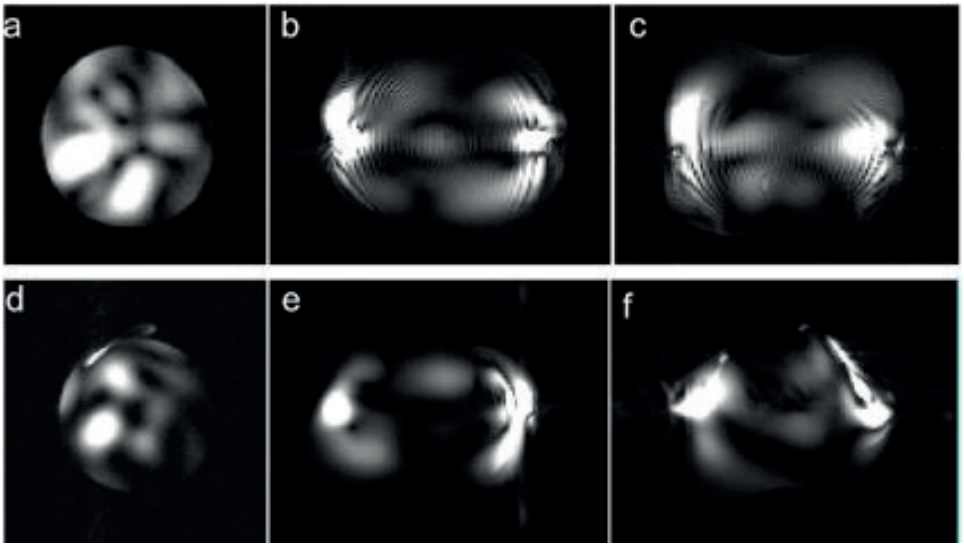

Figure 2.17: (a-c) GRE and (d-f) SE images obtained in phantom with patch and metal strip cylinder: (a,d) axial, (b,e) coronal, and (c,f) sagittal slices. (SE parameters: TR/TE=1 s/20 ms, FOV=20x20 cm^2, matrix=256x128, slice thickness of 2 mm, 0.8 mm gap, 10 slices)

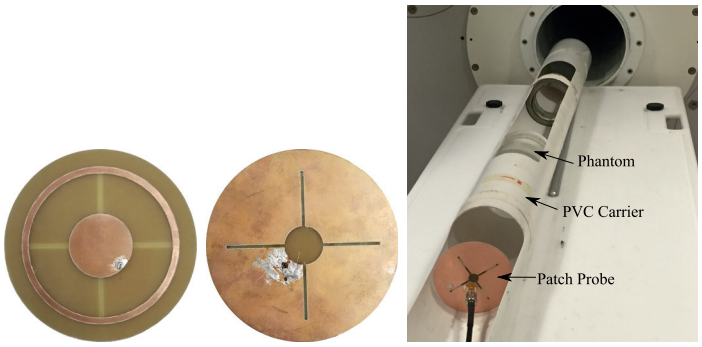

(a) (b)

Figure 2.18: (a) Fabricated small annular ring circular patch probe (Fig. 2.2e) and (b) experimental setup showing the patch probe with the phantom in the PVC carrier.

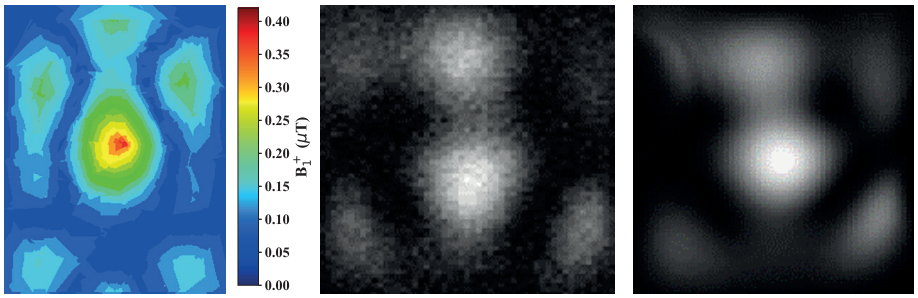

(a) (b) (c)

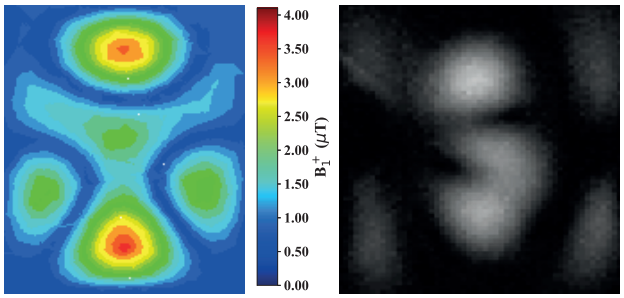

(d) (e)

Figure 2.19: (a) Simulated result with the patch probe placed 5 cm from the phantom. Experimental GRE images with the patch probe placed (b) 0 cm from the phantom, and (c) the patch probe 5 cm away covered with a copper strip array similar to the one used in the previous section.

when placed even 5 cm from the phantom Fig. 2.19b. Moving it closer results in a significantly higher contrast Fig. 2.19c, however, the field coverage is fairly low. By adding the same copper strip array as the previous section, the field coverage improves, Fig. 2.19e.

2.5 Conclusion

In summary, this chapter demonstrates 16.4 T MR images in a phantom excited by a traveling-wave field patch probe far from the phantom. In addition, an anisotropic copper strip cylinder is inserted into the bore, modifying the modal content. Although the guide diameter is too small to support traveling waves above cut-off for a metal guide, the strip cylinder changes the boundary condition thus changing the mode cutoff frequencies, allowing TW MRI, with a seven-fold increase in SNR as compared to the patch probe without the strip cylinder. This work is published in the proceedings of International Microwave Symposium in Phoenix 2015 [19].

Chapter 3

Patch-Probe Excitation for Ultra-High Magnetic Field Wide-Bore MRI

Contents

In this chapter, experiments are shown for a whole-body Siemens 7 T system, Fig. 3.2, equipped with an Agilent magnet with a bore that is 3.366 m in length with a diameter of 90 cm. Experiments in this chapter are done at the Center for Magnetic Resonance Research (CMRR) at the University of Minnesota, Minneapolis, Minnesota. The Larmor frequency at 7 T is 297 MHz, corresponding to a free-space wavelength of 1.01 m and a wavelength in the water-based phantom (ε_r=81) of 11.22 cm. The 90-cm open bore fits a human and is above the cutoff frequency for at least one

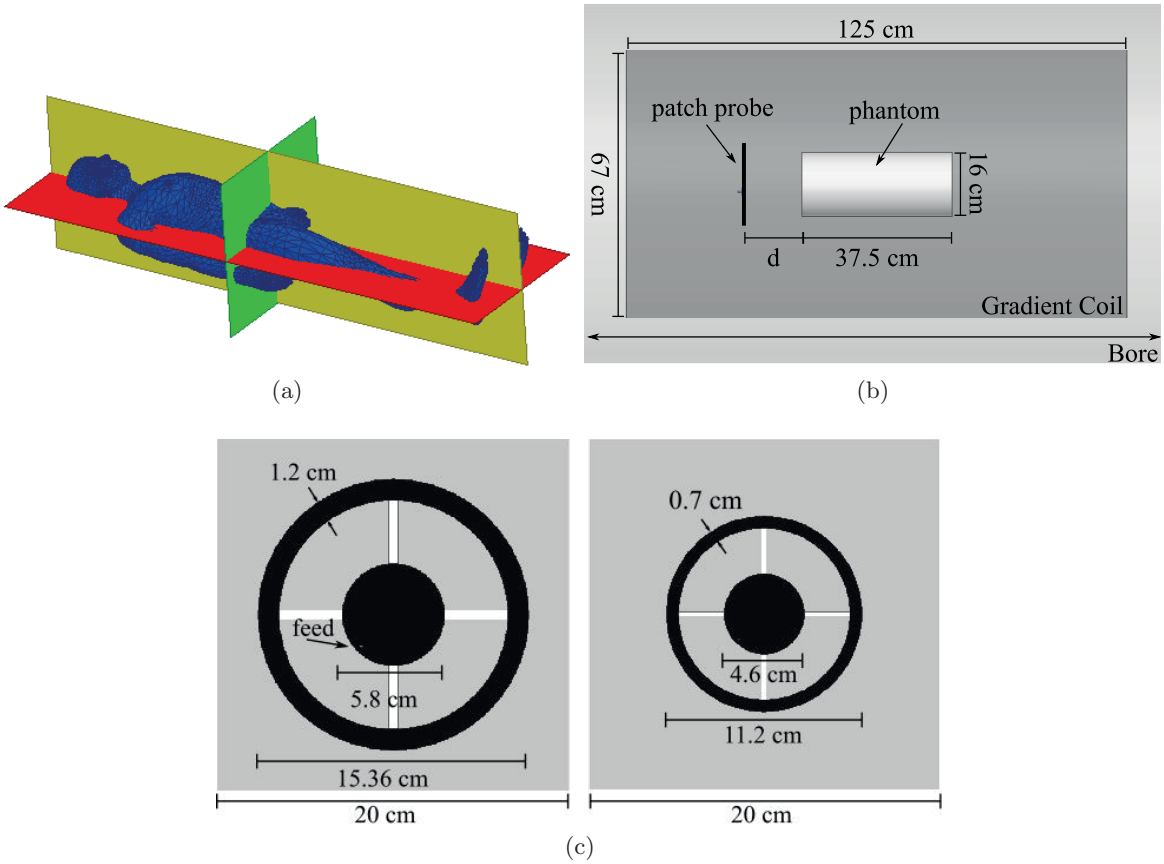

Figure 3.1: (a) Plane definitions for sagittal (yellow), coronal (red), and axial (green) cross-sections. (b) Sagittal view of the dimensions under the gradient coil for both 7 T and 10.5 T Siemens systems. The dark gray region is the region internal to the gradient coil. (c) 7 T (left, 297 MHz) and 10.5 T (right, 447 MHz) circular patch probes. Black indicates top metal, gray is the ground-plane, and the white rectangles are slots in the ground plane, and the dimensions are given for an FR-4 substrate.

mode of the bore when viewed as a cylindrical metallic waveguide loaded with a high dielectric constant, such as biological tissue, Fig. 3.1.

The chapter outline is as follows: in Section 3.1, the overall system geometry and probe layout are given, along with additional modifications of the bore, such as copper strip arrays and electrically hard surfaces, which enable improved field uniformity. Section 3.2 details simulations and measurements on the 7 T system, including dependence of image quality on geometric parameters such as probe distance from phantom and boundary condition modification. Section 3.3 presents multiple-probe transmit and receive results at 7 T, including experimental and simulated observations related to relative phasing between the two. Section 3.4 summarizes results for the

Figure 3.2: Image of the passively shielded 7 T Siemens MRI scanner at the Center for Magnetic Resonance Research.

10.5 T system, and, finally, Section 3.5 presents a discussion on the numerical analysis. Ansys High Frequency Structural Simulator (HFSS) full-wave electromagnetic finite element solver is used for all simulations presented in this chapter. Gradient non-linearities are not corrected for, resulting in well known barrel-shaped experimental image distortion instead of a correct restitution of the cylindrical shape of the physical phantom.

3.1 System and Probe Layout

The systems used in this work are two whole body human dimensioned (67 cm bore) MR scanners operating at 7 T and 10.5 T (Siemens, Erlangen, Germany). The spin excitation (Larmor) frequency is determined by

$$f = \gamma B_0 \tag{3.1}$$

where γ is the gyromagnetic ratio and B_0 is the static magnetic field. Using the gyromagnetic ratio of hydrogen, $\gamma = 42.58\,\mathrm{MHz/T}$, the proton Larmor frequency is calculated to be 297 MHz at 7 T and 447 MHz at 10.5 T [4]. Whole body MR systems, including high field, are built around wide-bore magnets that accommodates the size of a human body. In MRI, slice orientations include three orthogonal planes defined as sagittal, coronal, and axial as shown in Fig. 3.1a, dividing the body in left and right, anterior and posterior, cranial and caudal portions, respectively. Sagittal

cuts crossing the magnet iso-center will be presented in the remainder of the chapter, as single coronal cuts centered cuts missed the phantom iso-center due to an off-centered elevation of the phantom holder in the vertical direction.

Circular patch antennas have been used in traveling wave MRI [20] due to the circular nature of the currents and higher directivity than dipoles of the same size fed in quadrature. Therefore, the modeling is done with a metal cylinder the size of the bore, and the distance to the phantom is varied to verify the traveling wave conditions. Coupling of the circularly-polarized magnetic field into the phantom is examined in simulations by observing the transverse components of the B-field.

3.1.1 System Dimensions

The wide-bore system in Fig. 3.1b shows the relevant dimensions and position in the bore of the gradient coil, the water phantom, and patch probe. The two systems are nearly identical dimensionally (both are equipped with the same gradient coil), other than the complete bore length. The 7 T system is 336.5 cm long while the 10.5 T system is longer by about one-fifth, at 410 cm. The electrical lengths are, however, greatly different, thus producing different mode structures. The cutoff frequency for the TE_{11} mode of the air-filled circular waveguide (bore) can be calculated using [62],

$$f = \frac{0.293}{a\sqrt{\mu\varepsilon}} \tag{3.2}$$

where a is the radius of the waveguide. For the 7 T system the cut-off frequencies are found to be 199.8 MHz in the bore and 262.4 MHz inside the gradient coil. With the addition of a high permittivity dielectric, the cutoff frequencies will decrease, allowing for the propagation of additional modes. The first four propagating modes for a 7 T MRI are solved for in [63] to be HE_{11}, TE_{01}, HE_{21}, and TM_{01}. The high attenuation of the first four modes shows that the excitation source must be close to the phantom, but not so close that traveling wave conditions are not met. Necessary computational resources in simulations are substantially minimized by excluding physical components, such as the plastic bore cover and patient table, that are structurally complicated to mesh but electrically insignificant as shown later in section III. The phantom used for experiments

is the Siemens 55 12 608 K2205, which is 16 cm in diameter and 37.5 cm long. This phantom is approximated by a cylinder of the same dimensions with a dielectric permittivity of $\varepsilon_r = 81$ and conductivity of $\sigma_d = 0.4\ S/m$.

3.1.2 Circular Patch Probe

A circular patch with an outer ring and slots is chosen as an excitation source due to the circular nature of the current on the patch and compact design [61]. The uneven slots in the ground plane enable single coaxial feed right handed circular polarization. The probe is implemented using FR-4 62.5 mil thick substrate with $\varepsilon_r = 4.35$ at 297 MHz. The probe is designed using full-wave simulations for 297 MHz excitation with dimensions seen in Fig. 3.1c. The 5.45 mm wide slots in the ground plane are 15.4 cm and 15.22 cm long, creating a right handed circular polarized current distribution, with the feed diagonally 2.55 cm from the center. The probe is fed using a coaxial feed using an SMA coaxial connector exciting the inner circularly-shaped metal. The single feed and uneven slots create a quadrature current excitation which enables circular polarization. For the opposite sense circular polarization, the feed can be moved 90 degrees around the patch in either direction. The probe for 10.5 T is implemented using the same FR-4 substrate with a permittivity of $\varepsilon_r = 4.25$. The dimensions can be seen in Fig. 3.1c with 2.5 mm wide slots that are 11.25 cm and 11.03 cm long and the feed 2.05 cm from the center. The ground plane is much larger than necessary to provide mounting similar to the 7 T probe experiments. Both probes exhibited a measured narrow-band 10 MHz bandwidth return loss greater than 15 dB with no additional matching inside the bore. The probe is placed at a distance d from the phantom as shown in Fig. 3.1b. This distance varies depending on the experiment.

The quality of the near-field circular polarization is determined by the currents of the probe. Right-handed circular polarization is defined by the electric field tracing a clockwise circle from the receiver's point of view. The magnitude of the current density on the top conductors as the phase advances is shown in Fig. 3.3. The magnitude of the current density on the ground plane can be seen in Fig. 3.4. The slots behave similarly to dipoles in quadrature where in Fig. 3.4b the current

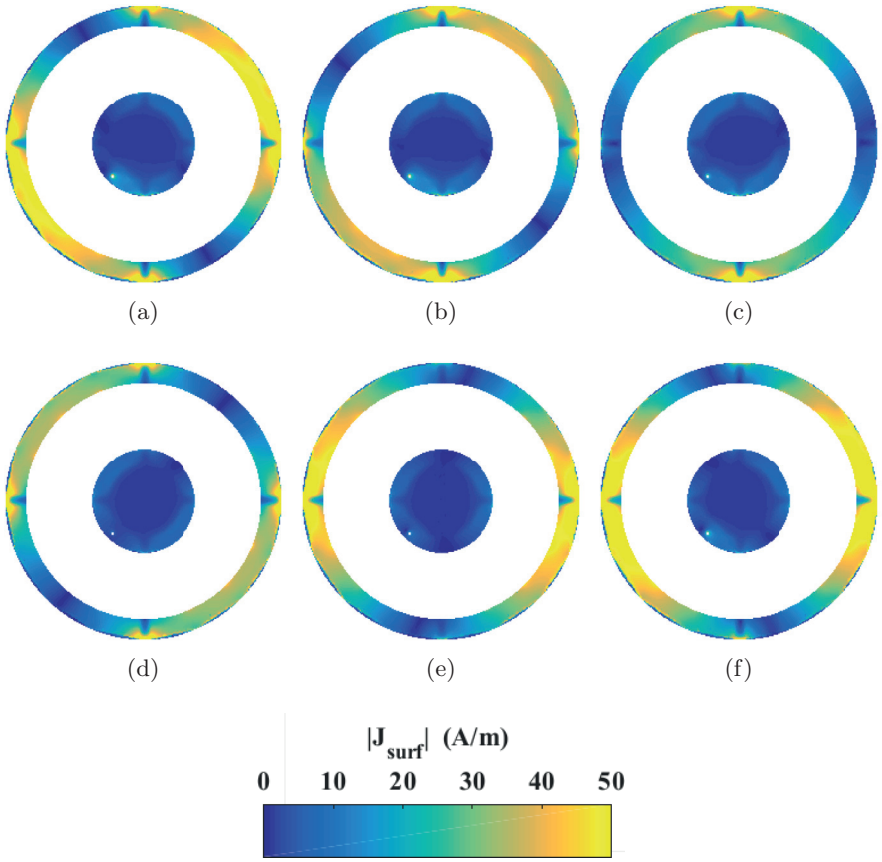

Figure 3.3: Magnitude of the current density on the top conductors of the patch probe as the phase advances from 0 (a) to 150 (f) degrees with a step size of 30 degrees (indicated in black in Fig. 3.1c).

density fully illuminates the vertical slot. As the current advances 90 degrees, the current density in Fig. 3.4e fully illuminates the horizontal slot. As a result of this behavior, the magnitude of the current density traces an elliptical pattern. When simulated as an antenna, the probes exhibit a 1 dB far-field axial ratio.

3.1.3 Electrically Hard Surface

Experiments from [19] show that field coupling and distribution can be improved by modifying the modes in the bore through changing the boundary conditions. For example, electrically hard surfaces are used in horn antennas to increase aperture efficiency [64]. A longitudinally corrugated surface where the tangential electric and longitudinal magnetic fields are equal to zero along the

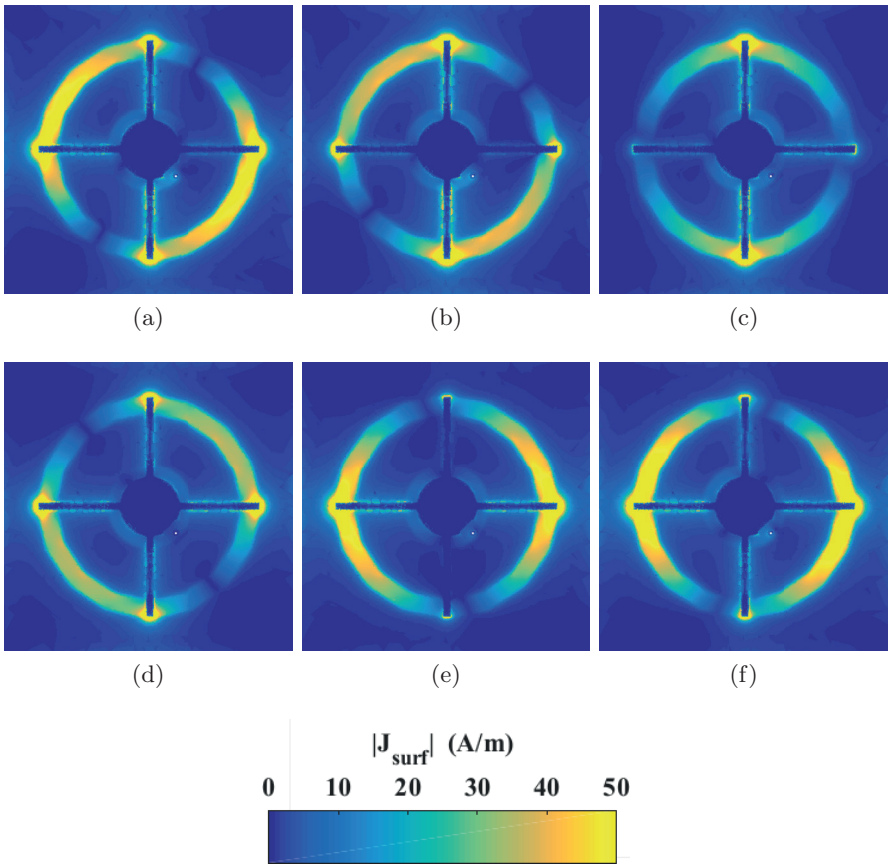

Figure 3.4: Magnitude of the current density on the ground plane of the patch probe as the phase advances from 0 (a) to 150 (f) degrees with a step size of 30 degrees (shown in gray in Fig. 3.1c).

surface is referred to as an electrically hard surface [65]. Electrically hard surfaces can either be formed by implementing dielectric-filled longitudinal corrugations or longitudinal conducting strips on a dielectric horn antenna [64].

For experiments presented in this chapter, longitudinal conducting strips are implemented without a dielectric. Since it is an approximation to a hard surface, we refer to it as a copper strip array, and simulations show that only the magnitude of the fields is slightly affected by eliminating the dielectric. The longitudinal strips are implemented using copper tape on a thin plastic sheet and wrapped around the dielectric phantom, Fig. 3.5. The strips are 3 cm wide with 3 cm separation and the length is varied for different experiments.

3.2 7 T Simulated and Experimental Results

The distance between the probe and the phantom is varied to help determine the optimal location for the best signal strength and SNR. The copper strip structure is then set up in various configurations to analyze the effect on SNR and signal intensity. All images are taken using a gradient recalled echo sequence for a FOV of 20x40 cm^2 with a small flip angle. This small flip angle regime preserves

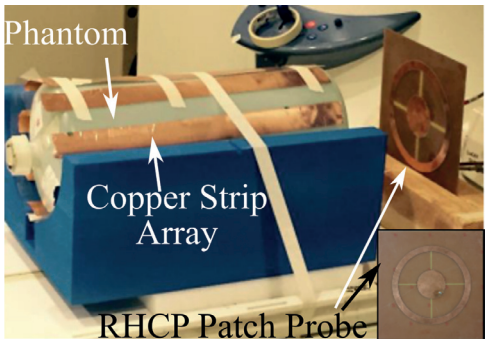

Figure 3.5: Experimental setup of electrically hard surface approximated by thin copper strips on a plastic sheet on a 16 cm diameter phantom for a 7 T system. The probe used is shown in the bottom right.

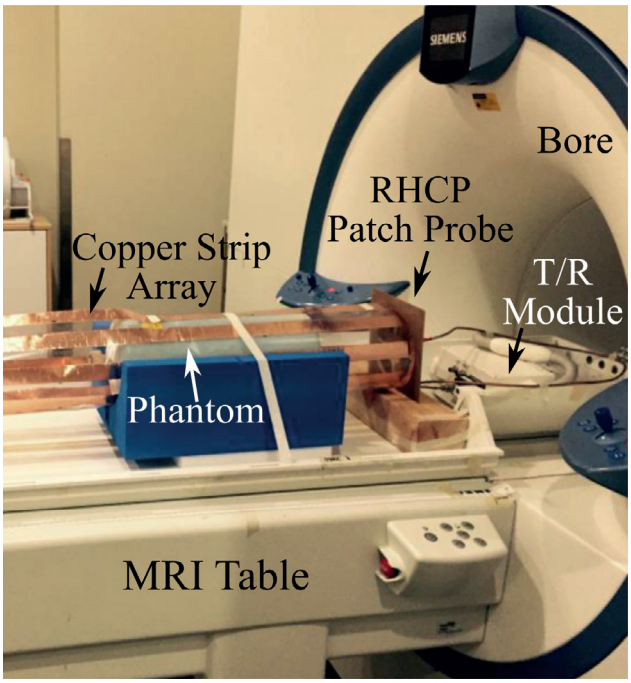

Figure 3.6: Complete setup showing the probe and phantom on the Siemens table and connected to the T/R switch. The copper strip array covers both the air gap and phantom.

direct proportionality between the magnitude of the detected MR signal originating inside the phantom and the corresponding excitation field magnitude distribution. Note that the detected signal is also proportional to the receive field magnitude and to the proton density of the phantom.

The probe is placed d=15 cm from the phantom and simulated to measure the effects of several extra physical features. The features modeled include the plastic covering over the gradient coil, the foam that is used to support the cylindrical phantom, and the plastic patient table. Fig. 3.7 shows the result with and without the extra features modeled. The extra features cause an asymmetry in the fields toward the foam holder (left side of the plot), deforming the center mode pattern from the oval shape shown in Fig. 3.7b. The result shown in Fig. 3.7b is used as the basis for comparing all results.

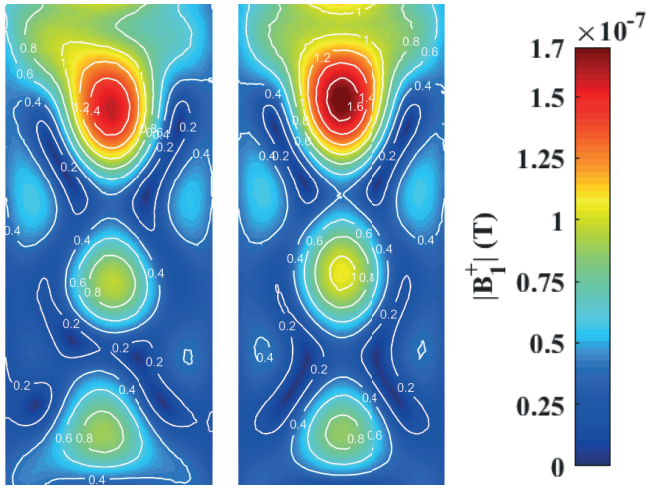

(a) (b)

Figure 3.7: 7 T simulations of the probe 15 cm from the phantom with (a) and without (b) modeling the plastic covering over the gradient coil, foam phantom support, and table. Normalized to 1 W input power at the probe port.

3.2.1 Distance Sweep from the Phantom

With its long axis parallel to the long axis of the magnet, the phantom is positioned at the center of the latter along the foot-head direction, and slightly off-centered above the patient table, held within a foam holder. The phantom is imaged at several distances from the patch probe: the

location closest to the phantom (d=4.5 cm); the farthest possible location (d=40 cm); and two distances in between (d=15 and 25 cm).

The experimental results, Fig. 3.8, are plotted as magnitude images using a DICOM viewer and individually scaled to show the overall mode pattern. The first distance, d=4.5 cm and Fig. 3.8a, shows a vertical asymmetry in the mode pattern, corresponding to a degradation in the circular polarization, which results in wasted power in the cross-polarized field. The second distance, d=15 cm and Fig. 3.8b, shows excellent matching with the simulated mode pattern (Fig. 3.7b), with reasonable SNR. The image, however, is slightly skewed due to the physical mounting of the probe. The semi-rigid cables and magnetic solder prevent perfect vertical positioning of the probe and the foam phantom holder creates a material discontinuity. The next distance, d=25 cm and Fig. 3.8c, shows a similar image to the 15 cm case but of slightly lower magnitude and SNR. The last case, d=40 cm and Fig. 3.8d, shows very little signal coupled and low SNR. These results indicate that between 15 and 40 cm there is a consistent field profile based off the probe excitation and a traveling wave is indeed excited.

The magnitude of the simulated response is shown in Fig. 3.8e (left) and the SNR, Fig. 3.8e (right) calculated according to [66] with a one centimeter square box in the center mode pattern used for comparison. Distances between 15-25 cm are usable, with only limited magnitude variation and a preserved overall mode pattern. Beyond 25 cm, however, the distance is too long, leading to decreased signal strength, thus lower SNR, which translates into lower image quality. From these results, 15 cm is taken to be the best location and is used for future experiments.

The distance, d, between the phantom and the excitation plays two critical roles. First, the cross polarization effects and reflected power become greater as the probe moves closer to the phantom due to the large discontinuity of the high dielectric constant phantom. The farther the probe is from the phantom, the more consistent the frequency response and circular polarization will be for different dielectrics. Second, as the probe moves farther away, the SNR degrades due to the decrease in overall coupled field, but the peak magnitude (located close to the probe) stays fairly high. This field imbalance causes a degradation of the mode features farther into the phantom

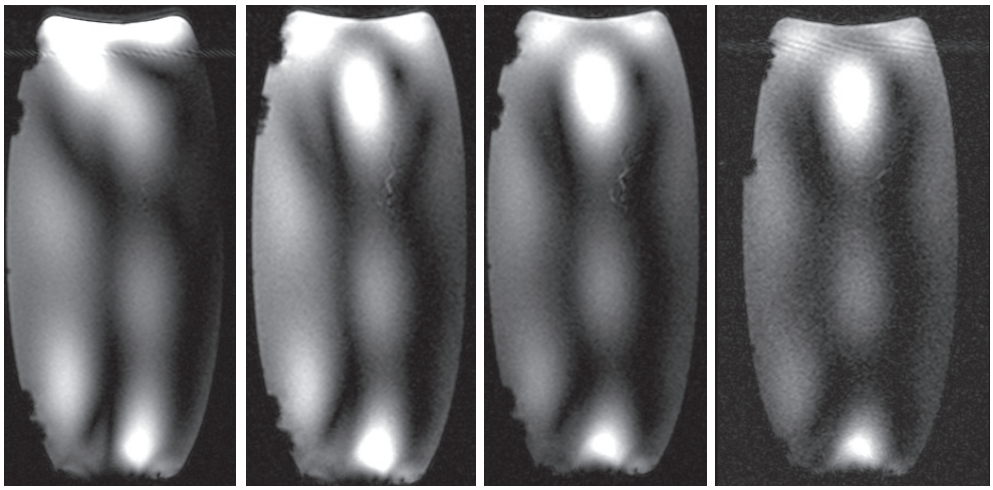

(a) (b) (c) (d)

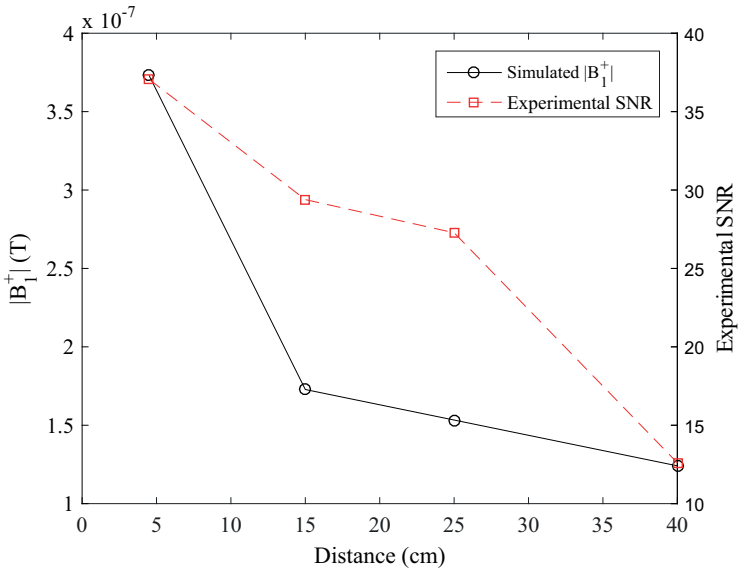

(e)

Figure 3.8: MR images plotted to show the mode pattern variation for different d (Fig. 3.1b) (a) 4.5 cm, (b) 15 cm, (c) 25 cm, and (d) 40 cm. Images are individually scaled to show consistency in excited mode pattern with magnitude variations shown in Fig. 3.8e. (e) Magnitude of the simulated response and SNR for the locations (a)-(d).

and produces an overall noisier image. The resulting pattern may be expected to be clinically unusable. Furthermore, there is a large deviation between the maxima and the middle and edge field magnitudes along with large gaps in field coverage. To remedy this deviation, the field should be homogenized, which can be addressed by changing the boundary conditions, as described next.

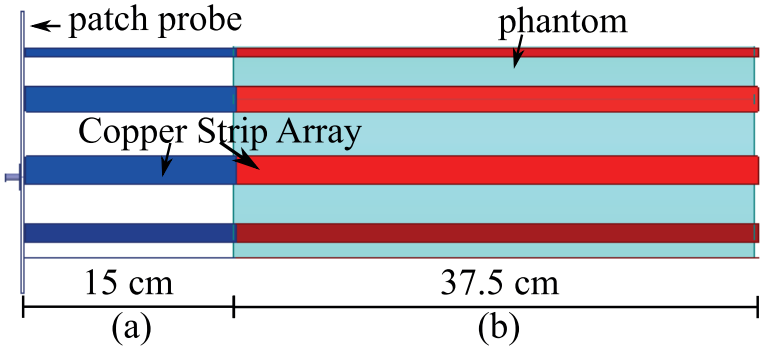

Figure 3.9: Details the setup of copper strip experiments. (a) Air gap between the probe and phantom. (b) Phantom.

3.2.2 Copper Strip Array Experiments

Next, experiments are run with d=15 cm and with the copper strip array (Fig. 3.5) for the following cases:

(a) No copper strip array

(b) strips covering the 37.5-cm phantom (Fig. 3.9b)

(c) strips covering the 15-cm air gap (Fig. 3.9a)

(d) strips covering the 30-cm air gap

(e) strips covering the 15-cm air gap and phantom (Fig. 3.5)

The simulated results corresponding to the above configurations are shown in Fig. 3.10. The magnitude of the field of the first strips experiment, (b), is similar to the case with no copper strip array, but broadens slightly at the top of the phantom and reduces the field away from the probe. The second strips experiment, (c), creates a classical near field absorption parameter with high field concentrated close to the probe and little elsewhere as shown in Fig. 3.10c. To try and balance the possible near field pattern with the field in the rest of the phantom, the probe is moved out to d=30 cm. Fig. 3.10d shows a result similar to Fig. 3.10a but with increased field strength, and a mode pattern which is more visible across the entire image compared to Fig. 3.10c. The last case

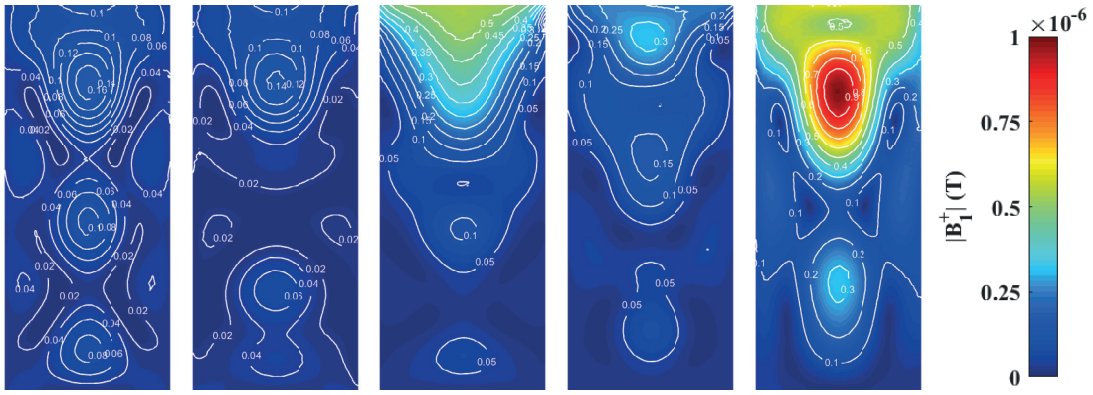

(a) (b) (c) (d) (e)

Figure 3.10: Simulations of copper strip array experiments for: (a) No copper structure (b) 37.5 cm phantom (c) 15 cm air gap (d) 30 cm air gap (e) Phantom and 15 cm air gap. Simulations are plotted on the same scale. Normalized to 1 W input power at the probe port.

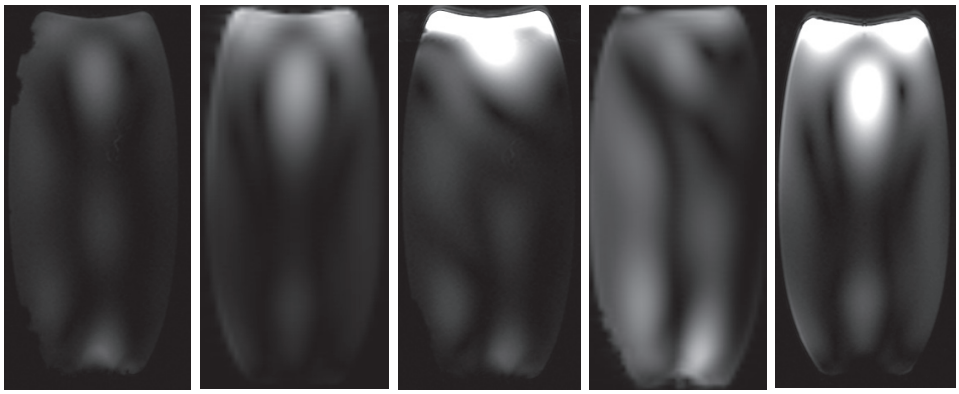

(a) (b) (c) (d) (e)

Figure 3.11: MR images for: (a) No copper structure (b) 37.5 cm phantom (c) 15 cm air gap (d) 30 cm air gap (e) Phantom and 15 cm air gap. MR images are plotted on the same scale.

moves the probe back to d=15 cm and uses the copper strip array covering the 15 cm air gap and the 37.5 cm phantom.

Experimentally, the copper strip array performs as expected, as shown in Fig. 3.11. For the first experiment, Fig. 3.11b, the field coupling is comparable to Fig. 3.11a, but the mode pattern has changed. The top mode pattern has spread, as expected with the copper strip array. The lower mode pattern is faint compared to the upper pattern, while the middle mode pattern disappears almost completely. This could in principle be desirable for an application focusing solely on a region

close to one edge of the imaging volume, such as the brain. The mode pattern farthest from the excitation is a result of the impedance discontinuity between the phantom and the air and would vanish in a longer or higher loss phantom.

In the second experiment with the d=15 cm air gap, the copper strips and close distance results in a large amount of field coupled at the near end of the phantom compared to the rest. This shifts the scale and causes the image to appear almost blank as shown in Fig. 3.11c. In an attempt to balance the field, the probe is pushed back to d=30 cm, Fig. 3.11d. This pattern is nearly identical to that of Fig. 3.11d. With this structure and double the separation, the magnitude of the field coupled is much higher than in the case with no copper strip array, Fig. 3.11a.

Creating a complete copper strip array that extends from the probe to the end of the phantom, yields an image with higher SNR and spreads the field more over the first 10 cm of the phantom, Fig. 3.11e. The SNR is 7 times higher than the case with no copper strip array, Fig 3.11a, as shown in Table 3.1. The large SNR improvement is a result of the copper strip array covering the air gap, while the mode change is due to the copper strip array covering the phantom. The SNR presented in Table 3.1 and 3.2 is calculated using a 1 cm^2 square around the maximum field intensity.

Table 3.1: SNR for Single Probe Experiments

Experiment	**SNR**
d=15 cm Fig. 3.11a	46
Copper Strip Array (b) Fig. 3.11b	92
Copper Strip Array (c) Fig. 3.11c	347
Copper Strip Array (d) Fig. 3.11d	79
Copper Strip Array (e) Fig. 3.11e	331

It was found that the copper strip array has an impact when placed within one centimeter of the imaging volume. If it is placed any farther, the effect begins to diminish. Imaging a human with this setup poses a few difficulties. The strips must be placed in such a way that they do not irritate the patient, that is, they are placed away from sensitive areas such as the ears, eyes, nose, and mouth. For a head scan, these can be placed primarily over the volume that encompasses the brain. Additionally, any metal in contact with the skin will cause a peak in Specific Absorption

Rate (SAR) and undesired local heating. Simply placing a dielectric layer less than 0.5 cm thick under the strips reduces this peak inside the body without reducing the effect of the copper strip array.

3.3 7 T Multiple Probe Transmit/Receive Results

An additional identical patch probe is placed on the opposite side of the phantom as seen in Fig. 3.12. This probe has the same dimensions as the original probe, but the feed is rotated 90° to accommodate the opposite polarization. This probe must be of opposite polarization to ensure both probes excite the atomic spins in the same direction. Adding an extra probe to the system tests the use of B_1 shimming along with the effects of the copper strips.

By phasing the two probes 180° apart, Fig. 3.13a shows that the mode pattern can be shifted primarily to the top region. The field profile is now elongated and moved to the upper region of the phantom. The opposite is true when the probes are fed in phase. The mode pattern has now shifted towards the bottom of the phantom. When the probes are fed in quadrature, the modes merge in the center to create an extended center mode pattern. While the signal is now spread out over the majority of the phantom fairly evenly, bright spots still exist and need to be controlled. Constructive interference has created a higher peak field magnitude compared to the single probe case even with the same total input power.

Adding the copper strip array across both gaps and the phantom creates the mode structures shown in Fig. 3.14. The performance is similar to the single probe case with the copper strip array,

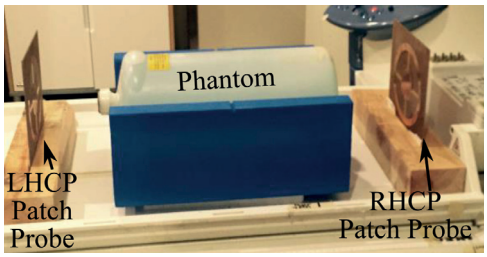

Figure 3.12: Setup for the multiple probe experiments showing a RHCP probe (right) and LHCP probe (left), placed 15 cm from the phantom edges.

Fig. 3.10e. In this case, however, the peak signal is slightly lower and the field is more evenly distributed in the ends of the phantom.

The MR images from Fig. 3.15 show the case of one probe transmitting and both probes receiving. As expected, the lower mode pattern is brighter in every case due to the placement

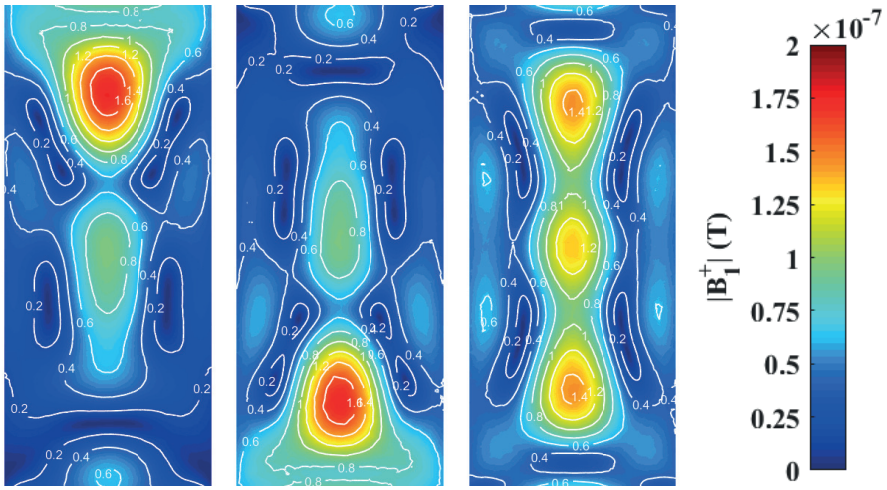

(a) (b) (c)

Figure 3.13: Simulated results for relative phasing of (a) 180°, (b) 0°, and (c) 90° between the two probes, normalized to a total input power of 1 W.

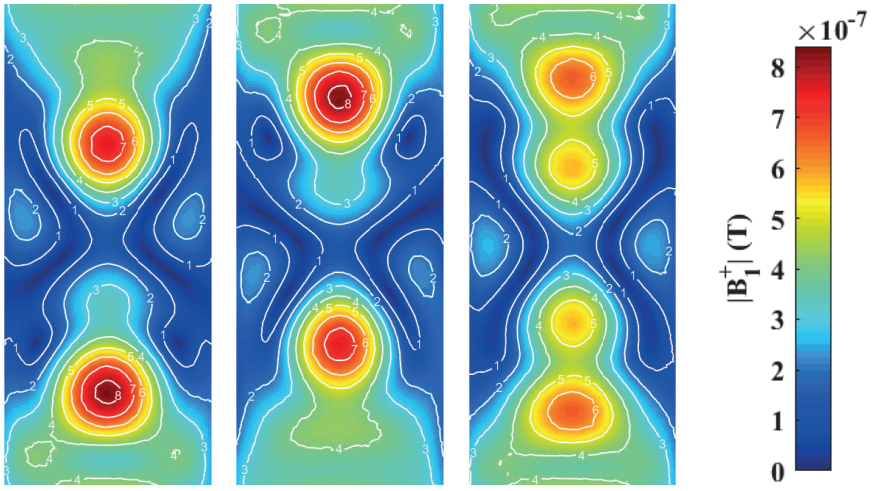

(a) (b) (c)

Figure 3.14: Simulated results for relative phasing of (a) 180°, (b) 0°, and (c) 90° between the two probes with the added copper strip array, normalized to a total input power of 1 W. Note the field magnitude is four times higher than the case without a copper strip array in Fig. 3.13.

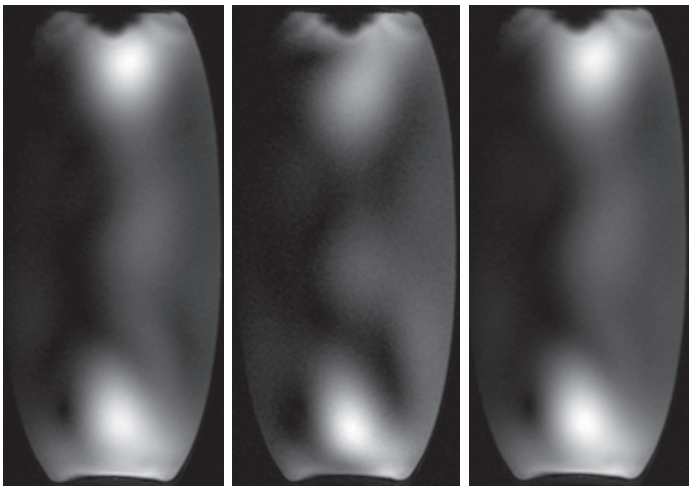

(a) (b) (c)

Figure 3.15: Measured images for (a) Receive only probe (b) T/R probe (c) Combined image of (a) and (b).

of the transmit probe. Similarly to the single probe case, the middle pattern tends towards the right (posterior) of the image. The mode pattern farthest from the excitation in Fig. 3.15a is much brighter than in the single probe case and in Fig. 3.15b. This confirms reciprocity between transmit and receive field patterns. Interestingly, the SNR is slightly lower in the combined case, as shown in Table 3.2. This is most likely due to the additional noise present in combining the two images without any additional power. This SNR figure has increased dramatically compared to the single probe case, however, the setup, mainly the T/R switch module, and imaging parameters also changed between experiments.

The two transmitting probes allow B_1 shimming, which here consists in adjusting the relative phase of the excitations to create a region as homogeneous as possible. For this experiment, top, bottom, and center focusing regions were defined. From Fig. 3.16c, B_1 shimming produces a more homogeneous signal in the center of the phantom connecting the two bright mode structures. The shift of the center mode is also removed with this technique. The results show this probe can use the same B_1 shimming methods as classical structures.

Initially, the copper strip array is added to the system without attempting B_1 shimming. The image shown in Fig. 3.16d has structural similarity to the simulated field profile, Fig. 3.14b shows

a noticeable SNR improvement over the two probe case and a broadening of the field similar to that seen in the single probe case with a copper strip array. The simulated field strength has five times the field strength over the initial case with one probe and no copper strip array. The actual result is 1.86 times higher than the SNR as the single transmit probe case, Fig. 3.15c.

Table 3.2: SNR for Multiple Probe Experiments

Experiment	**SNR**
Receive Probe Fig. 3.15a	235
T/R Probe Fig. 3.15b	226
Combined Fig. 3.15c	194
B_1 Shim Top Fig. 3.16a	156
B_1 Shim Bottom Fig. 3.16b	211
B_1 Shim Middle Fig. 3.16c	192
B_1 Shim Copper Array Fig. 3.16d	362

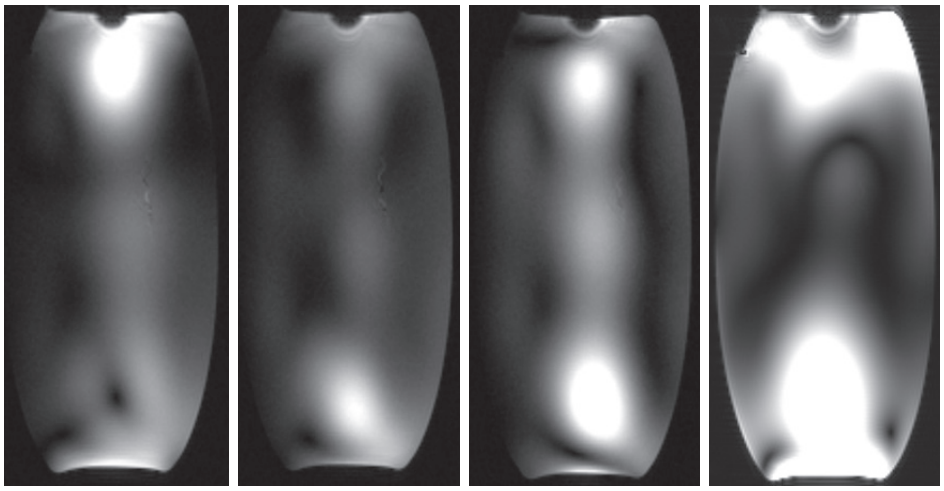

(a) (b) (c) (d)

Figure 3.16: B_1 shimming for regions: (a) Top Region (b) Bottom Region (c) Center Region (d) Added copper strip array.

3.4 10.5 T Simulated and Experimental Results

Traveling wave excitation and detection systems in MRI can potentially be advantageous in terms of providing a more comfortable environment for patients, a larger field of view, imaging hard-to-

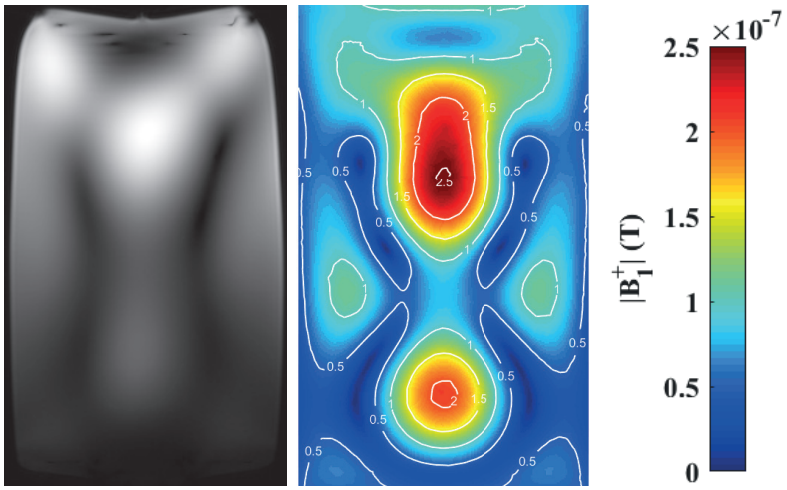

(a) (b)

Figure 3.17: (a) Tuned 7 T head volume coil MR image at 10.5 T (b) Simulated patch probe excitation.

reach organs (e.g., prostate gland) and some areas that are difficult to access with MRI, as well as enabling new spatial encoding schemes and a variety of mode sensitivity profiles [67]. As the wavelength decreases in size compared to the imaging volume, the quasi-static approach suffers. To illustrate this concept, a 7 T head coil tuned to work at 10.5 T (447 MHz) is imaged. A smaller phantom with a 12 cm diameter and 20 cm length is used as the imaging volume for the head coil. As shown in Fig. 3.17a, inhomogeneity due to modes is present in the classical volume coil excitation. This mode structure is identical to the simulated patch probe excitation for the same phantom. This shows that, independent of the approach, similar mode patterns appear for a given phantom, indicating that similar solutions for improving field homogeneity could be applied to traveling-wave and classical excitations. However, the excited region for a traveling-wave excitation extends farther than in the case of near-field coil excitations [20].

A single patch probe is excited to observe the simplest case results at 10.5 T so they can be compared to simulations. The copper strip array is then wrapped around both the gap and the phantom. All images are taken using a gradient recalled echo sequence for a FOV of 16.25x40 cm^2 with a small flip angle.

Experiments on the 10.5 T system use the same phantom and the probe seen in Fig. 3.1c

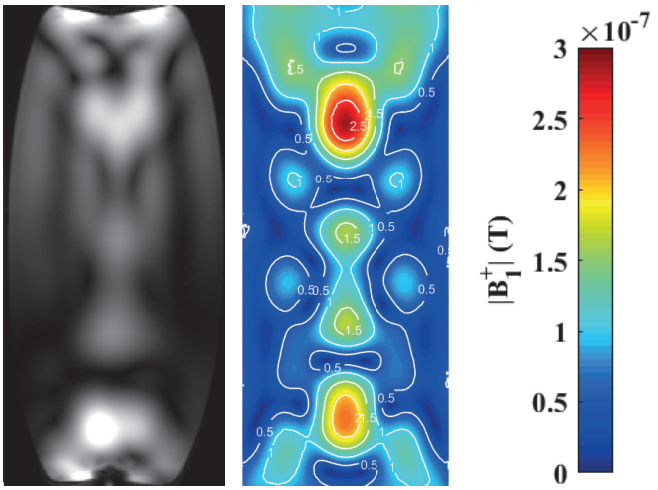

(a) (b)

Figure 3.18: Single probe experiment results for: (a) MR image (b) Simulated patch probe excitation.

(right). The probe is placed 15 cm from the phantom, similar to setup of the 7 T experiments. Due to the increase in frequency, the mode pattern is more complicated compared to 7 T with the same phantom. However, the pattern obtained in the experimental MR image in Fig. 3.18a has strong similarity with the simulated image shown in Fig. 3.18b. While some overall similarity can also be observed between field magnitude profiles observed at 7 T and 10.5 T, the 10.5 T pattern clearly exhibits a more complex distribution that includes multiple local spots with high or very low field magnitude. The SNR of the experimental image was found to be 471.

It is found that a copper strip array does not improve field homogeneity since the electrical size of the bore and phantom are larger than at 7 T. It should be noted, however, that it is well known from experience that improving homogeneity in a uniform water-based dielectric phantom at high magnetic fields is typically very difficult, if not impossible. By contrast, the human head is a complex combination of different tissues, with an averaged relative permittivity $\epsilon_r \approx 55$ offering more flexibility in terms of B_1 field modulation. Using Sim4Life, the human body tissue numerical model of a male adult (Duke, IT'IS, Zurich, Switzerland) from the IT'IS virtual population is used to load the probe with and without a copper strip array (Fig. 3.19) at 447 MHz and to compute the resulting B_1 distribution. The copper strip array extends from the probe, follows the contour

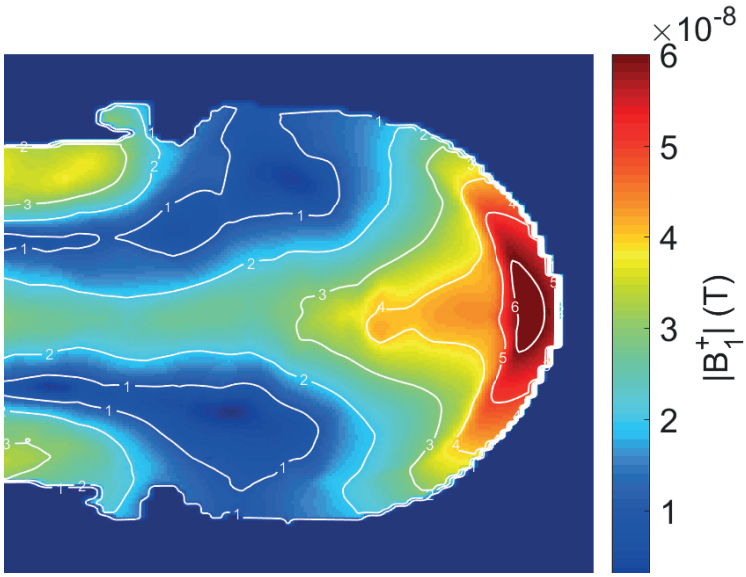

(a)

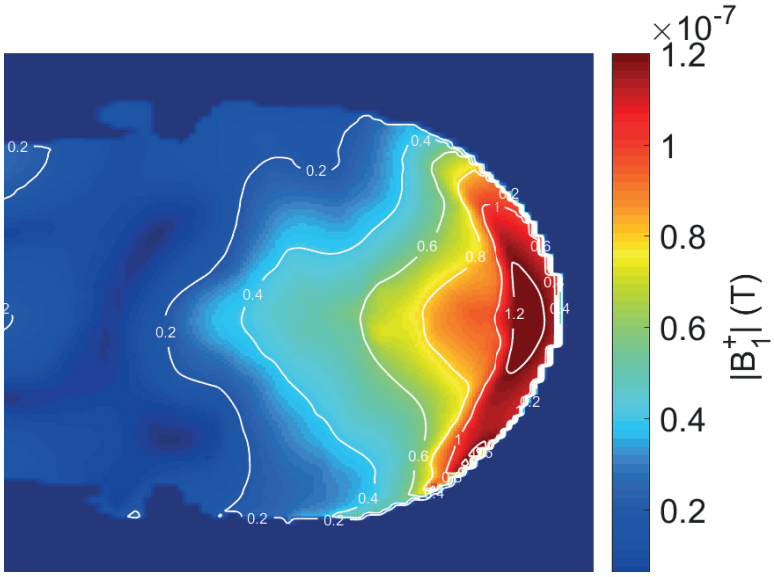

(b)

Figure 3.19: Sim4Life simulated results using Duke from IT'IS virtual population (a) without copper strip array and (b) with copper strip array.

of the head, and stops at the ear. The copper strip array limits the field propagation to only the region of interest around the brain and expands the mode pattern to the areas with nulls. This will also constrain the E-field to this area.

3.5 Numerical Methodology

Current simulation methods include complex physics modeling or a quasi-static approximation of the system [68]. The physics simulations model the excitations and response on an atomic level, thus requiring extensive computational resources and time. This approach is typically done with a finite difference time domain solver. For high field MRI, the frequency is too high to use the quasi-static approximation as the imaging volume is electrically large. For wide bore MRI, the computational domain becomes much larger and must model the interactions between the RF excitation and the bore.

The goal of this analysis is to simplify the numerical problem without introducing significant additional error. Only one excitation and the transmit probe are modeled, since this adequately illustrates the problem, while introducing more excitations and boundary structures would further increase computational resources. This analysis is done using Ansys HFSS finite element modeling with mixed order basis functions for the 10.5 T system. The time presented is total CPU time on a 3.6 GHz Intel i7-3820. To observe the effect of the bore, four different approaches are taken and results compared to a control case. The chosen control simulation is the complete system of the bore and gradient coil as shown in Fig. 3.1b. An air box with a radiation boundary is placed around the bore. This simulation approximates the physical setup of the MRI and is shown in Fig. 3.18b. To ensure adequate mesh coverage and overlap for comparison, the maximum mesh size inside of the phantom is set at 1.5 cm. This simulation takes 1:37:05 (hr:min:sec) and requires 19.7 GB of RAM.

The first approach simply removes the bore from the simulation. The reasoning here is that the field from the probe diminishes relatively quickly, thus the bore has little effect. The resulting simulation can be seen on the left in Fig. 3.20a with the overall percent error shown on the right. The main difference from the control simulation lies in the gradient of the field intensity. The fields decay slightly slower, resulting in a somewhat expanded mode pattern. This simulation is not much faster at 01:20:36 and uses 18 GB of RAM. With this approach, the average error across the field

Table 3.3: Summary of Results of Numerical Study

Method	**CPU Time** (hr:min:sec)	**Memory** (GB)	**Percent Error (%)**
Control Fig. 3.18b	01:37:05	19.7	N/A
Bore Removed Fig. 3.20a	01:20:36	18	18.51
No Bore/Gradient Coil Fig. 3.20b	00:58:19	14.9	28
Radiation Boundary on Bore Face	01:14:05	16.8	12.33
Radiation Boundary on Gradient Coil Face Fig. 3.20c	00:57:33	14.1	12.42

slice is 18.51 %. This setup is important as not all software allow complete control over the outer boundary conditions.

The next approach removes the bore and gradient coil, leaving just the probe, phantom, and a radiation boundary. This reduces the simulation time down to 00:58:19 and a total RAM usage of 14.9 GB, but at great cost. As expected, the field profile significantly changes as shown in Fig. 3.20b. The field propagation through the phantom is very poor and, overall, does not match the experimental results shown in Fig. 3.18a. This result clearly highlights the importance of the waveguide effects of the MRI system when using the excitation probes investigated in the present study. The average error is much higher at 28 %.

The third approach keeps the bore and gradient coil in place, and adds a radiation boundary to the opening of the bore. This reduces the simulation time down to 01:14:05 with a total RAM usage of 16.8 GB. The reduction can be attributed to removing the over-modeled exterior of the system. The average error is lower at 12.33 %. The plot is not shown, however, the results are nearly identical to the next approach in Fig. 3.20c, where the bore is eliminated and radiation boundaries placed on the faces of the gradient region. This only slightly reduces the simulation time to 00:57:33 and RAM usage to 14.1 GB. The result shown in Fig. 3.20c matches the control simulation very well. The average error remains similar at 12.42 %.

These simulations, summarized in Table 3.3, are useful in providing an overall understanding of what to expect when constricting the solved region. While this simulation setup is relatively

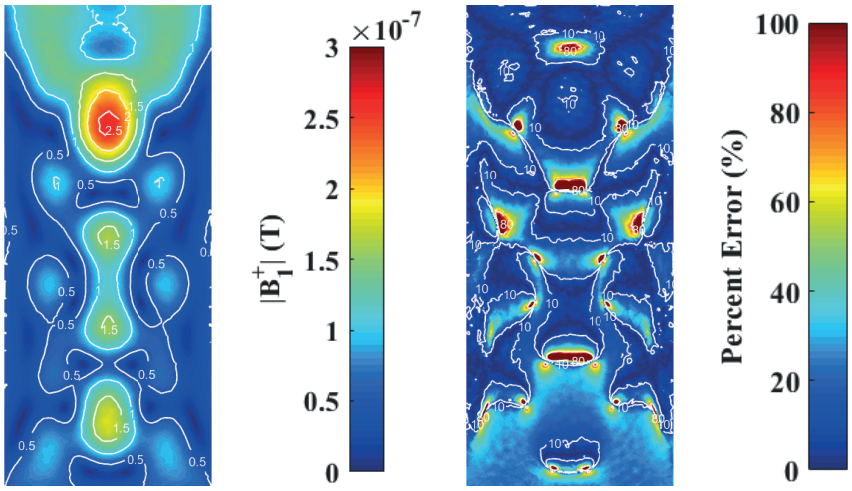

(a)

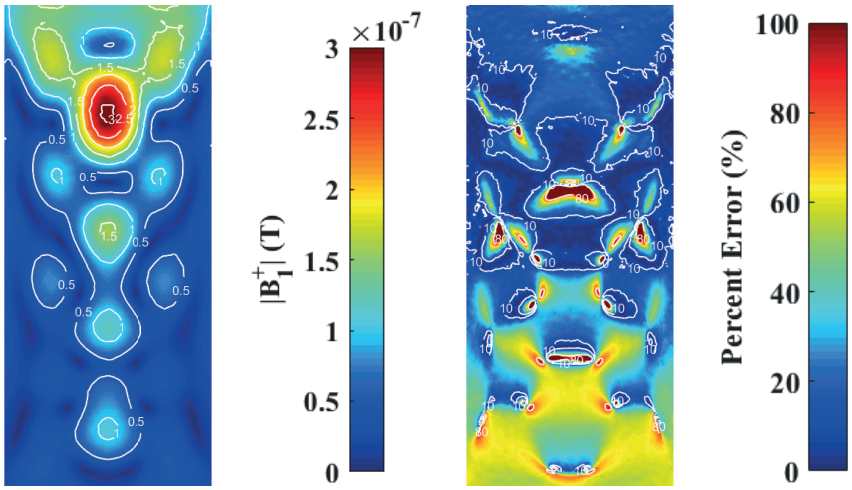

(b)

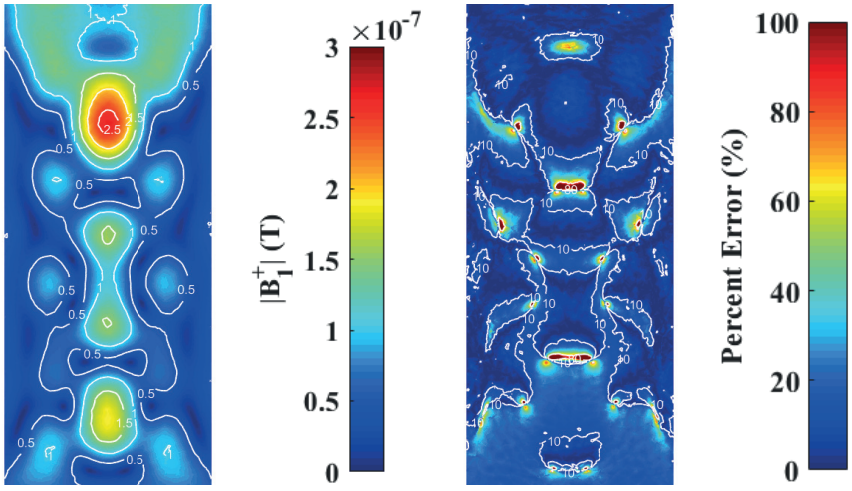

(c)

Figure 3.20: Simulated results (left) and percent error (right) for: (a) radiation boundary around the gradient coil (b) no bore or gradient region present (c) radiation boundary on the end face of the gradient coil.

simple and short, the complexity must increase in order to improve the homogeneity of the excited B-field. This quickly increases the simulation time. Additional steps can be taken to improve the simulation by modifying HFSS solver parameters, however, these are specific to the application and will not be explored.

3.6 Conclusion

This chapter has shown single patch probe excitation benefits and difficulties. The patch probe can be placed a significant distance from the imaging volume (d=15-25 cm) for improving patient comfort. Unfortunately with only a single probe, the spatial coverage for the received power is low and the image quality suffers. Using a copper strip array can improve the coupling for the transmit and receive, and depending on the structure, it can modify the excited modes inside the imaging volume. At 10.5 T the copper strip array did not perform as well as expected compared to simulations. However, this is not surprising since it was designed for 7 T use. Further simulations will be necessary to determine how to optimize the approach at 447 MHz. Two patch probes were used to show benefits of B_1 shimming. By phasing two probes together with and without a copper strip array, the region of interest can be shifted along the phantom. These initial investigational setups described in the current study were not tailored to MRI clinical settings, and produced RF excitation that would not extend through the whole human body. However, it is anticipated that further developments may result in better coverage, including phasing traveling wave probes together as they wrap around the imaging volume. These results are reported in IEEE Transactions on Microwave Theory and Techniques titled, "Patch-Probe Excitation for Ultra-High Magnetic Field Wide-Bore MRI" [69] and a unpublished poster at the 24th meeting of the International Society for Magnetic Resonance in Medicine (ISMRM), 2016, titled "Control of Excited Modes in Ultra High Magnetic Field MRI with Electrically Hard Surfaces".

Chapter 4

Excitation and Field Control of a Human-Size 10.5-T MRI System

Contents

4.1 Introduction

Experiments in this chapter are done at the Center for Magnetic Resonance Research (CMRR) at the University of Minnesota, Minneapolis, Minnesota. This chapter addresses the problem

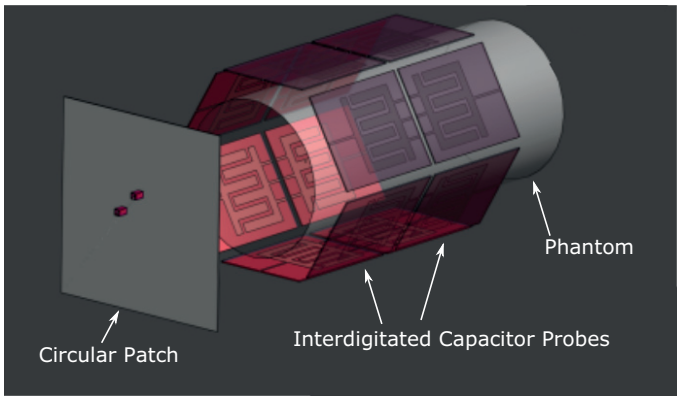

(a)

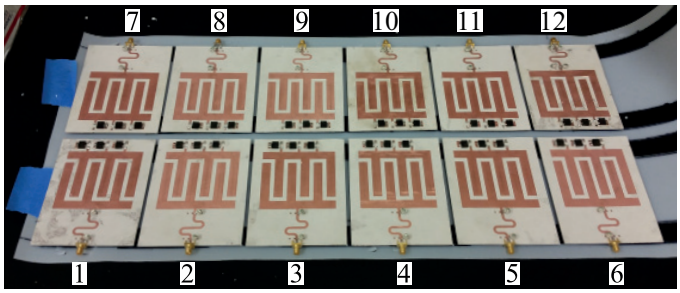

(b)

Figure 4.1: (a) Simulation setup (Sim4Life) showing cylindrical phantom surrounded by interdigitated capacitor probe array with patch probe excitation. (b) Fabricated interdigitated capacitor probe array.

of inhomogeneous B_1^+ in the imaging volume due to complex field profiles associated with the electrically-large size of the bore and imaging volume. Excitation geometries and passive electromagnetic structures that can modify the field profiles and improve field uniformity are investigated in simulations and measurement. Due to the complex nature of the fields inside of the imaging volume, these are not a complete solution, but instead present a study on possible ways to improve homogeneity inside of a uniform phantom, the worst-case scenario. Excitation probes are designed using full-wave EM analysis and experimentally validated and quantified in a human-size 90-cm diameter 10.5-T Siemens scanner at the Univ. of Minnesota Center for Magnetic Resonance Research (CMRR) using a homogeneous water phantom (ϵ_r=81, σ_d=0.4). We show that non-uniform imaging volumes, such as a NIST phantom and a pineapple, inherently have improved B_1^+ field uniformity. After the probe and passive field modifier designs are validated, simulations are performed

with an anatomically accurate human model from the IT'IS virtual population. A distribution comparison is presented in terms of B_1^+ and specific absorption rate (SAR) in the imaging volume.

The chapter outline is as follows: Section 4.2 shows the system configuration, probe design and excitation scheme, and different phantom wall boundary field modifier structures. Section 4.3 and 4.4 quantify the water phantom simulations and experiments. The water phantom is the worst-case scenario in terms of homogenizing the B_1^+ field due to resonances inside of the phantom. Section 4.6 explores the use of two inhomogeneous imaging volumes, the NIST phantom (similar to [70]) and a pineapple, to highlight the differences with a homogeneous water phantom. Section 4.7 uses an anatomically correct human body model from the Virtual Population developed by IT'IS (Zürich, Switzerland) to show how the demonstrated probes and additional conductive structures that modify the electromagnetic fields can be used to develop a head excitation scheme.

4.2 System Configuration

The overall system configuration is described in Fig. 4.2a. MR experiments were collected at the CMRR, on a prototype 90 cm diameter whole body MR scanner (Siemens, Erlangen, Germany) operating at 10.5 T, equipped with an insert body gradient coil of 67 cm inner diameter as shown in Fig. 4.2a. The gradient coil is 125 cm long with a spherical encoding region of about 40 cm in diameter, co-centered with the magnet isocenter. The complete length of the bore is 443 cm. The metal bore is a circular waveguide where the unloaded cutoff frequency of the fundamental TE_{11} mode is given by [62]

$$f = \frac{0.293}{a\sqrt{\mu\varepsilon}} = 262.4\,\text{MHz} \tag{4.1}$$

where a is the radius under the gradient coil equal to 67 cm. Without loading, the gradient coil supports three propagating modes. When loaded with a high dielectric constant volume, the number of propagating modes increases, complicating the homogenization of the imaging volume.

The necessary RF spin excitation frequency is given by

$$f = \gamma\, B_0, \tag{4.2}$$

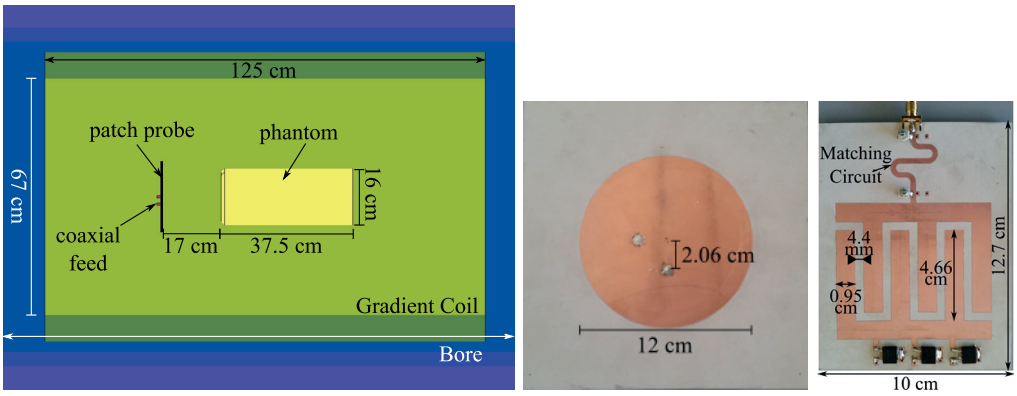

(a) (b) (c)

Figure 4.2: (a) Dimensions of the 10.5 T Siemens scanner with cylindrical phantom shown from the side. (b) Coaxially quadrature fed circular patch probe and (c) interdigitated capacitor probe designed for 447 MHz.

where γ is the gyromagnetic ratio of the H^1 nucleus, 42.58 MHz/T, and B_0 is the DC magnetic field of 10.5 T. The increase in excitation frequency to 447 MHz, compared to clinical scanners at 1.5 T (68 MHz) and 3 T (127 MHz), reduces the wavelength inside of the imaging volume. The imaging volume becomes electrically large and standing waves develop in contrast to the traditional quasi-static approximation used to design RF coils. The dielectric phantom used in experiments is the Siemens 55 12 608 K2205 with a 16 cm diameter and 37.5 cm length. The phantom is filled with DI water of $\varepsilon_r = 81$ and $\sigma_d = 0.4$ S/m.

The RF portion of the MR system includes up to 32 receive channels as well as 16 independent transmit RF channels allowing for different transmit RF phases for each of the individual RF elements. A specific set of relative transmit RF phases is referred to as B_1 shimming. Each RF channel is powered by a 1 kW RF amplifier. Any RF coil element could be utilized during both RF transmission and signal reception using a multi-channel T/R switch board built at CMRR.

Two imaging protocols were used for images reported here: $|B_1^+|$ mapping and conventional gradient echo images (GRE). $|B_1^+|$ maps were obtained with the 3D Actual Flip Angle (AFI) technique [71]. It should be noted that, wherever receive or transmit local B_1 fields are very weak, $|B_1^+|$ may not be measurable because of either limited SNR or too small flip angle. Thus, it is typical to obtain patchy measured $|B_1^+|$ maps at very high fields in a dielectric phantom. Conventional

GRE images were collected in a relatively small flip angle regime, a condition where image intensity is typically proportional to the product of the magnitude transmit B_1 field and the square root of sum of squares of the 12 magnitudes of the receive B_1 fields.

For phantom experiments, the sets of relative RF phases (i.e. B_1 shimming) applied to the transmit channels were defined based on electromagnetic simulations conducted in Sim4Life (see corresponding tables throughout the manuscript).

For data obtained in a pineapple, with its long axis parallel to the longitudinal B_0 axis, an additional imaging protocol was used to obtain multi-channel relative complex $|B_1^+|$ map, consisting of multi-slice 2D GRE images series obtained by pulsing sequentially on one transmit channel at a time while receiving on all receive channels [72, 73]. B_1 shimming was then performed in an region of interest elongated along the Z axis covering the central core of the pineapple with an algorithm aiming at maximizing constructive interferences between the complex $|B_1^+|$ field of all transmit coils [74].

In all experiments, B_1 shimming was applied by only varying relative transmit RF phases between channels.

4.2.1 Circular Patch Probe

A quadrature circular patch is an effective traveling-wave MR probe [20]. The circular spatial current density distribution on the probe excites a circularly polarized field in the cylindrical bore as shown in [69]. A similar coaxially fed patch is designed on a Rogers 3010 substrate, $\varepsilon_r = 11.2$ and 1.27 mm thick, shown in Fig. 4.2b. The probe is designed with no additional matching circuit and has a return loss greater than 15 dB over a 10 MHz bandwidth. Its diameter is 12.28 cm and the feeds are spaced 2.06 cm from the center of the patch to maintain a low axial ratio and high return loss. In free space, the probe is a well-matched resonant patch antenna. The return loss remains high when the probe is inside the electrically-large bore at this frequency, since it is placed at a reasonable distance from the imaging volume, > 10 cm and is therefore not heavily loaded. The ground plane is cut to a 20 cm x 20 cm square to align the center of the patch with the phantom.

The coaxial quadrature feed allows phase and amplitude scaling of the feeds for either sense (right or left) of circular polarization and B_1 shimming. Referring to Fig. 4.2a, the 17 cm distance from the dielectric phantom is a trade-off between circular polarization quality and excitation field magnitude.

4.2.2 Interdigitated Capacitor Probe

Traveling wave excitations have poor spatial coverage of the imaging volume, reducing the overall signal level coupled back into the probe for the received image. An interdigitated capacitor probe [75] is created to improve on this major drawback, Fig. 4.2c. This probe is designed on Rogers 6010, $\varepsilon_r = 10.6$, 1.27 mm thick substrate. The finger dimensions are chosen to ensure uniform current distribution across the two middle fingers while maintaining a high return loss. The combination of the number of fingers and finger width will affect the loading and current distribution on each finger. The design is chosen to target the loading to create a balanced current distribution on the inner two fingers. The interdigitated capacitor probe is a traveling wave probe, and as such needs appropriate resistive loading to eliminate a standing wave across the probe. Reactive loading can also be used, [76], but is prohibitively large for this application and number of radiating elements. Simulations show that a 25 Ω load would allow 30% of the power to be dissipated in the load. Instead of a single resistor, three 75 Ω resistors are used to satisfy the traveling wave condition while balancing the current across the three pairs of fingers. Simulations also showed that adequate loading for probes could be accomplished by using the high permittivity imaging volume as the primary load and that the resistors had little overall impact on the current distribution. Since the primary goals of this work is the development of boundary structures for improving field homogeneity for the transmitted B_1^+, the resistors are kept in order to reduce the number of experimental variables, at the cost of increased noise.

The Rogers 6010 substrate exhibits a substantial anisotropic variation in permittivity across the 12.7 cm x 12.7 cm panel. To compensate for this unknown variation, a Π matching network is designed using two 250 V shunt mechanically variable capacitors and a length of line shown in Fig.

4.2c. The variable capacitors are tuned to have a narrowband frequency response where the return loss is greater than 15 dB at 447 MHz.

Twelve interdigitated capacitor probes are wrapped 60° apart and in two rows (or rings) around the dielectric phantom, as shown in Fig. 4.1a. Simulating this electrically large structure presents some issues. For example, since FDTD solvers require rectangular voxels, the diagonal interdigitated capacitor probes are meshed incorrectly. Regardless of the mesh size, the top radiating copper layer is over- or under-approximated and the results become inaccurate. With a near-field excitation, the currents along the radiating element greatly affect the resulting field. To alleviate this issue, each probe is aligned with the mesh, and the domain is rotated around the probe. This ensures proper meshing of each radiating element and the resulting field can then be scaled, phased, and recombined using superposition to determine the overall field excitation. The FDTD solver, Sim4Life, is chosen in particular due to the ease of use with an anatomically correct human body model and electrical parameters for the given excitation frequency. A single HFSS simulation determines the coupling between the 12 probes is less than -30 dB in the worst case for each element. Simulations show this is due to the close vicinity of the high permittivity dielectric.

4.3 Probe Validation with Water Phantom

The first experimental validation is performed with probes to evaluate the accuracy of full-wave FDTD simulations. Specifically, simulated $|B_1^+|$ transmit efficiency is compared qualitatively to the Gradient Echo (GRE) images and quantitatively to measured $|B_1^+|$ maps with the Siemens 10.5 T scanner using the standard water phantom. The efficiency of the experimental results are expected to be lower than simulations because excitation power is not calibrated to the connection of the probe elements. Additionally, some black speckles in the plots are due to miscalibrations of the scanner, resulting in a loss of data at that point.

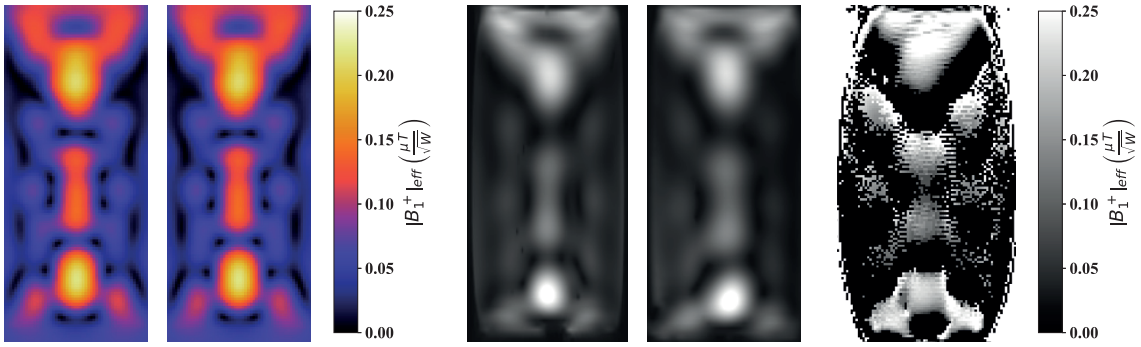

(a) (b) (c)

Figure 4.3: Single circular patch probe: coronal (left) and sagittal (right) (a) simulated $|B_1^+|$ efficiency, (b) measured GRE images, and (c) measured $|B_1^+|$ efficiency inside of cylindrical phantom. Geometric distortions (barreling aspect) of $|B_1^+|$ are due to uncorrected non-linearity of the gradient coils.

4.3.1 Circular Patch Probe

Referring to Fig. 4.2a, the patch is placed 17 cm away from the phantom and the two feeds are excited in quadrature, or 90° out of phase, and with an equal power. Either circular polarization can be excited by varying the relative 90° phase difference. The phantom is placed in the isocenter of the bore and excited with an absolute flip angle imaging (AFI) sequence. Fig. 4.3 shows the results with the single circular patch probe. The efficiency, in $\mu T/\sqrt{W}$, from the simulation in Fig. 4.3a correlates well with the experimental result in Fig. 4.3b and 4.3c. Due to system imperfections and very low SNR in $|B_1^+|$ maps in locations where $|B_1^+|$ is weak, the exact excitation magnitude and phase will vary slightly from the desired value. For this experiment, the variations are fairly low and the experimental result is similar to the simulated result shown in Fig. 4.3a. The absolute $|B_1^+|$ map can be seen in Fig. 4.3c to also have good agreement with the simulated response. The magnitude of the efficiency map is slightly higher than expected due to the uncorrected geometric distortion.

The efficiency is calculated on the coronal slice as the AFI sequence images coronal cuts and therefore only one cross-section is shown. Agreement between the efficiency map and experimental image is expected in this case as the transmit and receive profiles of the single patch probe experi-

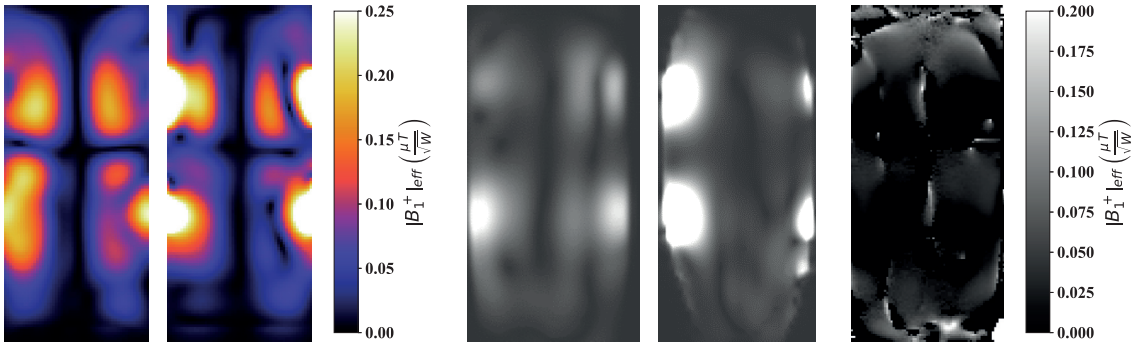

(a) (b) (c)

Figure 4.4: Interdigitated capacitor probe array: coronal (left) and sagittal (right) (a) simulated $|B_1^+|$ efficiency, (b) measured GRE images, and (c) measured $|B_1^+|$ efficiency inside of cylindrical phantom. 60° incremental phasing with equal magnitude excitation on the interdigitated capacitor probes. Geometric distortions (barreling aspect) of $|B_1^+|$ are due to uncorrected non-linearity of the gradient coils.

ment should be similar by reciprocity, because the left and right handed circular polarizations are identical. With more complicated excitations, which are phased relative to each other, this will not be the case and the simulation should correlate with the efficiency map and vary slightly from the GRE images. As the GRE images are approximately proportional to the product of the transmit and receive profiles, their spatial pattern can vary and may have limited consistency with transmit B_1 simulation.

4.3.2 Interdigitated Capacitor Probe Array

To improve the spatial distribution around the phantom and the field distribution inside of the phantom, a volume excitation system is created from interdigitated capacitors. Two rows (or rings) of 6 probes are wrapped around the phantom as shown in Fig. 4.1a for a total of 12 additional excited ports compared to the circular patch probe setup. With the correct sequential phasing, the array can transmit either circular polarization. The field distribution can additionally be improved by varying the magnitudes and phases of individual element. For all plots in the following sections, the coronal slice is shown on the left and the sagittal on the right.

The interdigitated capacitor probe array, Fig. 4.1b, is held in place using 0.5 mm plastic with

Table 4.1: Relative Phase Excitations for the Patch Probe and Array Combination (Fig. 4.5)

1	**2**	**3**	**4**	**5**	**6**
74°	164°	180°	228°	274°	339°
7	**8**	**9**	**10**	**11**	**12**
169°	236°	273°	298°	334°	19°

hook and loop fasteners for flexibility. The probes are placed 3 cm from the phantom to ensure minimal coupling between the elements. The probes are initially simulated and measured separately with a 60° sequential phase difference around the phantom to achieve circular polarization. The probes are excited with the same magnitude to reduce the number of variables when comparing to simulations, as each excitation port has a small magnitude and phase variation from the mean. Fig. 4.4 shows the expected result using Sim4Life and the experimental result. The efficiency result in Fig. 4.4c is expectedly low as it is the center coronal slice, between two probe elements.

4.3.3 Combining the Two Probes

Combining the interdigitated capacitor array with the traveling-wave circular patch can improve the overall field distribution to a targeted region of interest inside the phantom. The relative phasing that minimizes the change in $|\mathrm{B}_1^+|$ is found using a least squares algorithm. The two goal functions are defined as,

$$min\ \frac{|\nabla\,|B_1^+||}{\mu_{|B_1^+|}} \quad \text{and} \quad min\ \frac{\sigma_{|B_1^+|}}{\mu_{|B_1^+|}} \tag{4.3}$$

where μ and σ are the mean and standard deviation of $|\mathrm{B}_1^+|$. Because the variation of the power amplifiers, T/R switch modules, and overall path lengths are not calibrated, only the relative phasing is modified in order to reduce the number of variables to compare the results to simulations. For all practical purposes, the system is capable of varying relative amplitudes between channels. For the phantom results, the region of interest is a 14 cm wide cylinder covering all but the edges of the phantom. While such a large region might be unrealistic, it illustrates clearly the differences between the various excitation schemes.

Combining the two approaches increases the overall efficiency in the areas of interest. Even

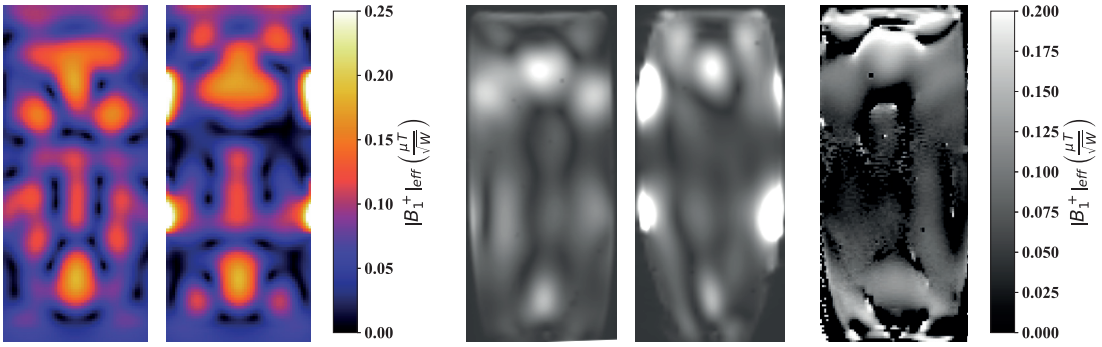

(a) (b) (c)

Figure 4.5: Circular patch probe and interdigitated capacitor probe array: coronal (left) and sagittal (right) (a) simulated $|B_1^+|$ efficiency, (b) measured GRE images, and (c) measured $|B_1^+|$ efficiency inside of cylindrical phantom. Phasing shown in Table 4.1 and magnitude excitations a quarter of the magnitude of the circular patch.

though the overall excitation power increases, the peak magnitude does not increase substantially, indicating power being distributed elsewhere in the phantom. The location of the array is chosen to improve the excited field distribution. The phases chosen to excite the array relative to the patch phase are shown in Table 4.1, with the probe order from Fig. 4.1b. The magnitude of the excitation is set to 25% of the patch excitation magnitude. If the volume excitation can be placed farther from the phantom, the magnitude of the excitation can be increased to reduce the near-field shown in the coronal slice. The circular patch probe is excited with the maximum amount of power available from the RF power amplifiers and in quadrature. The coronal slice correlates well with the simulation shown in Fig. 4.5a, with minor differences due to magnitude and phase variation in the excitation and overall placement of the interdigitated capacitor array. Minor variations in the placement along the phantom's center-axis can shift the excitation. This can be beneficial to complement the distribution due to the traveling-wave excitation. The sagittal slice differs slightly from the simulation as the gradient distortion is not corrected as well as the coronal slice.

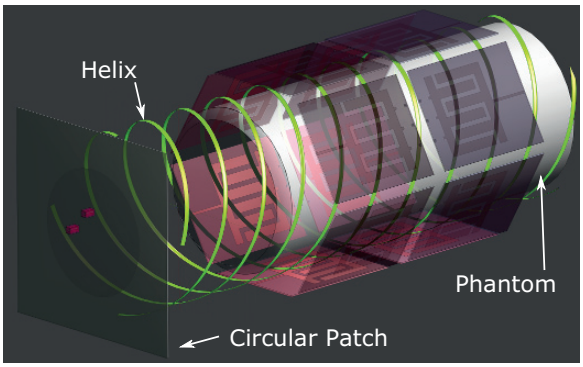

Figure 4.6: Sim4Life setup with the interdigitated capacitor probe array encircling the phantom and helix boundary structure.

4.4 Boundary Condition Modifications

Due to the electrically large size of the phantom, homogenizing the excited $|B_1^+|$ field becomes increasingly difficult for higher field systems due to the increased number of supported modes inside of the dielectric cavity. Typical $|B_1^+|$ shimming can only partially improve the field homogeneity [25]. Additionally, the complex structure of biological tissues can further complicate the excited field profile which can be manipulated using specially designed high permittivity [77] or metallic structures [69]. Three basic passive field modifiers are explored in this chapter: (1) an undriven quadrifilar helix, (2) electrically hard surfaces, and (3) electrically soft surfaces [65].

An un-driven quadrifilar helix, Fig. 4.6 implemented with copper strips on a thin mylar sheet is placed 3 cm from the patch, 1 cm from the phantom, 24 cm from the gradient coil, and has a 5 cm pitch. With the rotation sense following the right-handed circular polarization necessary, the helix can improve the overall efficiency in the far ends of the phantom while improving uniformity in the close end of the phantom, relative to the probe, as shown in Fig. 4.7. The relative phases of the probes can be seen in Table 4.2.

It is interesting to investigate the required helix length since in some cases it may not be practical to cover the entire volume. The helix is reduced to cover 2/3 of the phantom, and the arms are shorted together at the far end. This allows for further homogenization without reducing efficiency, however, the result is fairly asymmetric as shown in Fig. 4.8. The asymmetry is expected from the

Table 4.2: Relative Phase Excitations for the Patch Probe and Array Combination with Strip Helix (Fig. 4.7)

1	**2**	**3**	**4**	**5**	**6**
119°	180°	190°	252°	291°	320°
7	**8**	**9**	**10**	**11**	**12**
180°	335°	24°	44°	69°	136°

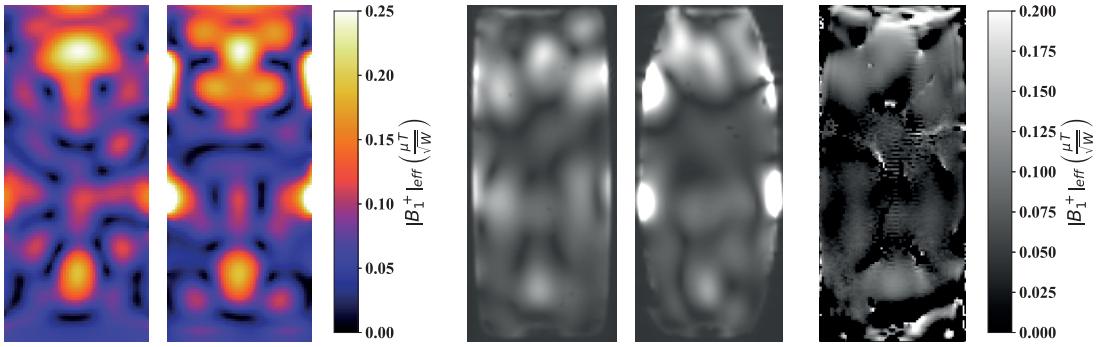

(a) (b) (c)

Figure 4.7: Circular patch probe and interdigitated capacitor probe array with quadrifilar strip helix: coronal (left) and sagittal (right) (a) simulated $|B_1^+|$ efficiency, (b) measured GRE images, and (c) measured $|B_1^+|$ efficiency inside of cylindrical phantom. Phasing shown in Table 4.2 and magnitude excitations a quarter of the magnitude of the circular patch. Geometric distortions (barreling aspect) of $|B_1^+|$ are due to uncorrected non-linearity of the gradient coils.

simulation, Fig. 4.8a, however, the effect is more pronounced in the experimental results, possibly due to magnitudes and phases deviating slightly from simulated values. The phase excitations for the shorted helix are shown in Table 4.3.

Other boundary structures that can affect field uniformity are electrically hard and soft surfaces as shown previously in [69]. Electrically hard surfaces are longitudinal corrugations used in horn antennas, to increase aperture efficiency by distributing the field more uniformly across the aperture, characterized by H_{lon}=0 along the boundary [64], [65]. Electrically soft surfaces are transverse corrugations, characterized by H_{tan}=0 along the boundary, that gives zero electric field at the wall, reducing the side lobe level and broadening the beamwidth, [64]. For these experiments, electrically hard and soft surfaces are approximated with longitudinal and transverse strips, respectively, significantly reducing their size. With an approximation to an electrically hard surface covering the

Table 4.3: Relative Phase Excitations for the Patch Probe and Array Combination with Shorted Strip Helix

1	**2**	**3**	**4**	**5**	**6**
116°	189°	201°	275°	297°	343°
7	**8**	**9**	**10**	**11**	**12**
1°	2°	30°	63°	79°	160°

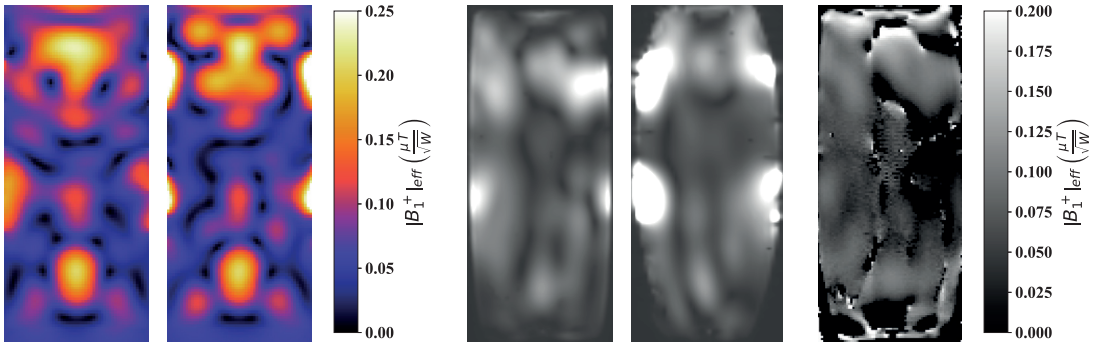

(a) (b) (c)

Figure 4.8: Circular patch probe and interdigitated capacitor probe array with shorted quadrifilar strip helix: coronal (left) and sagittal (right) (a) simulated $|B_1^+|$ efficiency, (b) measured GRE images, and (c) measured $|B_1^+|$ efficiency inside of cylindrical phantom. Phasing shown in Table 4.3 and magnitude excitations a quarter of the magnitude of the circular patch. Geometric distortions (barreling aspect) of $|B_1^+|$ are due to uncorrected non-linearity of the gradient coils.

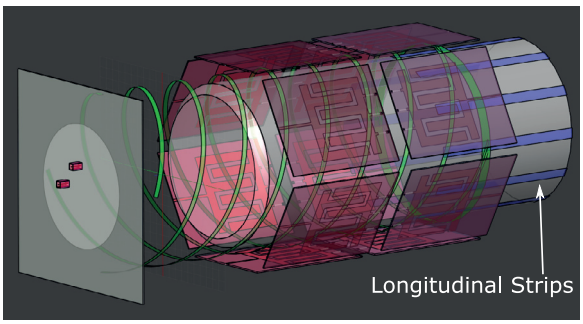

Figure 4.9: 10.5 T simulation setup showing longitudinal strips approximating an electrically hard surface added to the previous setup in Fig. 4.6.

bottom third of the phantom, the results in Fig. 4.10, and specifically Fig. 4.10c show improved field distribution in the upper and middle regions of the phantom. The strip structure is composed of twelve 15.7 cm long strips. The longitudinal strips result in the distribution spreading in the latter portions of the phantom as shown in Fig. 4.10a.

Table 4.4: Relative Phase Excitations for the Patch Probe and Array Combination with Shorted Strip Helix with Longitudinal End Strips (Fig. 4.10)

1	**2**	**3**	**4**	**5**	**6**
112°	166°	176°	257°	284°	310°
7	**8**	**9**	**10**	**11**	**12**
1°	15°	69°	103°	129°	200°

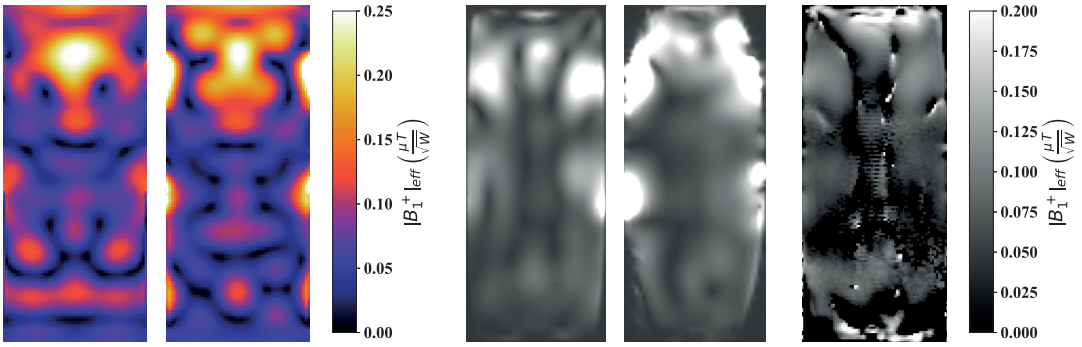

(a) (b) (c)

Figure 4.10: Circular patch probe and interdigitated capacitor probe array with quadrifilar strip helix and longitudinal end strips: coronal (left) and sagittal (right) (a) simulated $|B_1^+|$ efficiency, (b) measured GRE images, and (c) measured $|B_1^+|$ efficiency inside of cylindrical phantom. Phasing shown in Table 4.4 and magnitude excitations a quarter of the magnitude of the circular patch. Geometric distortions (barreling aspect) of $|B_1^+|$ are due to uncorrected non-linearity of the gradient coils.

With an approximation of an electrically soft surface using seven rings of lateral strips wrapped around the circumference of the cylinder, Fig. 4.12c shows an increase in field homogeneity in the phantom. This results in a higher field amplitude in the center of the phantom as shown in Fig. 4.12a. Unfortunately, metallic strips will increase the specific absorption rate (SAR) along the boundary if they are placed directly on the surface. A thin dielectric can be used as an intermediate boundary layer to reduce the impact of the metallic structure at the cost of a reduced effect of the boundary structure, as is easily shown by simulations.

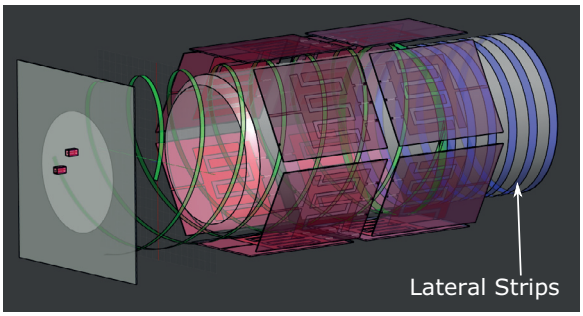

Figure 4.11: Setup showing lateral strips approximating an electrically soft surface.

Table 4.5: Relative Phase Excitations for the Patch Probe and Array Combination with Shorted Strip Helix with Lateral End Strips (Fig. 4.12)

1	**2**	**3**	**4**	**5**	**6**
1°	38°	99°	128°	152°	221°
7	**8**	**9**	**10**	**11**	**12**
74°	107°	188°	202°	259°	310°

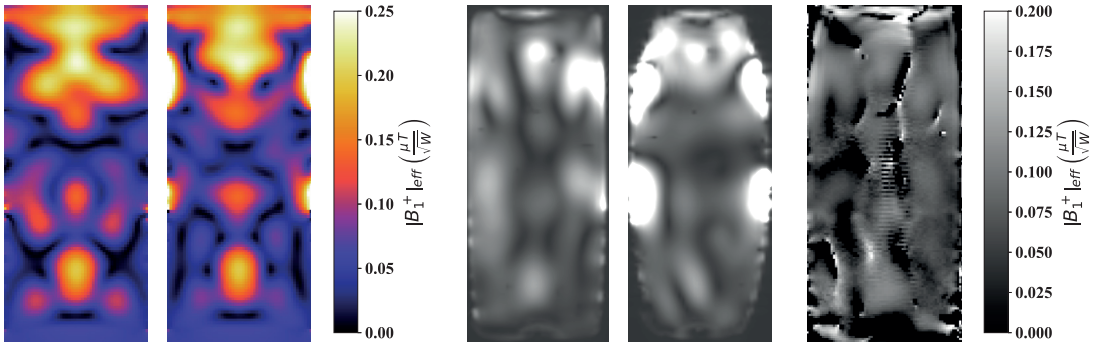

(a) (b) (c)

Figure 4.12: Circular patch probe and interdigitated capacitor probe array with quadrifilar strip helix and lateral end strips: coronal (left) and sagittal (right) (a) simulated $|B_1^+|$ efficiency, (b) measured GRE images, and (c) measured $|B_1^+|$ efficiency inside of cylindrical phantom. Phasing shown in Table 4.5 and magnitude excitations a quarter of the magnitude of the circular patch. Geometric distortions (barreling aspect) of $|B_1^+|$ are due to uncorrected non-linearity of the gradient coils.

Table 4.6: MSE Between Simulation and Experiment

Experiment	**MSE Coronal (%)**	**MSE Sagittal (%)**	**Eff. Map (%)**
Circular Patch Probe	1.2	1.5	8.4
Interdigital Capacitor Probe Array	3.8	3.8	16
Combination	3.6	4.8	9.7
Strip Helix	4.8	4.5	5.7
Shorted Strip Helix	5.1	7.9	6.7
Helix with End Long. Strips	5.6	8.5	7.8
Helix with End Lat. Strips	6.2	9	7

4.5 Statistical Result Comparison

The simulated results are compared to the experimental results using mean square error,

$$MSE = \frac{1}{N}\sum_{i=1}^{N}(X - Y)^2 \tag{4.4}$$

where X are the simulated and Y are the N experimental data points, N=153344, with results in Table 4.6. Some minimum error is expected due to the difference between the simulated and GRE DICOM results, subfigures (b) of the preceding result figures, due to the transmit and receive multiplication, along with the sagittal slices having a large uncorrected geometric distortion. Differences between the simulated and experimental efficiency maps are generally due to regions with low SNR that are not properly mapped to an efficiency value. For this reason, the error in the interdigitated capacitor probe array experiment is large because of the over-saturation of the region closest to the probes at the center slice. Additionally, due to a slight over estimation of the circular patch probe efficiency in the combined case, the results reduce the effect of the interdigitated capacitor probe array and create additional error in the comparison. For the cleaner coronal cut results, the error stays below 7%.

A comparison of the simulated results is used to determine the effectiveness of the boundary structures using the four statistical moments, mean, variance, skewness, and kurtosis based on the probability density shown in Fig. 4.13 with 200 bins for 291719 points. The non-Gaussian nature of

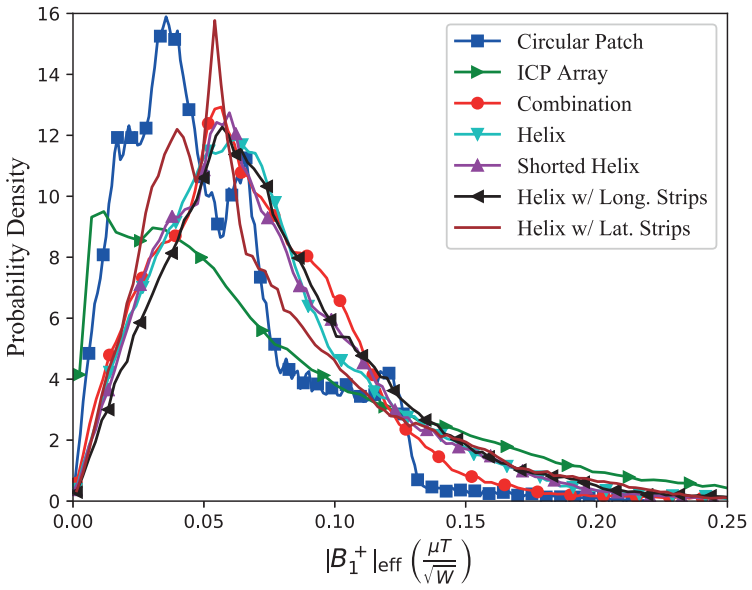

Figure 4.13: Probability density of the magnitude B_1^+ efficiency for various configurations. The results from the helical structure with longitudinal and lateral strips show a trend towards Gaussian behavior.

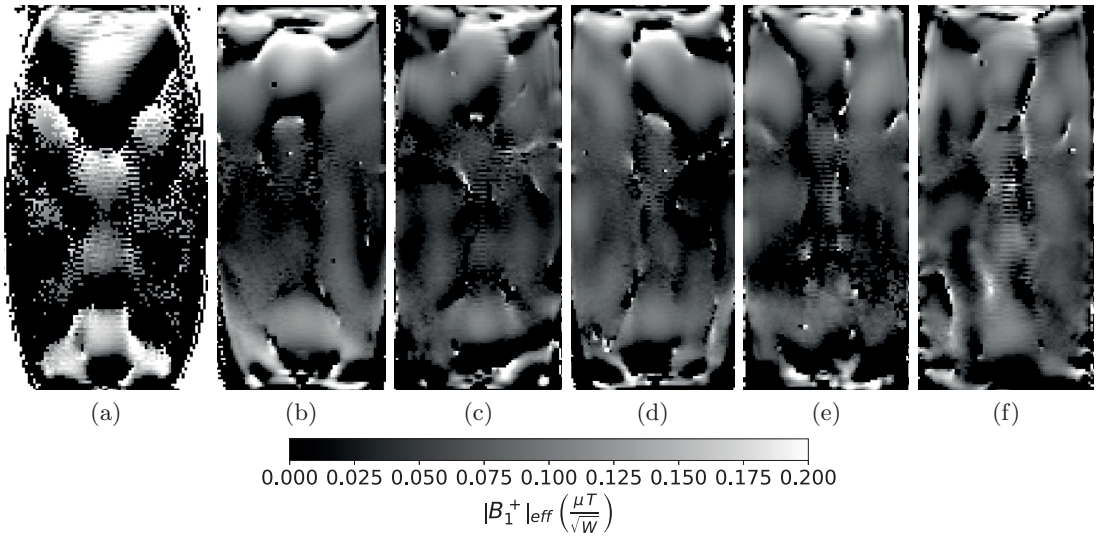

Figure 4.14: Experimental efficiency comparison for (a) single patch probe, (b) combination single patch probe and interdigitated capacitor probe array, (c) strip helix, (d) shorted strip helix, (e) shorted strip helix with longitudinal end strips, and (f) strip helix with lateral end strips.

Table 4.7: Four Moment Statistical Simulation Comparison in ($\mu T/\sqrt{W}$)

Simulation	**Max**	**Mean**	**Variance**	**Skewness**	**Kurtosis**
Circular Patch Probe	0.22	0.054	0.0012	0.912	0.843
Interdigital Capacitor Probe Array	0.93	0.086	0.0075	2.795	12.43
Combination	0.50	0.071	0.0018	2.08	9.83
Strip Helix	0.51	0.078	0.0022	1.77	6.30
Shorted Strip Helix	0.49	0.075	0.0021	1.74	6.21
Helix with End Long. Strips	0.48	0.078	0.0022	1.61	5.17
Helix with End Lat. Strips	0.48	0.073	0.0024	1.66	4.44

Table 4.8: Normalized Four Moment Statistical Experiment Comparison

Experiment	**Mean**	**Variance**	**Skewness**	**Kurtosis**
Circular Patch Probe	0.47	0.19	0.054	-1.79
Interdigital Capacitor Probe Array	0.35	0.17	0.079	-1.1
Combination	0.49	0.15	0.17	-1.45
Strip Helix	0.44	0.14	0.43	-1.3
Shorted Strip Helix	0.48	0.14	0.29	-1.28
Helix with End Long. Strips	0.46	0.14	0.34	-1.31
Helix with End Lat. Strips	0.50	0.12	0.28	-1.16

the data requires more than just mean and variance to show how the boundary structures modify the data. A positive skewness generally indicates a higher concentration above the mean. The kurtosis reported is excess kurtosis, or kurtosis centered around 0 instead of 3. An excess kurtosis below 0 implies a platykurtic distribution, focused around the mean. Ideally, the mean should be as high as possible and the skewness should be close to 0, indicating a Gaussian distribution, and the kurtosis should be as small as possible, indicating the distributions are focused towards the mean. Relative to the field produced by the circular patch probe alone (Table 4.7), with each field modifier, the mean is increased by 50%, at the expense of uniformity. However, by

adding increasingly more complex boundary conditions, the skewness and kurtosis both decrease substantially compared to the initial approach with the combination of circular patch probe and interdigitated capacitor probes. The experimental analysis using the efficiency map, normalized to 1, shows a similar trend, as indicated in Table 4.8. With a more complex structure, the mean increases while the variance decreases, with the skewness consistently close to 0 and excess kurtosis remaining relatively consistent around -1.5. The differences in statistics can be partially attributed to a slightly modified experimental setup compared to simulation. The air-capture region of the bottle prevented the helix and end strips from being perfectly circular along with some slack in the interdigitated capacitor probe construction preventing completely equidistant excitations from each element.

A visual comparison of the plots in Fig. 4.14 reveals increased homogeneity with increasing hardware complexity. While these field profiles will change slightly between imaging volumes, the boundary structures will perform similarly. For example, an electrically hard surface will still act as an electrically hard surface.

4.6 Inhomogeneous Imaging Volumes

The $|B_1^+|$ field distribution is difficult to homogenize if the imaging volume is uniform. For example, the simple and symmetric cylindrical shape of the water phantom supports high order resonant modes, increasing the spatial variation. The overall large electrical size of the phantom leads to lower maximum efficiency as the field is distributed over the entire volume. Although useful for simulation validation, a uniform phantom does not accurately describe inhomogeneous human tissues and this effect is more pronounced with higher field systems.

In this section, measurement results for two inhomogeneous phantoms of irregular shape are shown: a NIST standardized system phantom and a pineapple, which is roughly the size of a human head. The phases of the excitations for both inhomogeneous volumes are shown in Table 4.9 with the magnitudes equal across all of the excited ports. The two circular patch ports are excited at

Table 4.9: Relative Phase Excitations for the Inhomogeneous Imaging Volumes (Fig. 4.15 and 4.16)

1	**2**	**3**	**4**	**5**	**6**
112°	313°	145°	111°	40°	335°
7	**8**	**9**	**10**	**11**	**12**
314°	61°	60°	99°	241°	259°

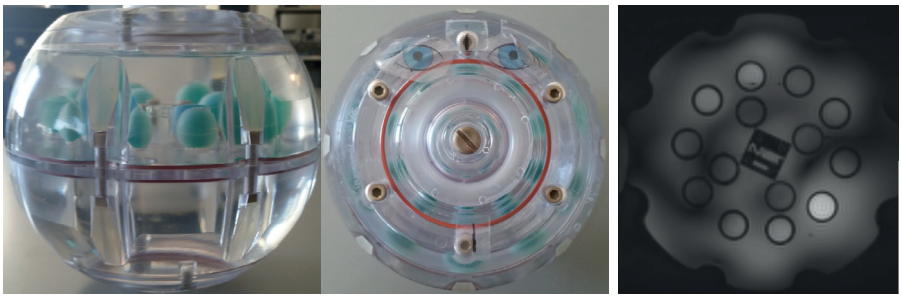

(a) (b)

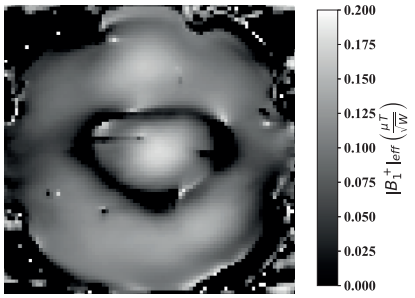

(c)

Figure 4.15: Measured NIST standardized system phantom (a) cross-sections showing the different spheres of materials, (b) GRE image, and (c) efficiency map ($\mu T/\sqrt{W}$).

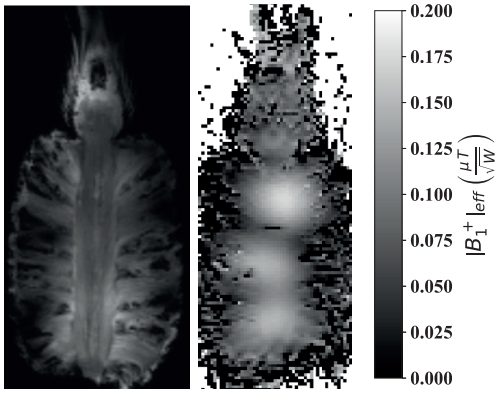

(a) (b)

Figure 4.16: Measured pineapple (a) GRE image and (b) efficiency map ($\mu T/\sqrt{W}$).

163° and 280°. This is slightly off quadrature to account for the imperfect circular polarization of the interdigitated capacitor probe array. These excitations are determined by optimizing the field excitation in the outer-regions of the pineapple, since the high-water content core overpowers the outer regions.

The NIST standardized phantom (Fig. 4.15a) contains various spheres of materials with different T1 and T2 weightings, such that each sphere should appear with different brightness in the resulting GRE image, as shown in Fig. 4.15b. The efficiency is slightly higher than the cylindrical phantom results, Fig. 4.15c, partially due to the smaller size of the phantom.

Fruit is often imaged in MRI systems due to similar electrical properties as human tissues and inhomogeneity of the internal structure. A pineapple was chosen as it is a similar size and structure to the human head. The pineapple is 15 cm long and 11 cm in diameter. Fig. 4.16a shows high resolution details of all parts of the pineapple while Fig. 4.16b shows significantly more field excited towards the high-water content center core. Only one cross-section for both inhomogeneous phantoms is shown and similar efficiency increase is obtained for all cuts.

4.7 Anatomically Accurate Human Body Model

The various excitations described in the previous sections are next used in simulations with *Duke*, an anatomically correct adult male from the IT'IS (Zürich, Switzerland) Virtual Population v3.1 [36]. The model contains 300 bones and tissues with accurate electrical properties across frequency. The relative phasing and magnitude is optimized for the volume of the head from the bottom of the ears to the top of the skull. Normalized $|B_1^+|$ results are shown and the 10 g specific absorption rate (SAR) maps are normalized to the maximum of 3.2 W/kg specified by the IEC 60601-2-33 standard. The simulated plots show a sagittal cut in the center of the body on the right, and a coronal cut in the center of the body on the left. The plots are cropped to roughly the armpits as there is no significant field below the shoulders. First, only a patch probe is simulated, then it is combined with the interdigitated capacitor probe array, and finally an undriven helix is added,

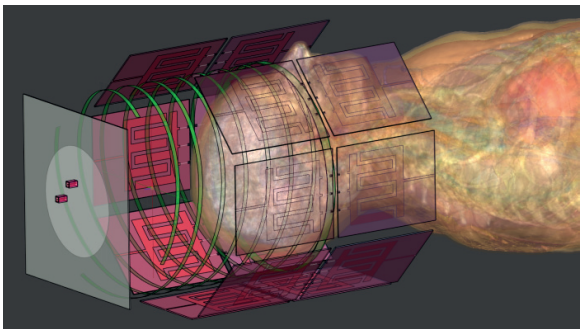

Figure 4.17: Simulation setup showing an anatomically accurate human body model from the IT'IS Virtual Population, *Duke*, with the shorted un-driven quadrifilar helix with circular patch probe and 14 interdigitated capacitor probes.

with the final combination shown in Fig. 4.17.

4.7.1 Patch Probe and Interdigitated Capacitor Probe Array

The circular patch probe is placed 17 cm from the top of the head. Fig. 4.18 shows the resulting excitation with poor field coverage; only the top and the middle of the head are excited with low field coverage on the sides. The peak of the SAR is located in a concave region of the shoulders, which then limits the maximum field excitation in the region of interest.

The interdigitated capacitor probe array is placed such that the chin is at the lower edge of the array, so that the center of the volume excitation is aligned with the brain. The head is larger than the uniform cylindrical phantom therefore the excitation for *Duke* adds an array element for each row, totaling 14 excitations in the array. Top radiating elements are not used as the coverage provided by the elements is already satisfied by the circular patch probe and the elimination of the element will potentially improve patient comfort. The combination of the array and the single circular patch probe can help improve the field coverage inside of the imaging region. The optimized excitation is shown in Table 4.10, where the voltage excitation is normalized to the patch probe excitation. To improve the right-handed circular polarization inside of the head, with the interdigitated capacitor probe array in place, the feeding of the circular patch probe is modified so that it is no longer in quadrature. The imperfect shape of the head will affect the quality of the circular polarization, such that the coronal and sagittal cuts do not see a similar electrical structure.

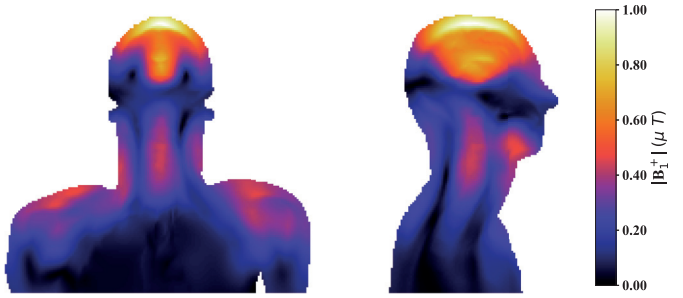

(a)

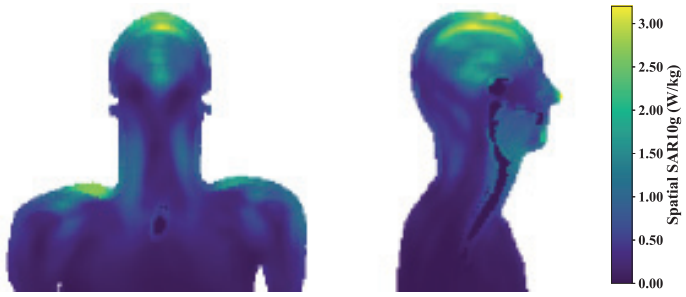

(b)

Figure 4.18: Results inside the head and shoulder volume of *Duke* using the circular patch probe excitation: (a) $|B_1^+|$ and (b) sSAR10g.

The lack of a top radiating element in the interdigitated capacitor probe array further complicates the excitation, requiring a combination of the sources to help maintain a circular polarized field.

The combination of the two excitations helps to improve the magnitude of the field in the outer regions of the head, but much of the inner regions have a low field magnitude. The combination with the interdigitated capacitors shift the unwanted absorption from the shoulders to the imaging region of the head. Practically this is useful because the limiting factor of the field excitation would be the volume being imaged, as opposed to another part of the body. However, there is higher absorption at the tip of the nose which could be reduced through further optimization with explicit constraint on max SAR10g.

4.7.2 Helix Boundary Condition

The un-driven quadrifilar helix is next added with the final configuration containing all elements from Fig. 4.6. The helix pitch is decreased to 3 cm and the separation between the helix and the head remains at 1 cm. The optimized excitation is shown in Table 4.11. The addition of the

Table 4.10: Patch Probe and Interdigitated Capacitor Probe Array Relative Magnitude and Phase Excitation with Duke (Fig. 4.19)

Patch Probe Port	**Magnitude**	**Phase °**
1	1	196
2	1	217
Interdigitated Capacitor	**Magnitude**	**Phase °**
1	1.25	13
2	2.08	63
3	2.08	86
4	2.08	111
5	2.08	181
6	2.08	262
7	2.1	328
8	1	18
9	1.62	58
10	1.45	133
11	1.18	164
12	1.67	208
13	1.68	236
14	1.76	280

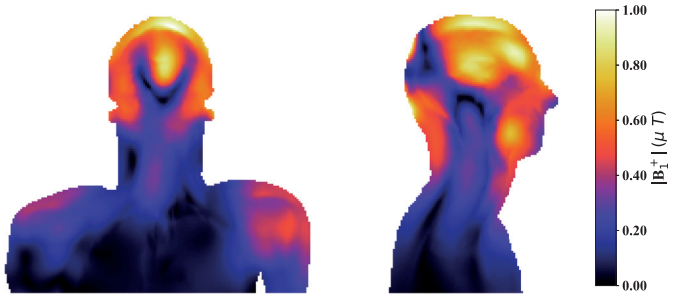

(a)

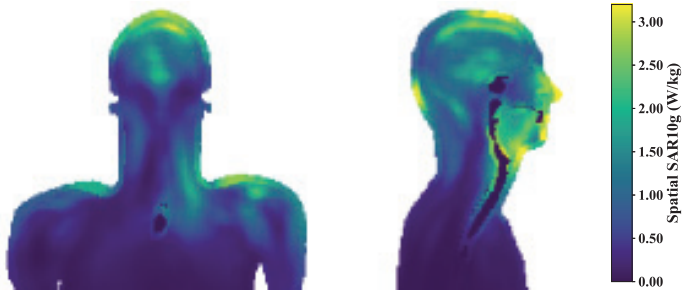

(b)

Figure 4.19: Results inside the head and shoulder volume of *Duke* using the circular patch probe and interdigitated capacitor probe array excitation: (a) $|B_1^+|$ and (b) sSAR10g.

Table 4.11: Patch Probe and Interdigitated Capacitor Probe Array Relative Magnitude and Phase Excitation with Duke and Helix Boundary Condition (Fig. 4.20)

Patch Probe Port	**Magnitude**	**Phase °**
1	1	32
2	1	157
Interdigitated Capacitor	**Magnitude**	**Phase °**
1	0.83	18
2	1.67	91
3	1.67	223
4	1.67	276
5	2.1	321
6	2.08	11
7	2.05	36
8	1.43	1
9	2.06	25
10	0.76	65
11	2.04	104
12	1.47	129
13	0.39	198
14	1.44	261

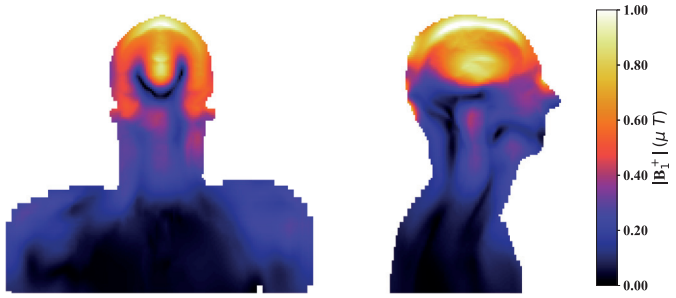

(a)

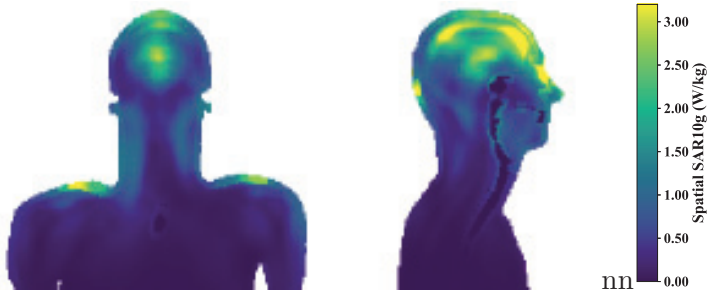

(b)

Figure 4.20: Results inside the head and shoulder volume of *Duke* using the circular patch probe and interdigitated capacitor probe array excitation with shorted helix boundary condition: (a) $|B_1^+|$ and (b) sSAR10g.

quadrifilar helix helps balance the overall magnetic field distribution in the upper region of the head. The field gradient from the outer to the inner region is reduced. With the addition of the helical boundary structure, the phase difference between the circular patch probe feeds is closer to 90° than the previous case as it helps improve on the imbalance created by an imperfect volume. Since the most important part of the head for ultra-high field MRI is the brain, this approach improves the homogeneity in the region of interest. It is interesting to note that the lower portion of the head, roughly even with the nose, is still difficult to excite, but a modified excitation could be designed for a redefined optimized region. The re-focusing of the fields reduces the SAR peaks in the lower portion of the head, and even in the outer regions of the head.

4.8 Conclusion

In summary, this chapter presents an investigation of various designs for the excitation and control of RF electromagnetic fields in a human-size 10.5-T MRI bore. Particular attention is given to methods that have the potential of improving the uniformity of the B_1^+ field inside several types of phantoms. Several conclusions can be made from the simulation and measurement results presented in the chapter. First, FDTD simulations using Sim4Life (Zurich MedTech) are validated by measurements on a uniform cylindrical water phantom using two different types of excitations and their combination, as well as three different passive field modifying structures. The simulated data is compared to measurements, and the measured data are quantitatively compared for various configurations. Although the homogeneous symmetrical phantom fundamentally supports resonant modes and therefore results in large field uniformities, it is found that a combination of a circularly-polarized patch and a traveling-wave capacitively loaded probe gives the largest field homogeneity when combined with a passive quadrifilar helix and soft electromagnetic surface that both surround the phantom.

After validating the simulations with measurements for the uniform water phantom, a second set of measurements is performed on two non-uniform phantoms: a standard NIST phantom and

a pineapple. Both of these phantoms lack the uniformity and symmetry of the water cylinder and show an improved B_1^+ field homogeneity when the same excitation and field modifying devices are used, with a 2.8 times increase in efficiency.

Finally, simulations are performed with an anatomically-correct human body model from the IT'IS virtual population and with the various configurations used in the measurements. The B_1^+ field distribution along with field absorption (SAR10g) in the tissues of the head and shoulder region of a mature male are plotted and analyzed. The best combination of probes and passive field structures that give a more uniform and stronger B_1^+ is found to be the case with the circular patch combined with the interdigitated capacitor probe with a shorted passive quadrifilar helix surrounding the head region.

In conclusion, the chapter demonstrates effective simulations with various levels of imaging volume complexity, as well as validation with a number of measurements on a 10.5-T MRI system. Several techniques for improved RF field excitation and distribution are investigated and compared, showing that the desired circular polarized transmit B-field component can be focused in specific regions by excitation phasing, while maintaining low absorption in the tissues of a human body imaging volume. This work is published in the proceedings of the IEEE International Microwave Symposium, 2017, [78] titled "10.5-T MRI volume excitation using traveling-wave microstrip probes" and Transactions on Microwave Theory and Techniques titled "Excitation and Field Control of a Human-Size 10.5-T MRI System".

Chapter 5

Electrically Large Cavities for Scalable Waste to Fuel Conversion

Contents

5.1 Introduction

This chapter presents the use of an electrically large microwave cavity for the conversion of waste-to-fuel. The military has an over abundance of waste that must be managed from small-scale field operations to large-scale base-wide management. The use of a microwave system to reduce the

waste to a carbon-rich fuel can be beneficial from both a waste management standpoint and to the additional creation of a fuel for cooking and heating.

Accomplishing this task requires multiple techniques to tailor the field distribution inside of the microwave cavity. The loading material inside of the cavity can vary greatly from a low permittivity and low loss material, such as oil, to a high permittivity and high loss material, such as potatoes. An estimation of the effective dielectric constant can be done by using some information based on previous studies of waste management at military bases. This allows targeting of certain material parameters and choosing a realistic size for a microwave cavity to begin the analysis. The cavity analysis begins with a statistical look at how many modes that can be expected inside of the cavity. Then, an eigenmode analysis is performed to observe how these fields will exist inside of the cavity and understand the composition of the modal content as the cavity structure becomes more complicated. To reduce the overall volume of the cavity, a coaxial cavity is created which limits the propagation of the field across the cavity. The center conductor can be used as a platform for a multitude of different components from extra sources to a vent for material. In this chapter, however, it will be used as a platform for a mixing auger which not only mixes the modes, but also mixes the fields. After the undriven approach is analyzed using eigenmode analysis, a wide band double-ridged waveguide is used as an excitation to compare the expected field results to what a driven analysis shows. The analysis, at both 915 MHz and 2.45 GHz, is repeated for the cylindrical cavity, coaxial cavity, and lastly the auger is explored to observe the effect on the driven excitation. With these results, a superposition of sources is used to measure efficiency of the excited electric field with modifications to the relative magnitude and phasing. To close out the analysis of the cavity, a realistic method of feeding is implemented to see how these different methodologies will effect a realistic source with a double-ridge to coaxial connector transition, as opposed to the idealized, simulated waveport. This chapter focuses mainly on 915 MHz and 2.45 GHz sources as it becomes simpler to find commercial high power components, such as magnetrons, due to their availability for high power microwave ovens and transmitters. Additionally, as GaN technology improves, high power and efficient devices are being created for L and S-band radar applications. By developing

excitation schemes for lower power devices, these high power devices can be substituted in to improve heating performance without sacrificing efficiency.

5.2 Material Considerations

One of the largest challenges to this problem is the potential lack of knowledge of the heating volume. The composition of trash can widely vary depending on the time, day, week, month, and year. The city of San Diego had a study done on trash collected at various military bases and published percentages of various materials found [79], with various typical materials highlighted in Table 5.1. The largest concentration was found to be wood, whose microwave characteristics have been studied, such as in [55]. Food represents one of the largest variation, as starches and fatty foods have drastically different permittivities and loss tangents. Fortunately, many of the other materials have similar permittivities around 2 and loss tangents around 0.02. This can simplify initial design to target ranges of effective permittivities and loss tangents.

Table 5.1: Trash Composition From San Diego Military Disposal

Waste	**Percentage (%)**	**Permittivity**	**Loss Tangent**
Wood/Pallets/Crates	29.8	1.2-2.1	0.03 (3 GHz)
Food	10.9	Meat/Potato: 50 Butter(fat): 4.6	Meat/Potato: 0.3-0.5 Butter(fat): 0.13
Molded Plastic	7.6	2-3.5	0.005-0.019
Corrugated Cardboard	6.4	2.5	-
Paper	5.4	2.0	0.03
Textiles	3.4	1.4-6	0.02
Butyl Rubber	–	2.34	0.001

Analyzing material mixing is a fairly old field, beginning with James Clerk Maxwell Garnett in 1904 presenting the mixing formula for a heterogeneous medium [80],

$$\frac{\varepsilon_{eff} - \varepsilon_h}{\varepsilon_{eff} + 2\varepsilon_h} = \sum_{j=1}^{n} f_j \frac{\varepsilon_j - \varepsilon_h}{\varepsilon_j + 2\varepsilon_h} \tag{5.1}$$

where ε_{eff} is the effective permittivity, ε_h is the permittivity of the host medium, ε_j is the permittivity of a component material, and f_j is the fractional content of a material whose sum across

j is 1. This approximation is valid under the assumption that any deviation is smaller than a wavelength and the medium is uniform and isotropic. Later, in 1912, Wiener more generally stated that the complex permittivity of a medium must lie between two limits; a series limit creating a line (5.2), and a parallel limit creating an arc (5.3) between two complex permittivities.

$$\varepsilon_{eff} = f_1\varepsilon_1 + f_2\varepsilon_2 \tag{5.2}$$

$$1/\varepsilon_{eff} = f_1/\varepsilon_1 + f_2/\varepsilon_2 \tag{5.3}$$

Similar to (5.1), (5.2) and (5.3) can be extended to an N component medium using a summation and bound the problem if the fractional content of the medium is well known. Using this information and the information supplied in Table 5.1, with the assumption that the food is half starches/meat and half fat, that the complex relative permittivity will be bounded by 6.71-1.83j (tanδ=0.27) and 2.65-0.092j (tanδ=0.035). If more information can be obtained about the material, or if the material is mixed well, the bounds can be decreased and slowly narrow in on an effective complex dielectric constant. With the same equations and with a general estimate of the material composition, the analysis can be extended to other material parameters, such as thermal conductivity, to gauge how effective the heating of the material will be.

Physically, another issue will be the thermal properties of the system. Each material has significantly different specific heat, mass density, heat capacity, and thermal conductivity. In 1818, Dulong and Petit [81] theorized that the product of specific heat and atomic weight is constant, later found to be about 3R where R is the gas constant. This was found to be generally true, with a few shortcomings such as for gases or at cryogenic temperatures. However, a corollary to this law is that the specific heat mass density product (ρc_p) has a limited range. For most solids, this narrows down to a range of about 1.4-2.5 MJ/m^3K, with water expanding the axis to around 4 MJ/m^3K depending on the salt content. An important part of this statement is that as these parameters change with temperature, specific heat generally increases and mass density generally decreases. Fortunately, this product will generally remain within these ranges and can help simplify the analysis to determine feasibility of a system and how much power could be expected.

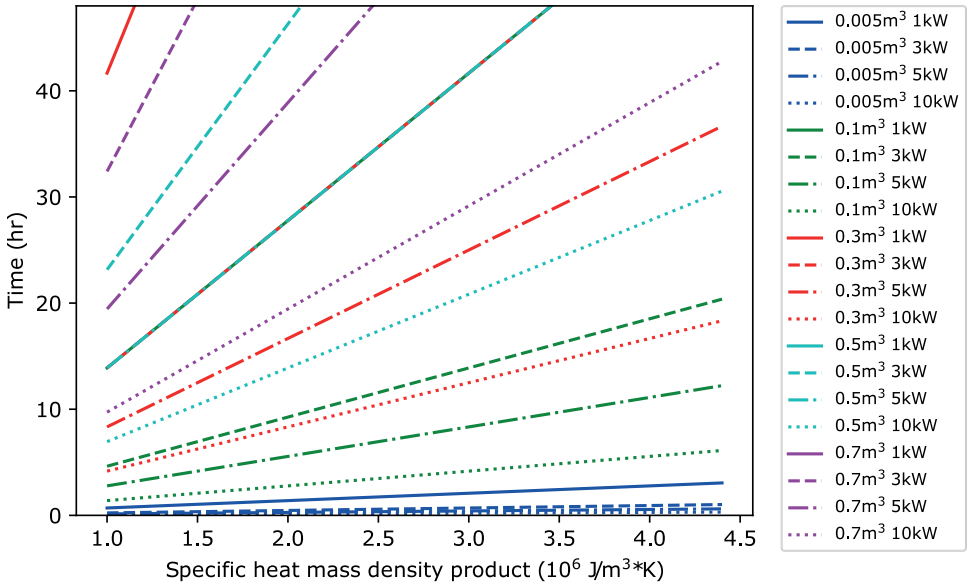

Figure 5.1: Power required for a change in 500°C for various volumes.

From a simplified standpoint, the power required to heat a volume at a given rate is,

$$P = \rho c_p V \frac{dT}{dt} \tag{5.4}$$

where P is power, ρ is mass density, c_p is specific heat, V is volume, T is temperature, and t is time. Visually, this can be seen in Fig. 5.1 and highlight why a commercial counter top microwave oven is so effective. It is relatively simple to heat a small volume quickly with relatively low power.

The next factor to account for is loss tangent. The power absorbed in a dielectric can be shown to be,

$$P_{density} = \sigma |E|^2 = 2\pi f \varepsilon_0 \varepsilon' tan\delta |E|^2 \tag{5.5}$$

where σ is the conductivity, f is the frequency, ε_0 is the permittivity of free space, ε' is the relative permittivity, $tan\delta$ is the loss tangent, and $|E|$ is the magnitude of the complex electric field. So while the specific heat mass density product is high, the loss tangent is also high and will allow for more power absorption compared to low loss materials, such as plastic. While the power absorbed stays constant with volume, the magnitude and distribution of the electric field will have a substantial effect on how much power is necessary to heat a volume.

A more intuitive way to look at the problem will be the necessary average electric field. Fig. 5.2

shows the required average electric field for different rates of heating. For incredibly fast heating of 1°C/s, the average electric field required approaches 20 kV/m at 915 MHz. Due to the electric field scaling with the square root of power and an average efficiency of 70 V/m*$\sqrt{W}$ (using Table 5.5 as a reference), this would require roughly 81.6 kW per source and 670 kW total. For a lower rate of 0.1°C/s, this would be only 5.1 kW per source, and only about 38.8 kW total. As the materials heat, the loss tangent will decrease along with the permittivity, and increasing the power is required to maintain a similar heating rate. This lower bound of the solid line would hopefully be a worst case scenario as the material heats, however, alleviate some concern, the initial composition of the material could be altered to obtain a higher loss tangent. For lumber processing, [55] found that a 15% moisture content hembal will burn wood in just 120 s compared to dry hembal which plateaus at 100°C in 120 s. Albeit, the experimental setup is significantly different due to the smaller heating volume, enabling a higher field density compared to the electrically large cavity shown in this chapter. By adding salt water, the loss of a volume and permittivity of a volume could increase to a desired amount, pre-determined by an analysis of the trash composition. However, this would also decrease the overall excitation efficiency. Instead, metals could be used in small sizes and place periodically inside the volume as an artificial dielectric. These metals will also be reusable as they will melt at a much higher temperature than this system would be capable of. Since metal has a high thermal conductivity, the metal could improve the heating of the volume.

5.3 Electrically Large Cavities

5.3.1 Mode Density

The number of modes supported in an electrically large cavity can be calculated with [82],

$$N_s(f) \approx \frac{8\pi f^3 V}{3c_0^3} \tag{5.6}$$

where N is the smooth mode number, f is frequency (Hz), c_0 is the speed of light in a vacuum (m/s), and V is the volume (m^3). The smooth mode number, (5.6), approximates the number of

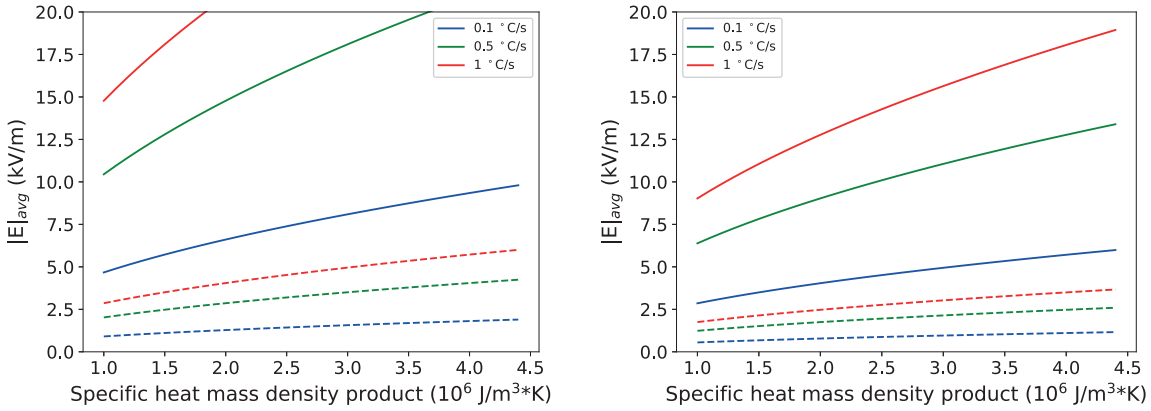

(a) (b)

Figure 5.2: Required |E| for different rates of heating at (a) 915 MHz and (b) 2.45 GHz where (solid) ε_r=3 tanδ=0.03 and (dashed) ε_r=8 tanδ=0.3.

TE and TM modes in an empty cavity. Filling the cavity with a high permittivity volume will increase this number by the square root of the relative permittivity. If it becomes necessary to change the possible excited mode distribution,

$$\Delta V \approx \frac{3c_0^3}{8\pi f^3} \tag{5.7}$$

represents the change in size necessary to modify the modal content of the system. Modifying the volume may not always be the best method to modify the excited modes,

$$\Delta f \approx \frac{c_0^3}{8\pi f^2 V} \tag{5.8}$$

represents the frequency deviation required. This could be accomplished by either injection locking a system and modifying the frequency excitation, using a relatively dirty oscillator, such as a magnetron, or a modulated signal which will excite multiple frequencies at once. Table 5.2 shows various modal statistics for a fixed volume of 0.15 m^3 at different frequencies.

While 685 modes supported at 2.45 GHz seems significant, however, many of these modes will excite a similar mode profile. Additionally, not all of these modes can be excited at once. The field pattern excited will depend on how the probe is oriented to the electric or magnetic field inside of the cavity. For rectangular cavities, the location becomes increasingly complex due to the lack of rotational symmetry compared to a cylindrical cavity.

Table 5.2: Mode Variations

Frequency	N_s	ΔV **(m^3)**	Δf **(MHz)**
915 MHz	36	0.02799	8.54
2.45 GHz	685	0.00146	1.19
10 GHz	46635	0.000021	0.071

$$L\Phi = \lambda M\phi \tag{5.9}$$

$$\lambda = \min \frac{\int \Phi \mathrm{L} \Phi \mathrm{dv}}{\int \Phi \mathrm{M} \Phi \mathrm{dv}} \tag{5.10}$$

$$\nabla^2\Phi + k^2\Phi = 0 \tag{5.11}$$

$$k^2 = \min \frac{\int \Phi \nabla^2 \Phi \mathrm{dv}}{\int \Phi^2 \mathrm{dv}} \tag{5.12}$$

$$k^2 = \min \frac{\int_{\mathrm{v}} |\nabla\Phi|^2 \mathrm{dv} - \oint \Phi \frac{\partial\Phi}{\partial \mathrm{n}} \mathrm{dS}}{\int_{\mathrm{v}} \Phi^2 \mathrm{dv}} \tag{5.13}$$

An eigenvalue analysis can give great insight into the resonant modes supported by a microwave structure. Eigenvalue analysis takes an equation of the form in (5.9) and solves for lambda using the variational principle (5.10) where L and M are differential, integral, scalar, or vector operators, Φ is an eigenfunction, and λ is the corresponding eigenvalue. Applying this to the Helmholtz equation (5.11) yields a way to solve for the resonant wave number (5.12). This result can be transformed to (5.13) in order to easily apply different boundary conditions and solve the structure [83].

The result is source independent, depending only on the structure and boundary conditions of the resonant structure. For a typical metallic structure with perfectly conducting walls, the tangential E and normal magnetic field must vanish. Using commercial software, this process generally gives resonant frequencies, and the associated electric and magnetic fields and Q of the system. The electric and magnetic fields can be decomposed in order to determine the best way to excite a given mode. Along the wall of a metallic structure, a magnetic loop or monopole-like structure excites a field that will satisfy the boundary conditions to obtain efficient coupling.

$$\boldsymbol{M}_{nmt} = \nabla \times \boldsymbol{a_z} \psi_{Mnmt} \tag{5.14}$$

$$k_{nmt}\boldsymbol{N}_{nmt} = \nabla \times \nabla \times \boldsymbol{a_z}\psi_{Nnmt} \tag{5.15}$$

$$k_{nmt}\boldsymbol{L}_{nmt} = \nabla\psi_{Lnmt} \tag{5.16}$$

$$\psi_{Mnmt} = \sqrt{\frac{\varepsilon_{0n}\varepsilon_{0t}}{\pi c}}\frac{J_n(p'_{nm}r/a)\,\sin\frac{t\pi z}{c}\,\cot(n\phi)}{\sqrt{1-n^2/p'^2_{nm}}J'_n(p'_{nm})p'_{nm}} \tag{5.17}$$

$$\psi_{Nnmt} = \sqrt{\frac{\varepsilon_{0n}\varepsilon_{0t}}{\pi c}}\frac{J_n(p_{nm}r/a)\,\cos\frac{t\pi z}{c}\,\cot(n\phi)}{J'_n(p_{nm})p_{nm}k_{nmt}} \tag{5.18}$$

$$\psi_{Lnmt} = \sqrt{\frac{\varepsilon_{0n}\varepsilon_{0t}}{\pi c}}\frac{J_n(p_{nm}r/a)\,\sin\frac{t\pi z}{c}\,\cot(n\phi)}{a\,J'_n(p_{nm})} \tag{5.19}$$

$$k_{nmt} = \sqrt{\left(\frac{p_{nm}}{a}\right)^2 + \left(\frac{t\pi}{c}\right)^2} \tag{5.20}$$

$$q_{nmt} = \sqrt{\left(\frac{p'_{nm}}{a}\right)^2 + \left(\frac{t\pi}{c}\right)^2} \tag{5.21}$$

$$\bar{G}_e(r,r') = \sum_{n=0}^{\infty}\sum_{m=0}^{\infty}\sum_{t=0}^{\infty}\left[\frac{\boldsymbol{M}_{nmt}(r)\boldsymbol{M}_{nmt}(r')}{q^2_{nmt}-k_0^2} + \frac{\boldsymbol{N}_{nmt}(r)\boldsymbol{N}_{nmt}(r')}{k^2_{nmt}-k_0^2} - \frac{\boldsymbol{L}_{nmt}(r)\boldsymbol{L}_{nmt}(r')}{k_0^2}\right] \tag{5.22}$$

$$\boldsymbol{E} = -j\omega\mu_0\bar{G}_e(r,r')\cdot\boldsymbol{J}(r') \tag{5.23}$$

Expanding the Green's function with the eigenfunctions can help determine which of these resonant frequencies can be excited. For a cylindrical cavity of radius a and length c, the fields excited in the cavity can be decomposed into the solenoidal fields $\boldsymbol{M_{nmt}}$ (5.14), TE modes, and $\boldsymbol{N_{nmt}}$ (5.15), TM modes, and the irrotational modes $\boldsymbol{L_{nmt}}$, (5.16), where $\boldsymbol{a_z}$ is the unit vector along the length of the cylindrical cavity and ψ (5.17, 5.18, 5.19) are solutions to the Helmholtz equation. The resonant wave numbers, k and q (5.20, 5.21) can be combined with the mode functions to solve the Green's function (5.22) and determine which electric field can be excited with (5.23) [84]. The important consequence of the Green's function is that any resonant mode can be excited with diminished magnitude for an excitation frequency away from the resonant frequency.

Analytically, the eigenfunctions are difficult to solve for electrically large cavities due to the sheer number of modes supported. The combination of full-wave eigenmode simulation results and the core theory behind the Green's function aids the design of excitations.

5.4 Electrically Large Cylindrical Cavity

5.4.1 915 MHz Analysis

The first logical frequency to model the cavity at is 915 MHz. Excitations are readily available due to commercial cooking and solid state transistors meant for UHF/L-Band radar applications. From the previous analysis, only about 36 modes are supported. However, as soon as a material is added into the cavity, this number can drastically increase, scaling with $\sqrt{\varepsilon_r}$. For low permittivity materials, such as wood and oil, the number of supported modes can increase to 80. For high permittivity materials, such as water, this number can increase to 324, however, the loss will also typically be increased as well so the number of actual excited modes will decrease substantially. Eigenmode analysis can give a general idea of what to expect out of electrically hard cavities, however, even with this number of modes the data can be overwhelming. Each component of the electric and magnetic field must be considered to determine which modes can be excited using realistic coupling methods, which will be explored further in section 5.5. The design of a probe at this frequency is what makes it more interesting than higher frequencies. The electrical size necessary complicates the issue because E-probes and loops cannot be arbitrarily placed due to material completely filling the cavity.

Consider the following example of a cavity loaded with ε_r=3 and $tan\delta$=0.03. The cavity is 14 in (35.56 cm) in diameter and 60 in (1.524 m) long, creating an electrically large cylindrical cavity as shown in Fig. 5.3. The initial plan was to use a 0.1 m^3 cavity as this size would be appropriate for creating an electrically large cavity at low frequencies without requiring an excessive amount of power. However, to reduce cost, the design is driven by affordable and readily available components, leaving ventilation ducts as the most reasonable choice.

The cavity has resonances at very specific frequencies, as determined using the eigenmode analysis in HFSS. The error of this specific frequency can be decreased at the cost of computational resources, however, even 5-10 % is accurate enough for this application. The fundamental resonant

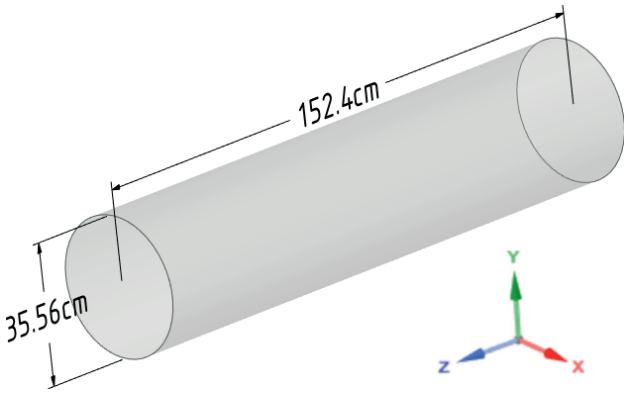

Figure 5.3: Dimensions of the cylindrical cavity.

(TE_{111}) frequency can be calculated using,

$$f_0 = \frac{c\sqrt{1+\left(\frac{2l}{3.41a}\right)^2}}{2l\sqrt{\mu_r\varepsilon_r}} \tag{5.24}$$

where c is the speed of light, l is the length of the cavity, and a is the radius of the cavity. The TE_{111} cut-off frequency is found to be 154 MHz, indicating that the cavity will be operated far from the fundamental resonant mode.

For the following eigenmode solutions, the scale is not very important as the result is normalized to a peak electric field of 1 V/m. The benefit of the eigenmode solver is to see structure and components of fields that can be excited using realistic methods. It is also important to note that the orientation of the field is irrelevant as the circular symmetry of the cylindrical cavity will allow the mode to be excited at any orientation. For all plots, the complex magnitude of the electric field, or the steady state field independent of phase, is shown. The closest frequency to the 915 MHz excitation frequency is Fig. 5.4, 914.8 MHz, showing complex magnitude of the electric field along the central XZ, YZ, and XY plane cuts. This mode is characterized by a strong normal electric field along the boundary, and little field distribution elsewhere.

The next interesting mode is at 916.2 MHz, Fig. 5.5, showing a much simpler electric field result. This mode would not be necessarily ideal due to a lack of field in the central portion of the cavity.

The next resonant mode is at 916.9 MHz, Fig. 5.6. This mode pattern contains more field

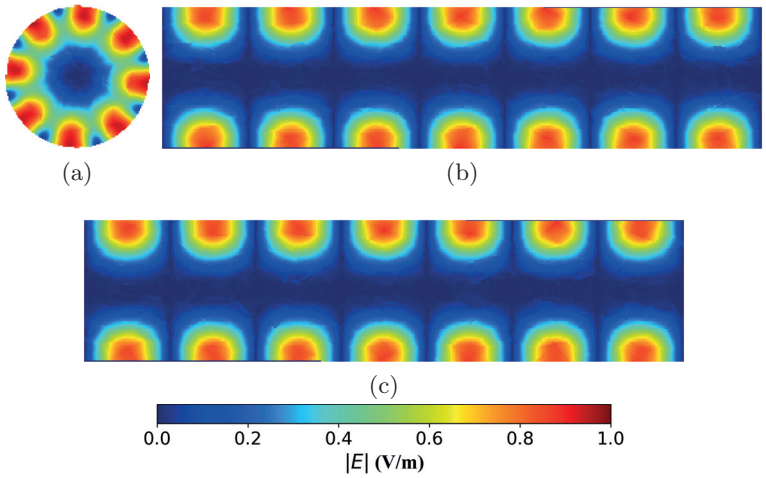

Figure 5.4: Complex magnitude of the electric field for the resonant mode at 915 MHz showing the (a) XY-plane cut, (b) XZ-plane cut, and (c) YZ-plane cut.

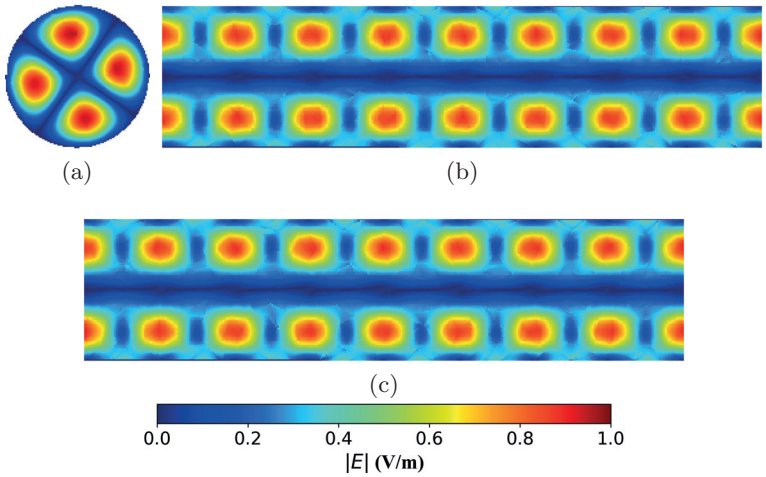

Figure 5.5: Complex magnitude of the electric field for the resonant mode at 916 MHz showing the (a) XY-plane cut, (b) XZ-plane cut, and (c) YZ-plane cut.

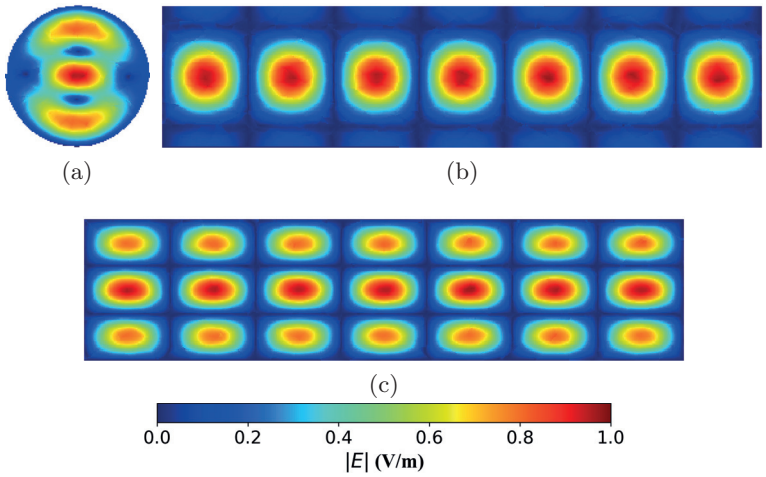

Figure 5.6: Complex magnitude of the electric field for the resonant mode at 917 MHz showing the (a) XY-plane cut, (b) XZ-plane cut, and (c) YZ-plane cut.

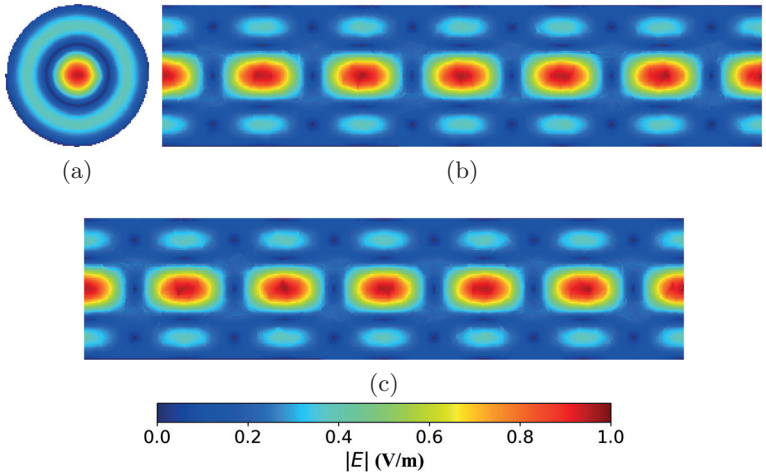

Figure 5.7: Complex magnitude of the electric field for the resonant mode at 921 MHz showing the (a) XY-plane cut, (b) XZ-plane cut, and (c) YZ-plane cut.

content in the center of the cylindrical cavity, however, rotationally it is lacking.

The last mode close to the operational frequency, Fig. 5.7, is at 920.7 MHz. This resonant frequency contains a rotationally symmetric field with a high field magnitude in the center of the cavity.

Overall, the combinations of these four resonant modes contain field content that would create either a relatively homogeneous result, or allow for targeting of specific regions of the cavity. This, however, is the simplest approach for a homogeneous loading and would not be the case in a realistic

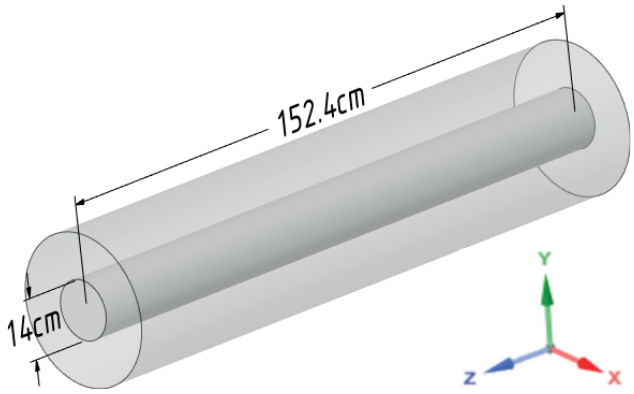

Figure 5.8: Dimensions of the coaxial cavity.

application. The field content will not be nearly as symmetric in practice. This result though, gives an idea of how the cavity will perform under general loading.

An interesting extension to this result is that of a low-Q source. Very few oscillators will have a high-Q frequency response at the given frequency of choice, resulting in some bandwidth around a center frequency. This allows for more interesting results of a given excitation. Or another choice would be using a lower power, clean oscillator to injection lock the source to a desired frequency, and dither the frequency slightly to manipulate the modal content of the cavity.

5.4.2 Coaxial Cylindrical Cavity

A practical consideration for this system will be the mixing and overall processing of materials. A tapered approach may be of interest as materials heat and the overall volume of a given sample size decreases, along with relative permittivity and loss tangent. Assuming constant operation, the end product will need to be somehow extracted from the cavity without effecting the electrical performance of the cavity.

To begin the formation of this cavity, a center PEC cylinder creates a coaxial cavity, similar to one shown in Fig. 5.8. Placing a center conductor will decrease the overall field-of-view for an individual source. This will enable more control over the generation of a given field profile in the cavity. An eigenmode analysis is performed around 915 MHz to observe the effect of the diameter of an inner conductor on the field profile. For a 6 cm diameter, Fig. 5.9, and 10 cm diameter,

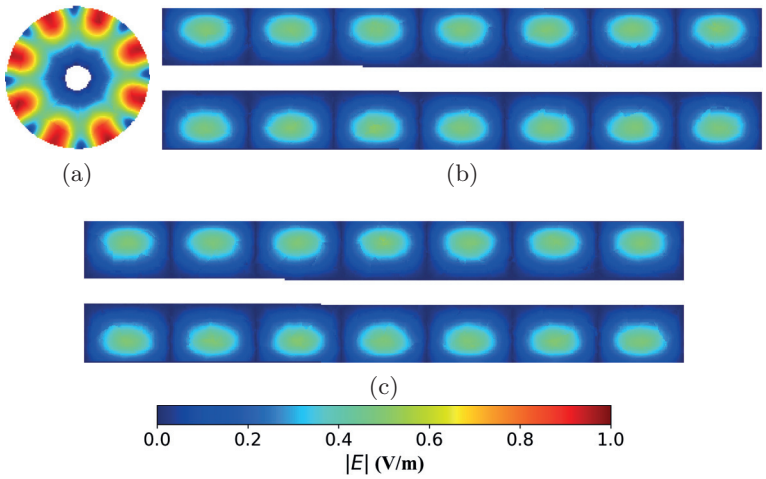

Figure 5.9: Complex magnitude of the electric field for the resonant mode at 914.7 MHz with a 6 cm diameter PEC cylinder showing the (a) XY-plane cut, (b) XZ-plane cut, and (c) YZ-plane cut.

Fig. 5.10, the resonant frequency closest to 915 MHz has a similar field profile as when there is no central cylinder. This is due to the lack of field at this point in previous results. As the diameter increases to 14 cm, the field profile begins to change, and becomes closer to the 917 MHz resonant probe of the previous section. The addition of a 14 cm center conductor reduces the overall volume from 0.15 m^2 to 0.05 m^3, reducing the amount of material to heat. Conversely, this now adds a central heatsink in the cavity which can pose an issue with the heat dissipating too fast through the cylinder.

5.5 Driven Excitation of a Electrically Large Cavity

5.5.1 Cavity Setup

For electrically large cavities, waveguide adapters interfacing with magnetrons are popular, such as with the commercial tabletop microwave oven. With the electrical size decreasing, microstrip patch probes become more realistic to implement as they can be made electrically small, however, loss becomes a large concern at high powers when using a lossy dielectric. With resonant cavities and waveguide excitations, apertures, monopole, and loop probes are popular due to their electrically

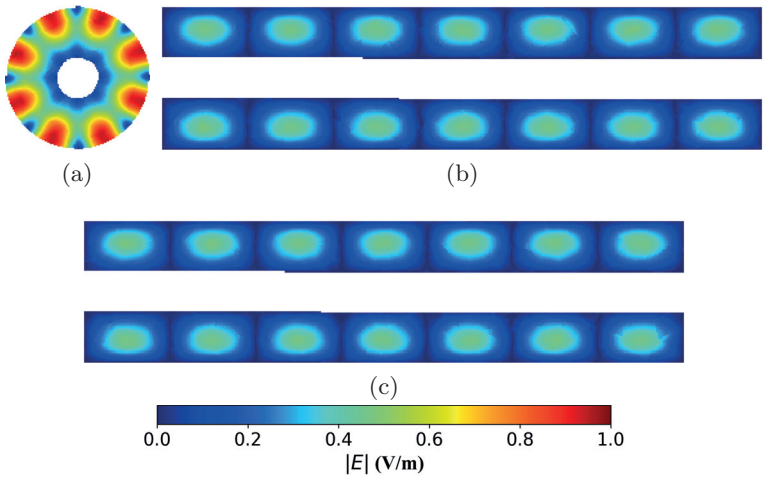

Figure 5.10: Complex magnitude of the electric field for the resonant mode at 914.4 MHz with a 10 cm diameter PEC cylinder showing the (a) XY-plane cut, (b) XZ-plane cut, and (c) YZ-plane cut.

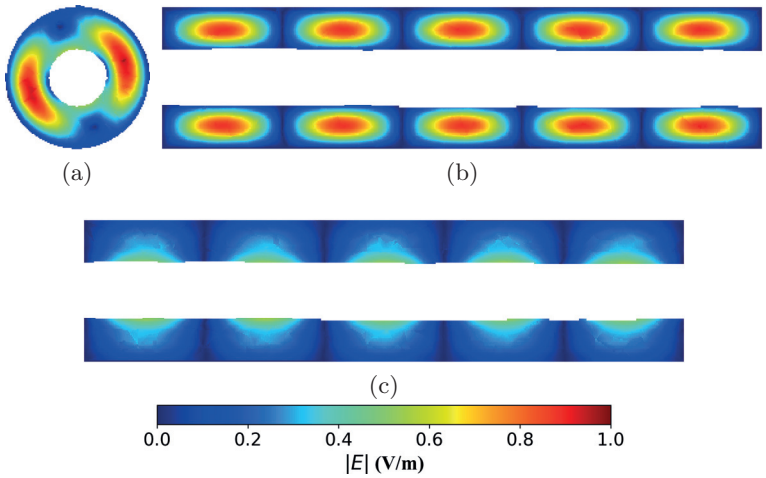

Figure 5.11: Complex magnitude of the electric field for the resonant mode at 914.6 MHz with a 14 cm diameter PEC cylinder showing the (a) XY-plane cut, (b) XZ-plane cut, and (c) YZ-plane cut.

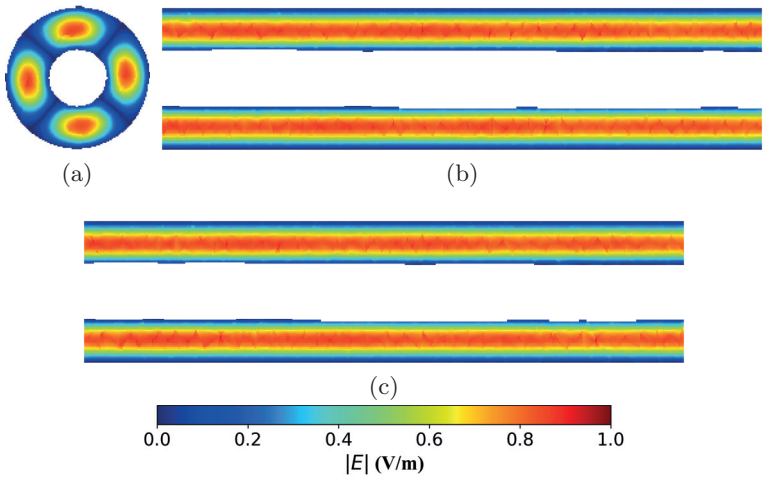

Figure 5.12: Complex magnitude of the electric field for the resonant mode at 917.5 MHz with a 14 cm diameter PEC cylinder showing the (a) XY-plane cut, (b) XZ-plane cut, and (c) YZ-plane cut.

small size compared to half a wavelength. Placement and probe type is critical to the given application and field pattern desired and requires careful consideration based on the size desired and power necessary. For a large microwave oven with a near 100% fill factor and moving materials, monopoles and loops in the cavity cannot be used as they protrude into the cavity and could break. This work will focus on using patch probe excitations at lower frequencies (around 915 MHz) and waveguide excitations at higher frequencies (2.45 GHz).

Another consideration to make with the placement is the relative phasing between each excitation. As with the MRI work, the complex addition between each excitation becomes critical. However, by working from the ground up and having more access to the RF control, more parameters and methods can be employed to improve the field distribution. One such method, popularized by MRI, is the time interleaved acquisition of modes [85]. This method builds on the fact that 100% duty cycle for one excitation scheme is not necessary, and using two or three schemes can improve homogeneity inside of a target volume. This method can be extended to microwave heating as thermal time constants are significantly longer than the period of the RF excitation and will negate some of the issues due to complex addition with multiple excitations.

For convenience, a double-ridged waveguide can be used as an excitation to lower the overall cut-

off frequency of a given outer dimensions for a waveguide. Dimensions of a doubled ridged waveguide can be chosen to operate over a large frequency bandwidth, generally about 2.4:1 and 3.6:1. This is accomplished through the use of two ridges placed in the center of the waveguide where the electric field is at its maximum. These ridges add capacitive loading to the center of the waveguide to not only lower the cut-off frequency, but also reduce the input impedance. Unfortunately, one draw-back to the double ridged waveguide is increased attenuation due to a larger surface area to carry currents. The mil-standard WRD-970U36 double ridged waveguide with a nominal frequency range of .970-3.5 GHz will suit this application well. The nominal frequency is slightly higher than the desired frequency of 915 MHz, however, the cut-off is low enough, 822 MHz, that it should still work adequately. This waveguide is characterized by a 98.48 mm length, 42.34 mm height, 8.255 mm gap, and 24.613 ridge width. This is slightly larger than the standard S-band waveguide 72.14 mm width, but significantly smaller than the 247.65 mm waveguide that operates at 915 MHz. The analysis at 2.45 GHz will use this excitation entirely as the eigenmode analysis is too computationally intensive. The double-ridged waveguide will be driven with a wave-port to observe the effect of a driven excitation without having to be concerned with designing a transition for the application. The setup with two orientations of waveguides is shown in Fig. 5.13. The two orientations are denoted a_z, Fig. 5.13b, and a_y, Fig. 5.13c. This convention is chosen due to the orientation, a_z, will predominantly excite $\mathbf{H}_z$ inside of the cavity and $a_y$will predominantly excite the $\mathbf{H}_y$ of the cavity in this location. All plots will be normalized to 1 W total excitation power for a fair comparison between single and multiple feed results and continue to show the complex magnitude of the electric field, as this will directly translate to heating of the material. The field plots will be formatted as a center cut of the XZ-plane, YZ-plane, then XY-plane for the a_z (a-c) excitation and a_y (d-f) excitation.

5.5.2 Low Loss Material

The first and most interesting excitation to consider will be the one of the low-loss material, with the same material properties as the previous section (ε_r=3, tanδ=0.03). With a 915 MHz excitation

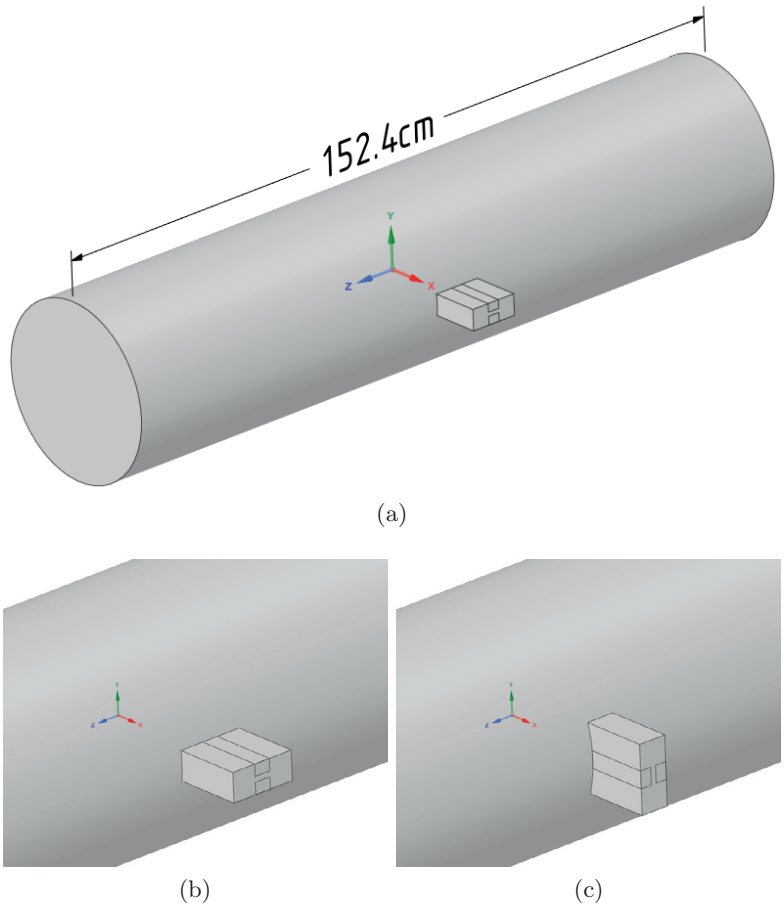

(a)

(b) (c)

Figure 5.13: (a) Setup of an electrically large cylindrical cavity with (b) a_z and (c) a_y excitation.

in the cylindrical cavity, Fig. 5.14, the majority of the electric field dissipates significantly with even this low of a loss tangent. With 1 W input power, the center and peaks of the mode features are slightly lower than 100 V/m. The overall modal feature of the $a_z$orientation can be seen as a combination of the 915 MHz eigenmode, Fig. 5.4, and the 917 MHz, Fig. 5.6, eigenmode. On the other hand, the a_y orientation is primarily composed of the 917 MHz eigenmode, highlighted by 3 main strips across the XY-plane cut. Interestingly, the rest of the cavity does not behave similar to the 917 MHz resonant mode, highlighting an issue predicting the field as the medium becomes inhomogeneous. The presence of the feed can slightly shift the E field towards the feed, but in this case it is not significant due to the small size of the waveguide. This result has two important conclusions. The first is that this frequency and loss are both low enough that the cavity still behaves as a resonant cavity. Modes are formed and established across the entire domain. Second,

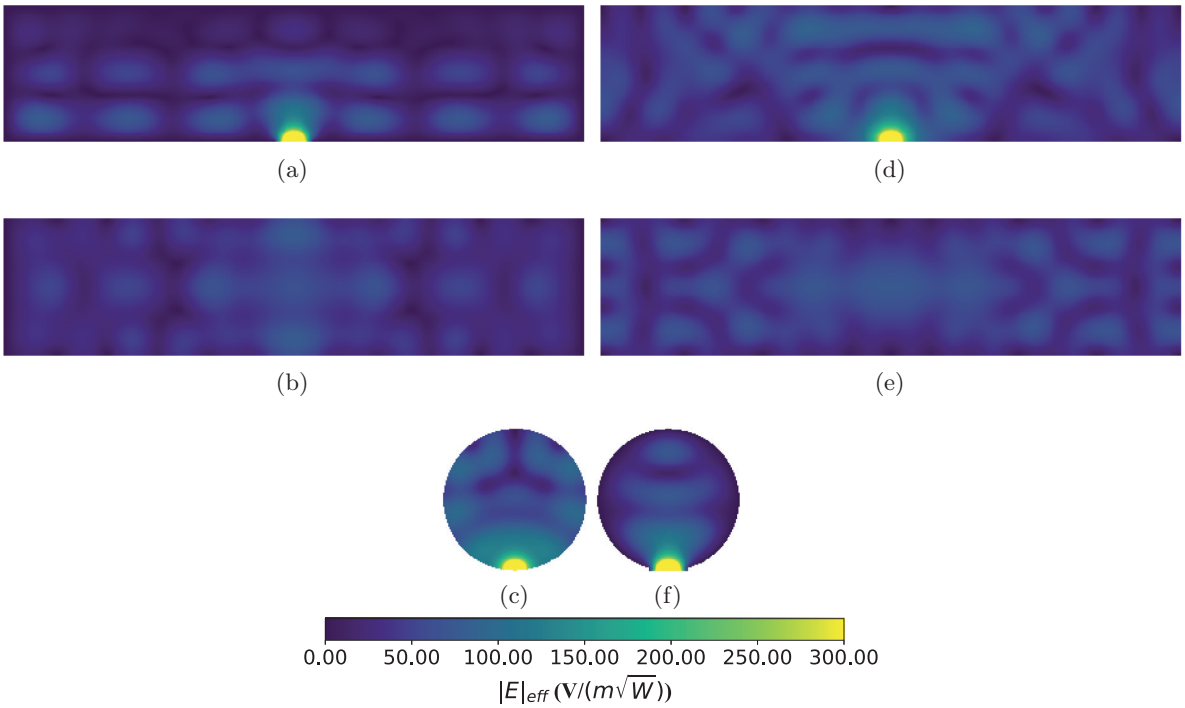

Figure 5.14: 915 MHz double ridge waveguide excitation in the cylindrical cavity: (a) XZ, (b) YZ, and (c) XY plane cuts for the a_z orientation and (d) XZ, (e) YZ, and (f) XY plane cuts for the a_y orientation.

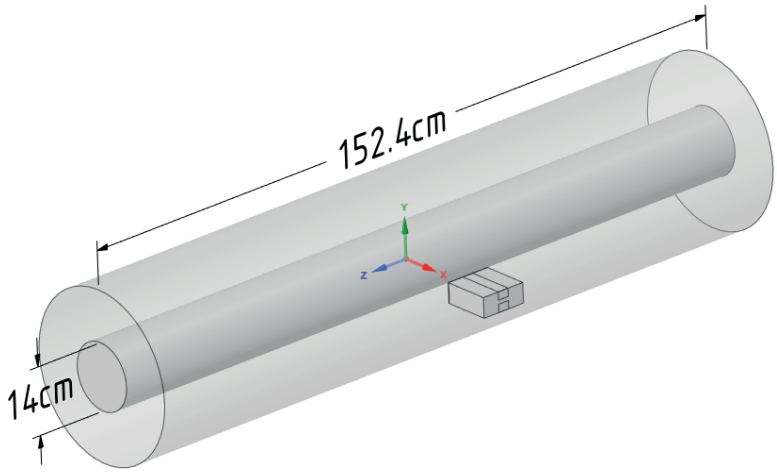

Figure 5.15: Setup of the cylindrical cavity with the addition of a PEC central cylinder to create a coaxial cavity.

the result is symmetric across the X-axis, but not rotationally symmetric. This would enable a second feed to be placed directly opposite of the first with minimal coupling.

With the addition of a 14 cm (5.51 in) diameter cylinder placed in the middle of the cavity,

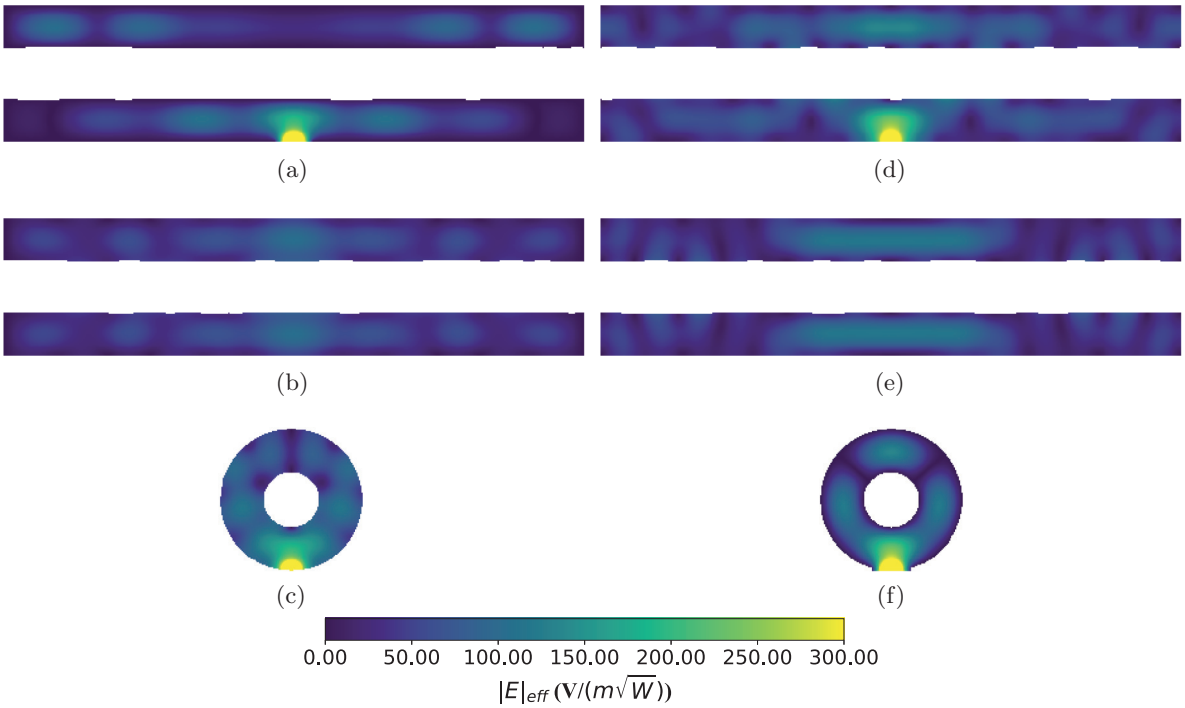

Figure 5.16: 915 MHz double ridge waveguide excitation in the coaxial cavity: (a) XZ, (b) YZ, and (c) XY plane cuts for the a_z orientation and (d) XZ, (e) YZ, and (f) XY plane cuts for the a_y orientation.

thus creating a coaxial cavity, really does not significantly effect the field profile at 915 MHz. The center of the plot shows the region occupied by the center cylinder with bumps in the field due to discretization issues with the field export functionality in HFSS. The result for a_z, Fig. 5.16, is nearly identical to the previous result, minus the center modal feature. For the other orientation, a_y, Fig. 5.16(d-f), the field pattern changes to be almost completely composed of Fig. 5.12. This field is characterized by a relatively homogeneous electric field around the excitation.

To compare the two orientations, two cases are evaluated. The first is a line from the center of the feed to directly across the cavity on the X-axis as shown in Fig. 5.17. Both orientations have very similar field magnitudes in the cylindrical cavity. However, by adding the center conductor and creating a coaxial cavity, the a_y orientation has a 20% increase in field magnitude on the near end and an increase of almost 200% on the far end. This could be considered both a positive and negative, as now the field is higher, but the coupling to a feed on the opposite side may be higher.

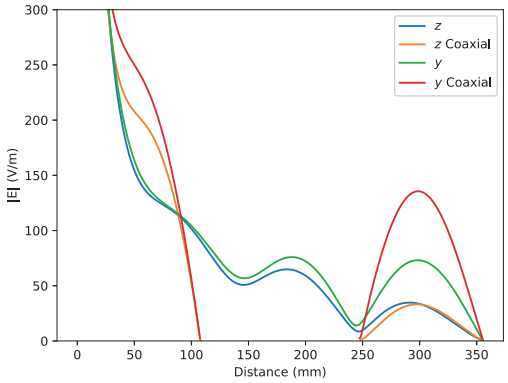

Figure 5.17: Complex magnitude of the electric field in the cylindrical and coaxial cavity at 915 MHz.

Setup	$\lvert\mathbf{E}\rvert \frac{V}{m\sqrt{W}}$
a_z Cyl. Cavity	61.15
a_z Coax. Cavity	74.72
a_y Cyl. Cavity	49.07
a_y Coax. Cavity	72.06

Table 5.3: 915 MHz average complex magnitude of the electric field inside of a 8 in long cylinder centered around the feed.

An average of the electric field spanning an 8 in disk, centered around the feed, is shown in Table 5.3. Interestingly, this result is exact opposite to the conclusion from Fig. 5.17. The a_y orientation results in a lower average electric field magnitude due to inhomogeneity in the result, as shown by the lack of electric field around the cavity wall. As a single feed, this can be seen as a drawback. However, as a system, this can be beneficial to reduce coupling between feeds.

A large issue with this system will be the inhomogeneity of the cooking material and excited electric field. In order to alleviate some of the concerns, a large rotating spiral, or auger, is placed on the central conductor of the coaxial cavity. The auger has a blade separation of 25 cm (9.8 in) and a thickness of 5.1 mm (0.2 in) as shown in Fig. 5.18. The blade extends from the center conductor all the way to the edge of the cavity. The thickness should provide enough mechanical stability to adequate rotate the material and push it along the cavity. A benefit of this action will segment the cavity into individual sections, allowing for a tapering or changing of frequency depending on

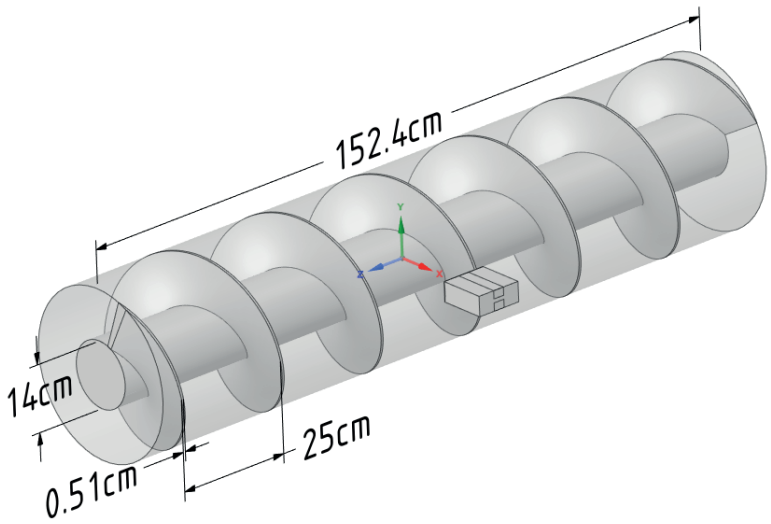

Figure 5.18: Dimensions of the auger placed inside of the existing coaxial cavity.

the material in the individual feed field of view. With the addition of the metal auger, this is no longer a coaxial cavity. The metal compartmentalizes the excitation and would allow for the infinite expansion in either direction along the Z-axis with minimal impact to a given excitation. This can be highly beneficial to the analysis of a scaling cavity to reduce computational resources.

Fig. 5.19(a-f) shows a 60° incremental rotation using a metal material for the blade for a_z orientation with the XZ-plane cut on the left and XY-plane cut on the right. This segments the cavity fairly well, allowing for an increased field magnitude near the feed. Unfortunately, at certain rotation angles, the metal blade will short the two ridges of the feed together and result in a high reflection toward the transmitter. While not ideal, this issue can be fixed simply by turning off the transmitter in this orientation. If the material of the auger blade is changed from metal to a ceramic (ε=12), Fig. 5.19(g-l), the overall field profile does not significantly change from the case without the auger. This would allow for material mixing with little to no effect on the field in the cavity.

Changing the orientation to a_y, a similar effect occurs as the previous orientation. Fig. 5.20(a-f) shows a homogeneity improvement circularly around the XY-plane cut without a high peak on the opposite side of the feed. Because the blade is no longer in the same plane as the ridges on

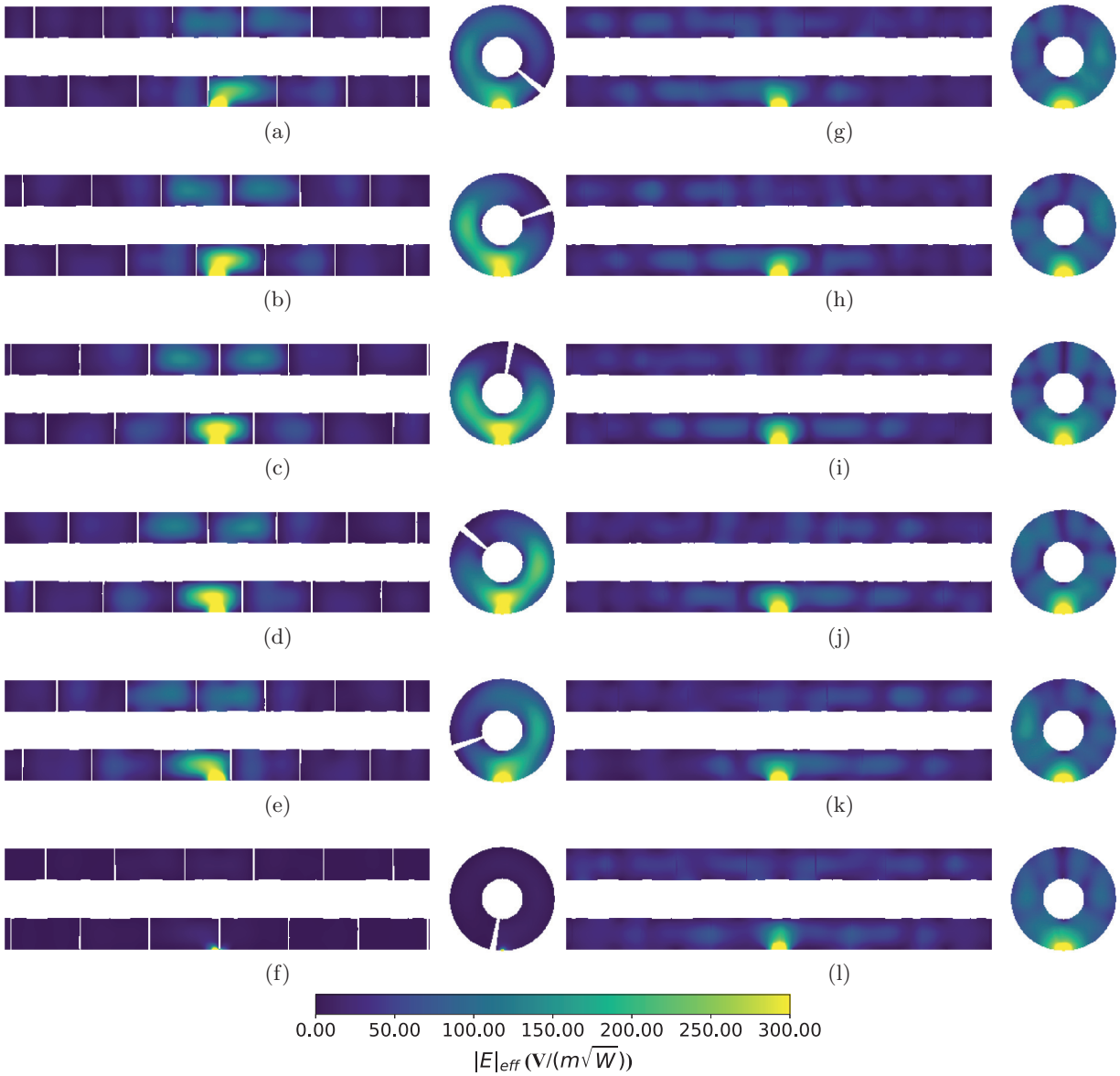

Figure 5.19: 915 MHz a_z oriented excitation with the rotating auger in 60° increments: XZ cut (left) and XY cut (right) (a-f) metal auger and (g-l) ceramic auger.

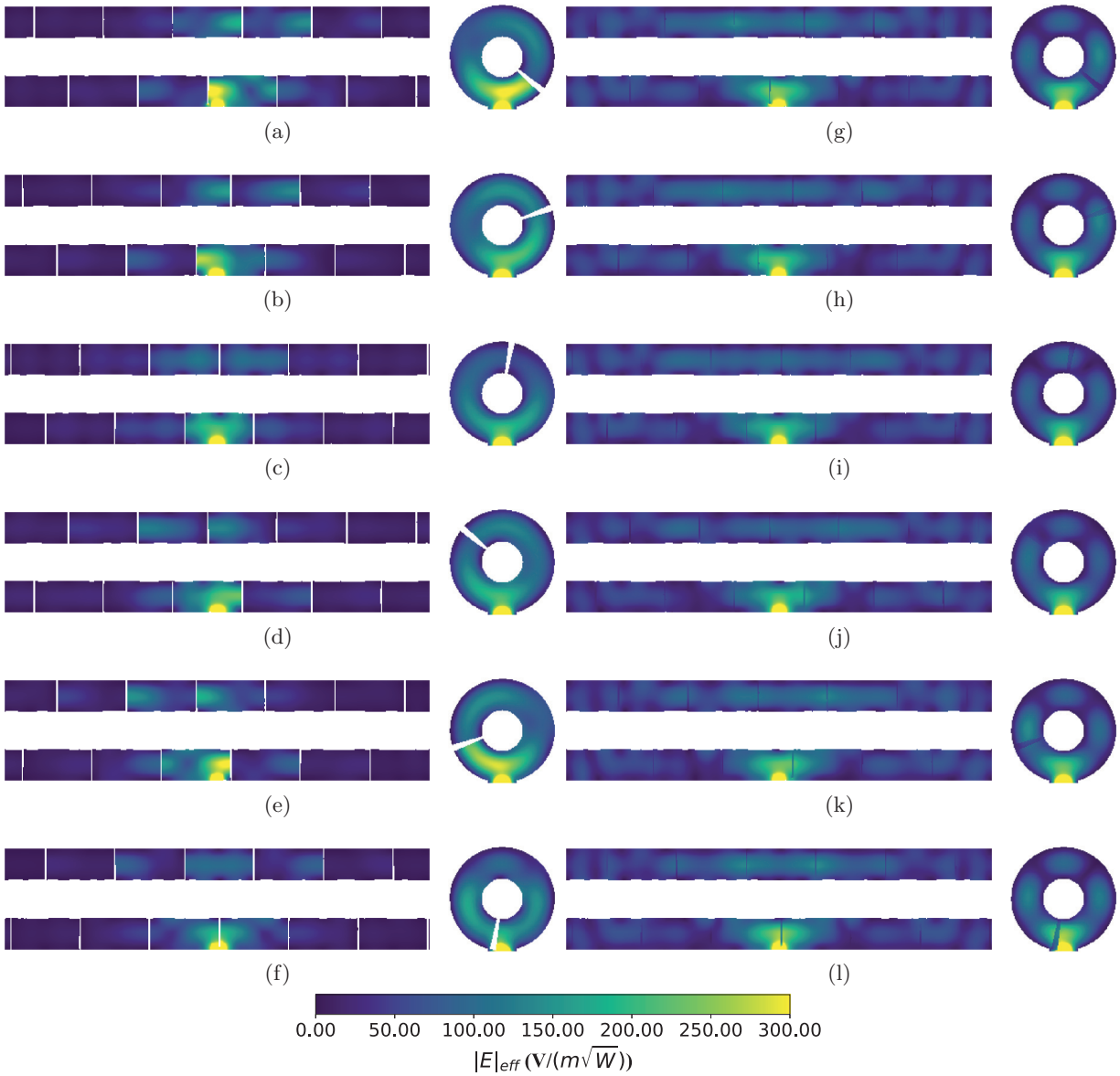

Figure 5.20: 915 MHz a_y oriented excitation with the rotating auger in 60° increments: XZ cut (left) and XY cut (right) (a-f) metal auger and (g-l) ceramic auger.

Rotation	a_z Metal $\lvert\mathbf{E}\rvert \frac{V}{m\sqrt{W}}$	a_y Metal $\lvert\mathbf{E}\rvert \frac{V}{m\sqrt{W}}$	a_z Ceramic $\lvert\mathbf{E}\rvert \frac{V}{m\sqrt{W}}$	a_y Ceramic $\lvert\mathbf{E}\rvert \frac{V}{m\sqrt{W}}$
0°	79.47	96.34	78.84	74.24
60°	92.49	92.98	71.85	69.82
120°	98.83	89.88	71.35	65.09
180°	96.16	90.38	73.27	65.12
240°	84.86	96.88	76.05	72.29
300°	7.73	88.07	75.20	77.08

Table 5.4: 915 MHz average complex magnitude of the electric field inside of a 8 in long cylinder centered around the feed as the auger rotates.

the horn, the issue of shorting the feed is not a concern. Similarly as in the previous orientation, the field profile does not significantly change with the addition of a ceramic blade Fig. 5.20(g-l). A quantitative comparison of the results can be seen in Table 5.4 at 915 MHz for the 60° incrementations of the auger for all of the variations. By reorienting the feed in the metal auger setup, the peak average decreases slightly, but the overall average is increased due to the fact that the metal auger can no longer short the feed. With the ceramic blade, however, the average across the rotation of the auger is consistently higher with the a_z orientation. With the ceramic blade, both orientations hardly see an increase in the average electric field at all compared to the case with the coaxial cavity. This is not surprising as the field profile does not significantly change with the presence of the ceramic material.

Increasing the frequency to 2.45 GHz will significantly increase the complexity of excitation inside of the volume. Because of the number of tetrahedrals necessary to properly model a cavity this large, it cannot be currently easily run using an eigenmode solver. However, as Fig. 5.21 shows, the eigenmode solver is unnecessary. The result is very close to a spherical wave emanating from a point source. The reflections off the cavity walls do begin to complicate the result as the material is not lossy enough to significantly attenuate and reduce the interference in the XY-plane. The field quickly dissipates away from the feed due to the short wavelength and loss of the material. This both requires extra feeds for adequate heating and also reduces the coupling between them. A feed right next to the single feed along the Z-axis will have minimal coupling from its neighbor. A feed rotated around the Z-axis, on the other hand, could possibly see a large amount of coupling

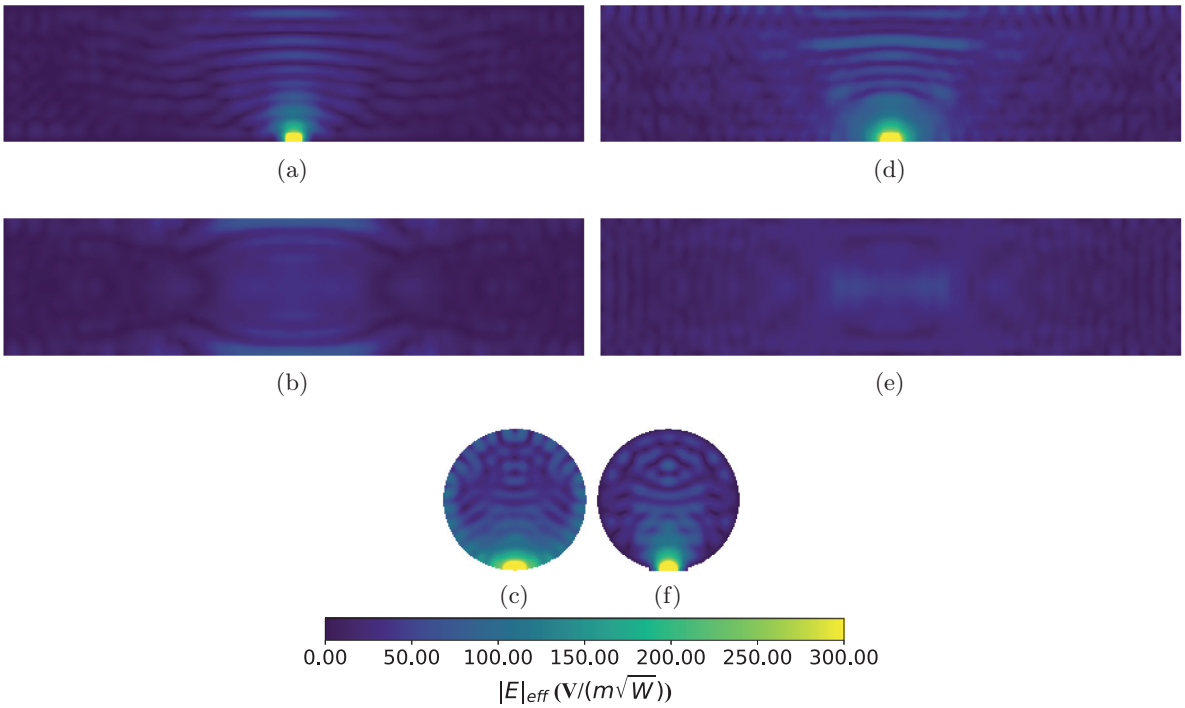

Figure 5.21: 2.45 GHz double ridge waveguide excitation in the cylindrical cavity: (a) XZ, (b) YZ, and (c) XY plane cuts for the a_z orientation and (d) XZ, (e) YZ, and (f) XY plane cuts for the a_y orientation.

due to a high field presence.

The addition of the cylinder in the center of the cavity has a drastic, yet beneficial effect on the field result, Fig. 5.22. With a properly sized central cylinder, the field can reflect back in-phase, resulting in a higher field strength compared to the previous result. Rotationally, the pattern is very similar and coupling will need to be investigated for adding multiple feeds. Translationally along the Z-axis, however, there is again very little field, leaving a possibility for multiple excitations with minimal coupling.

A similar analysis is performed to understand how the cylinder affects the field profile. Fig. 5.23 shows the field near the feed has a slightly higher average due to the peak being higher, but the null is slightly lower. On the far end, the field has reduced to about 50% of the value without the center conductor. Interestingly, the average electric field, Table 5.5 has only increased by about 10%, highlighting an increase in inhomogeneity compared to the case without the central conductor.

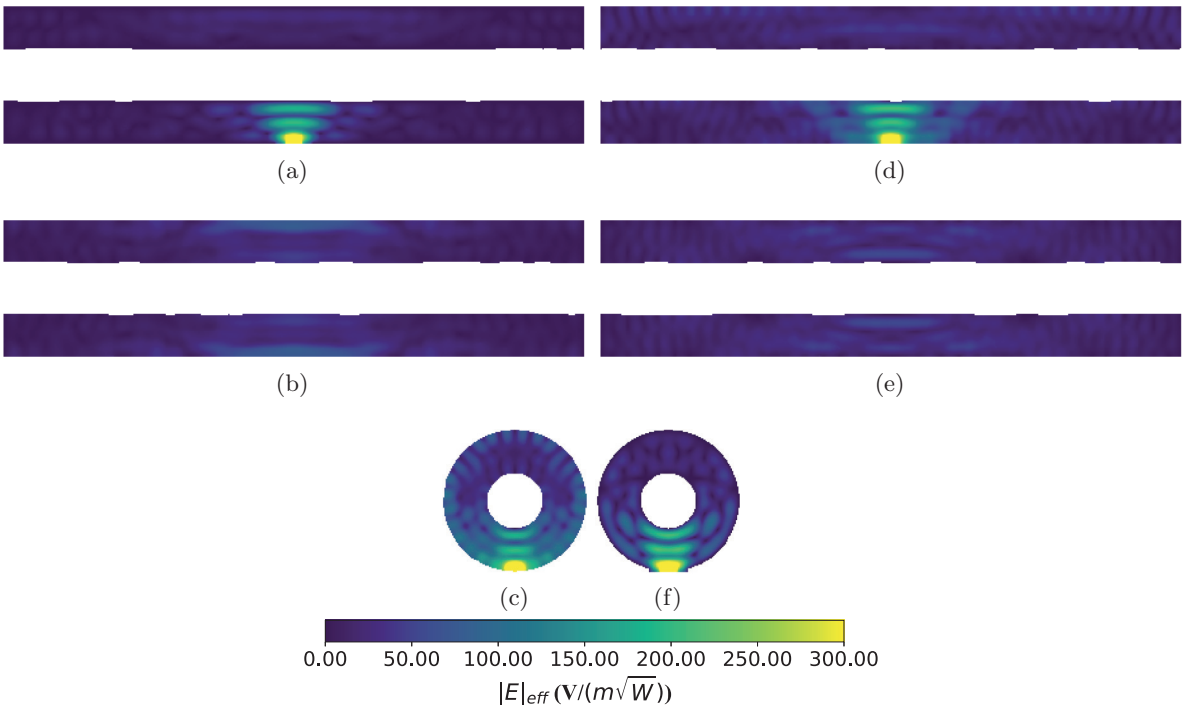

Figure 5.22: 2.45 GHz double ridge waveguide excitation in the coaxial cavity: (a) XZ, (b) YZ, and (c) XY plane cuts for the a_z orientation and (d) XZ, (e) YZ, and (f) XY plane cuts for the a_y orientation.

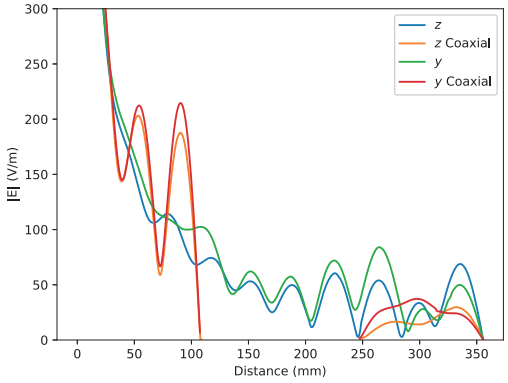

Figure 5.23: Complex magnitude of the electric field in the cylindrical and coaxial cavity at 2.45 GHz.

Setup	$\lvert\mathbf{E}\rvert \frac{V}{m\sqrt{W}}$
a_z Cyl. Cavity	52.35
a_z Coax. Cavity	58.06
a_y Cyl. Cavity	43.11
a_y Coax. Cavity	48.06

Table 5.5: 2.45 GHz average complex magnitude of the electric field inside of a 8 in long cylinder centered around the feed.

With the addition of a metal auger, Fig. 5.24(a-f), $a_z$shows a large restriction to the field to between the metal blade. Similar to the metal auger at 915 MHz, the field tends away from the close metal blade, directing the electric field either left or to the right. Due to the electric field oriented tangential to the metal blade, the electric field must be 0 anywhere near the blade. At this frequency, however, the metal blade does not completely short out the waveguide feed when it overlaps. The ceramic fin, Fig. 5.24(g-l) is the much more interesting result at this frequency. Due to the thickness and high permittivity, the effect of the ceramic blade is very similar to the metal blade. This conclusion combined with the result at 915 MHz shows mode stirring at the challenging higher frequency, while having minimal effect on the more homogeneous lower frequency.

The effect of the metal auger on a_y orientation has an even greater effect on the field profile. Fig. 5.25(a-f) shows the electric field is trapped even more by the rotating auger. With the electric field now being directed normal to the metal blade, it can exist very close to the metal blade. The metal blade pushes it along across the feed up until the metal blade is in the center of the feed, where it is split on either side of the metal fin. On the other hand, the ceramic blade has very little effect on the electric field in the cavity.

The quantitative effects, Table 5.6, on the average electric field at 2.45 GHz are much less pronounced than at 915 MHz. This is due to the fact that pitch of the auger is electrically much larger with the increase in the frequency. Between the two orientations with the metal auger, the average field does not increase substantially. However, between the case with just the coaxial cavity, the a_y metal auger has a large increase in the average electric field. The ceramic blade again only increases the average electric field minimally and would serve mainly to mix the material and push

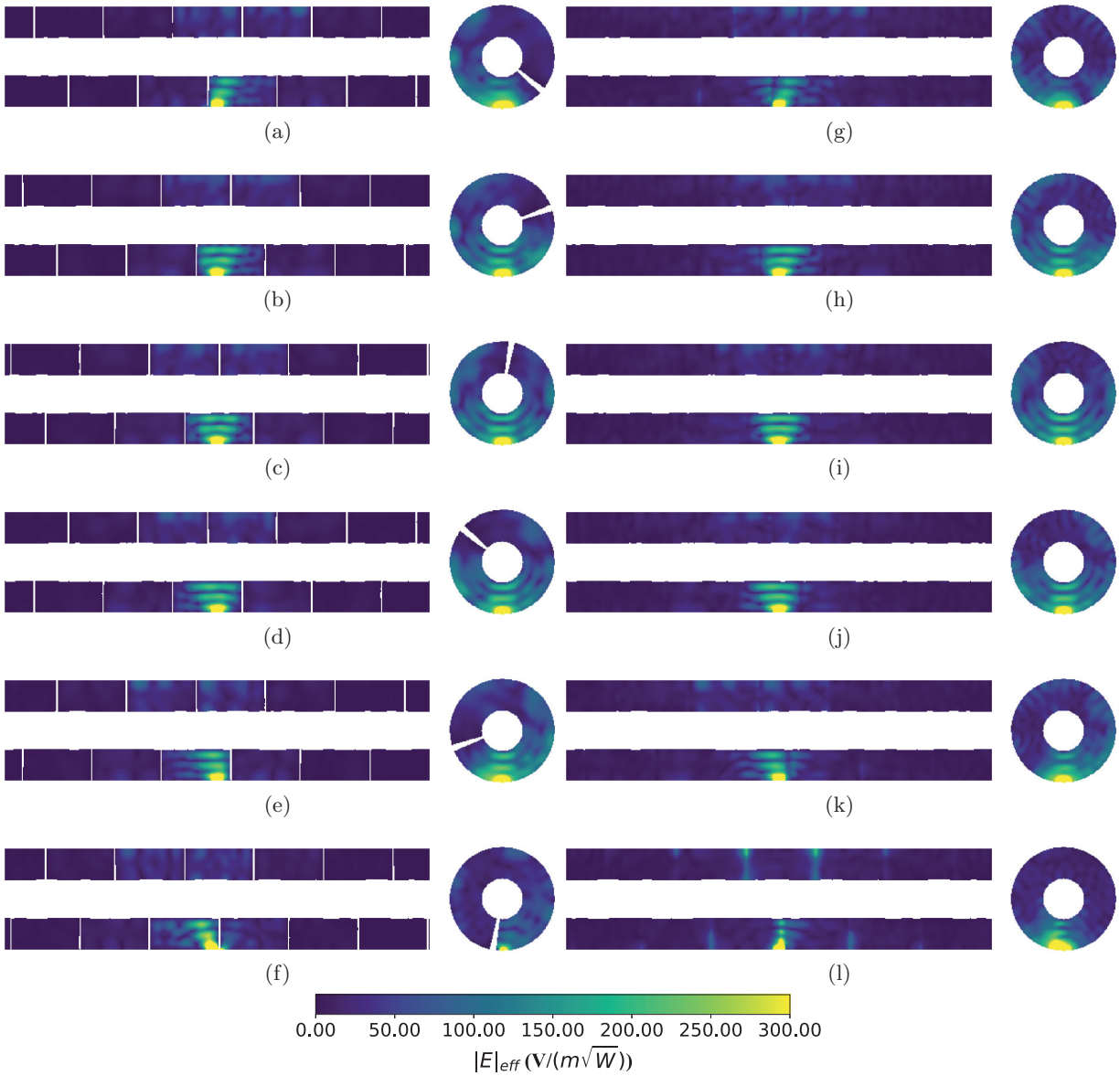

Figure 5.24: 2.45 GHz a_z oriented excitation with the rotating auger in 60° increments: XZ cut (left) and XY cut (right) (a-f) metal auger and (g-l) ceramic auger.

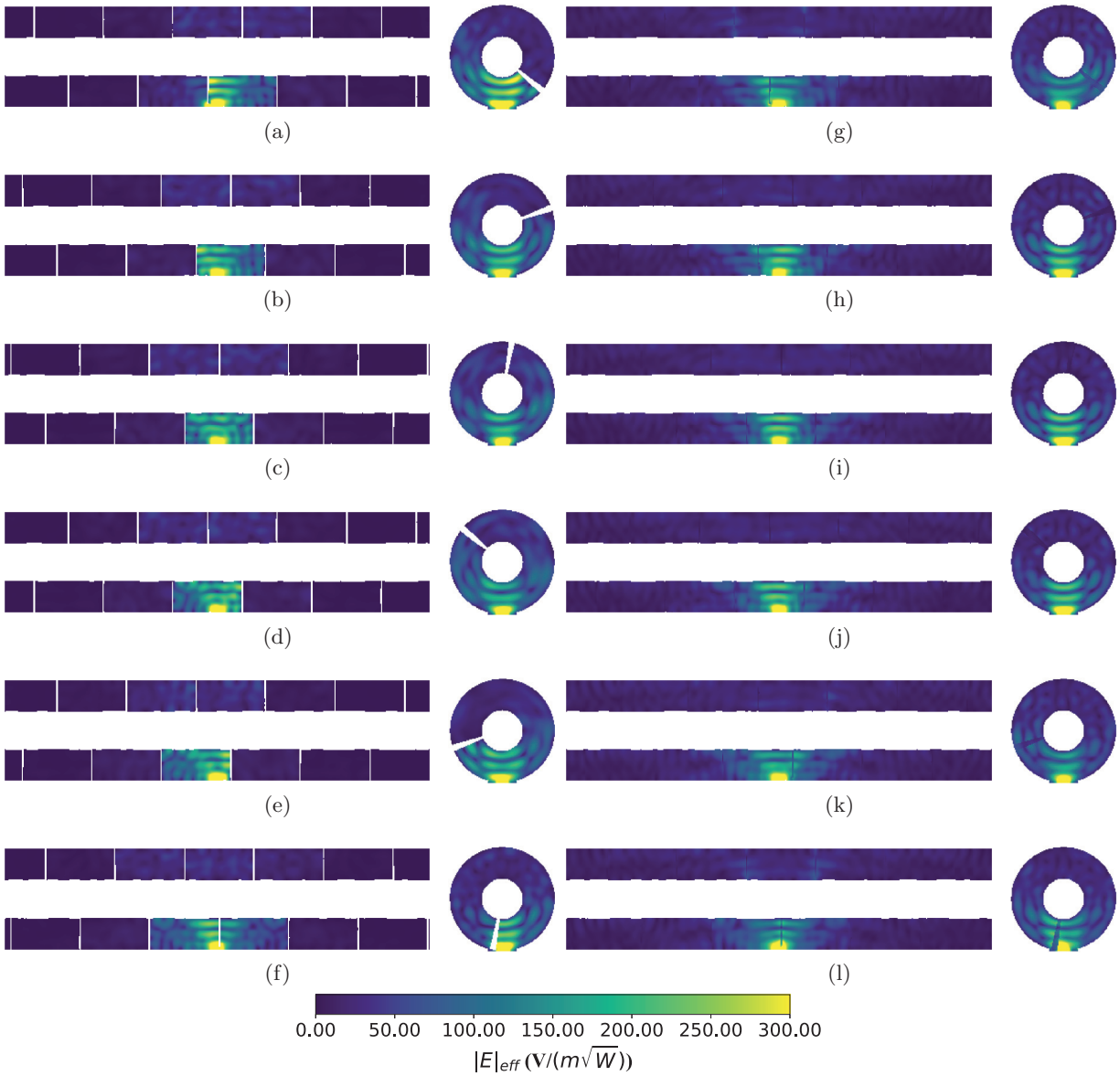

Figure 5.25: 2.45 GHz a_y oriented excitation with the rotating auger in 60° increments: XZ cut (left) and XY cut (right) (a-f) metal auger and (g-l) ceramic auger.

Rotation	a_z Metal $\lvert\mathbf{E}\rvert \frac{V}{m\sqrt{W}}$	a_y Metal $\lvert\mathbf{E}\rvert \frac{V}{m\sqrt{W}}$	a_z Ceramic $\lvert\mathbf{E}\rvert \frac{V}{m\sqrt{W}}$	a_y Ceramic $\lvert\mathbf{E}\rvert \frac{V}{m\sqrt{W}}$
0°	51.91	57.75	52.04	51.19
60°	61.62	59.29	59.40	50.86
120°	61.73	63.50	59.04	51.16
180°	63.62	62.56	60.98	51.23
240°	57.92	58.69	55.85	50.28
300°	48.42	55.89	48.38	54.72

Table 5.6: 2.45 GHz average complex magnitude of the electric field inside of a 8 in long cylinder centered around the feed as the auger rotates.

it along the cavity.

5.5.3 High Loss Material

The analysis of a higher loss, higher permittivity material (ε_r=8, tanδ=0.3) is somewhat simplified in the fact that very little power will propagate from the feed. The fields in Fig. 5.26 show very little penetration into the cavity. At this material composition, not much can really be done to it to improve the field homogeneity at the center of the cavity. With a similar averaged 8 in cylinder centered around the feed, the average magnitude of the electric field is only 12 V/m at 915 MHz and 3.1 V/m at 2.45 GHz.. By adding a center PEC cylinder to the cavity, Fig. 5.27, the field average is slightly improved to 12.4 V/m at 915 MHz and 3.4 V/m at 2.45 GHz. Not surprisingly, the averages in Table 5.7 tell a similar story. The average field across a 8 in long cylinder is incredibly low, to the point where a center PEC cylinder has an incredibly minimal effect on the field distribution. If this material is placed into the cavity, the rate of heat would be incredibly low without a significant amount of power.

Setup	$\lvert\mathbf{E}\rvert$ (V/m)
915 MHz a_z Cyl. Cavity	12.03
915 MHz a_z Coax. Cavity	12.34
2.45 GHz a_z Cyl. Cavity	3.11
2.45 GHz a_z Coax. Cavity	3.45

Table 5.7: Average complex magnitude of the electric field inside of a 8 in long cylinder centered around the feed with a high permittivity, high loss material.

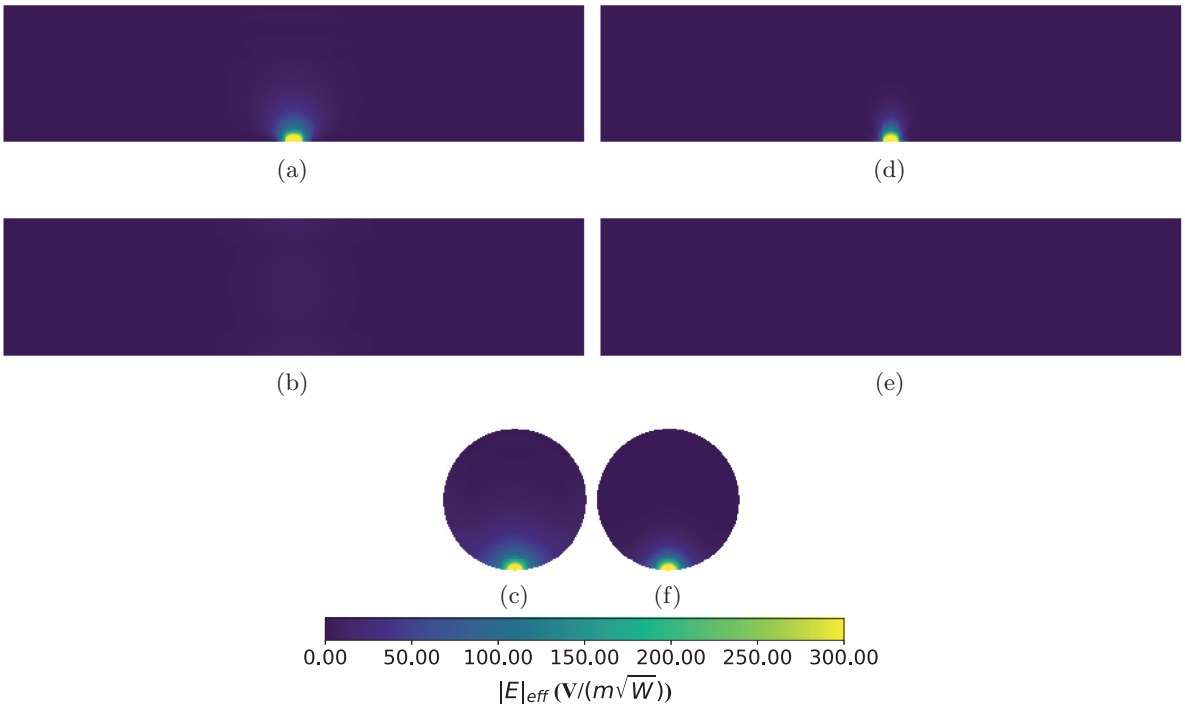

Figure 5.26: Double ridge waveguide excitation in the high-loss medium in the cylindrical cavity: (a) XZ, (b) YZ, and (c) XY plane cuts for 915 MHz and (d) XZ, (e) YZ, and (f) XY plane cuts for 2.45 GHz excitations.

5.5.4 Super-position of Sources

The spatial combining of these individual sources will be a key element of the microwave system. In order to compare the excitations properly, the sources will be scaled to the square root of the input power, giving an accurate scaling of the electric field with one watt input. In this section, only the coaxial cavity will be considered as it is determined to be necessary in the overall development of the system. The largest issue with the electrically large cavity, especially at 2.45 GHz will be the spatial coverage of the volume. With six excitations in phase and excited at the same magnitude for 915 MHz, Fig. 5.28, and 2.45 GHz, Fig. 5.29, the overall excitation coverage is increased fairly substantially. The efficiency of the excitation at 915 MHz increases from 74.7 to 83.3 $\frac{V}{m\sqrt{W}}$ for the a_z orientation and decreases from 72.1 to 67.6 $\frac{V}{m\sqrt{W}}$ for the a_y orientation. At 2.45 GHz the efficiency of the excitation decrease from 58.06 to 51.5 $\frac{V}{m\sqrt{W}}$ for the a_z orientation and from 48.06 to 43.3 $\frac{V}{m\sqrt{W}}$ for the a_y orientation. Unfortunately, the complex combining of the fields is not entirely

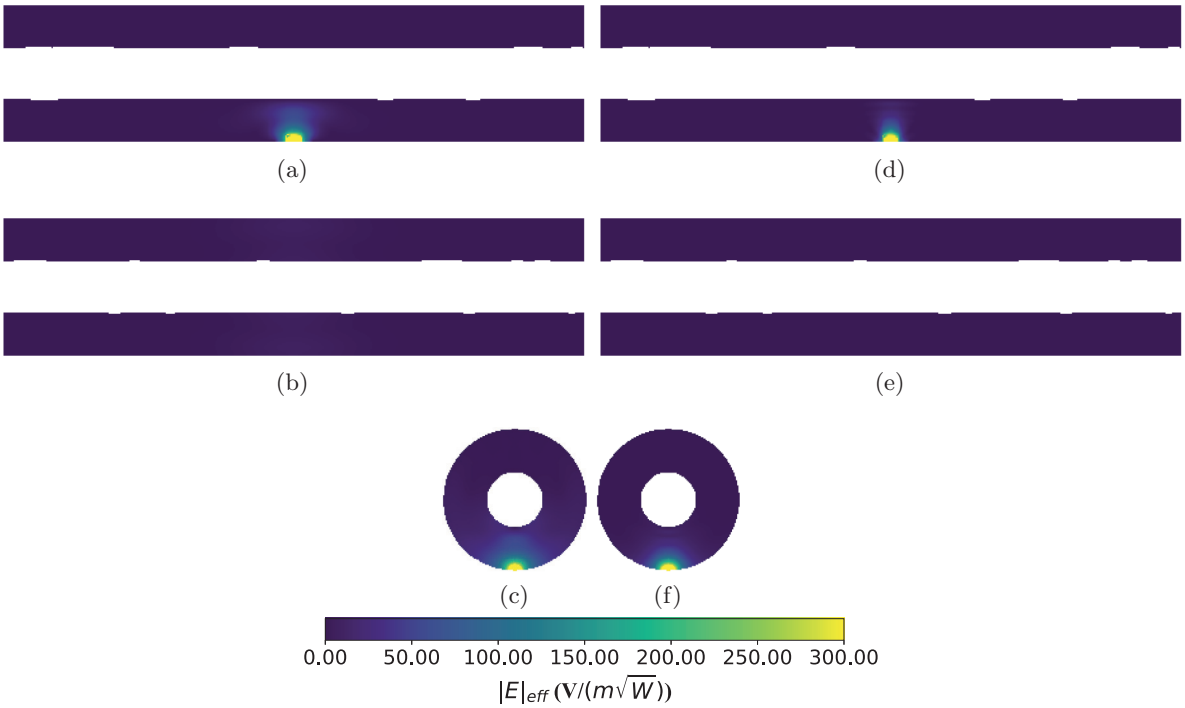

Figure 5.27: Double ridge waveguide excitation in the high-loss medium in the coaxial cavity: (a) XZ, (b) YZ, and (c) XY plane cuts for 915 MHz and (d) XZ, (e) YZ, and (f) XY plane cuts for 2.45 GHz excitations.

beneficial in field magnitude, however, the coverage is much higher. This result does not take into the account of the loss due to coupling. With the amount of loss in the system, the coupling will be relatively low. With 4 feeds spaced 90° apart, the couping is at a maximum of 17 dB in simulations. In practice, this should also be the lowest expected loss and permittivity, meaning the coupling should only decrease from here. The feeds can be phased together resulting in the field rotating slightly as opposed to homogenizing the heating volume.

More interestingly, the superposition using the metal auger creates much more interesting results. Similar to the process done in chapter 4, the domain is rotated around an individual feed. After the fields are exported in 10° increments, almost any reasonable combination of sources can be created. Twelve feeds are considered, still in phase and at the same magnitude excitations, with alternating orientations of the feed. The results is a further increase in homogenization of the heating volume and an increase to 97.6 $\frac{V}{m\sqrt{W}}$ at 915 MHz and 64.9 $\frac{V}{m\sqrt{W}}$ at 2.45 GHz.

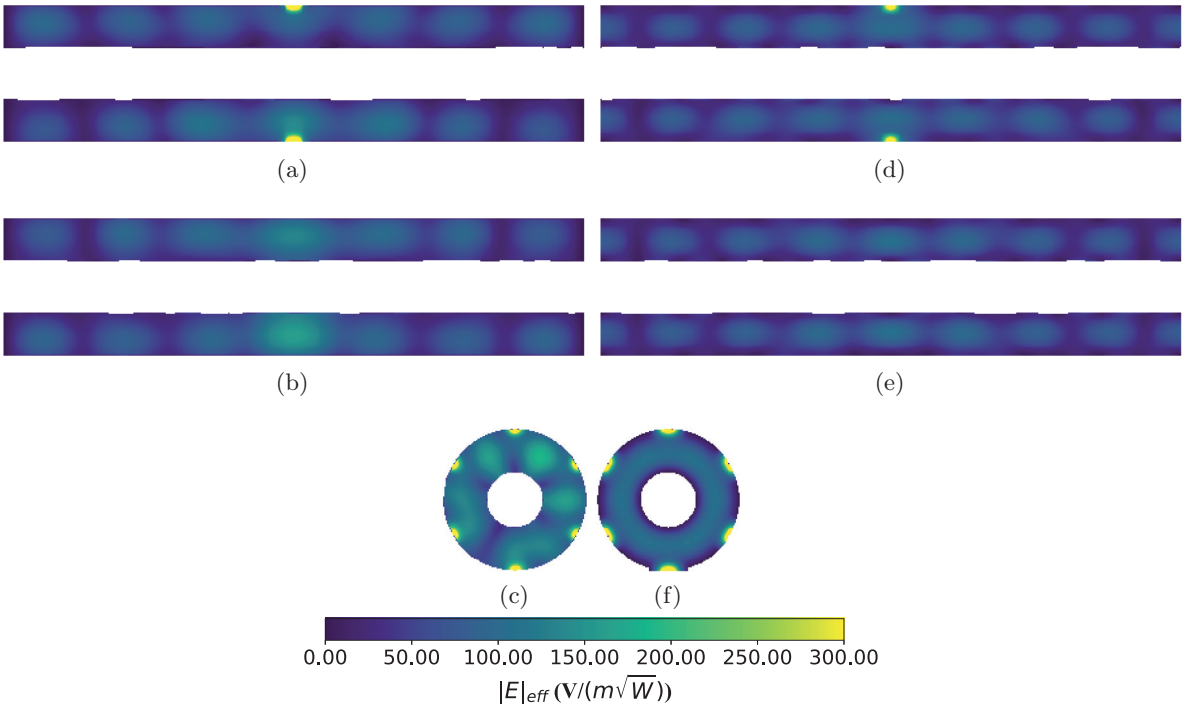

Figure 5.28: Super position of sources at 915 MHz with all excitations in phase and same magnitude: (a) XZ, (b) YZ, and (c) XY plane cuts a_z and (d) XZ, (e) YZ, and (f) XY plane cuts for a_y orientation.

At the same time, both 915 MHz and 2.45 GHz excitations can be combined to further improve the field homogeneity inside of the heating volume. Borrowing a proposed MRI technique [85], inhomogeneous excitations can be interleaved in time to improve the overall homogeneity of the combined field excitation. This would allow for combination of the magnitude squared (power combining) of the two field profiles instead of complex combining. Due to the long time constant, this would have a minimal effect on the overall heating of each individual excitation. It is apparent there is now a large increase in the number of excitable field profile possibilities inside of the cavity with power combining instead of complex combining. Fig. 5.31 shows the result with slightly higher homogenization than the previous two cases, however, these two frequencies do not complement each other incredibly well. This result shows a possibility for future work and that even two significantly different field profiles can be combined to create a slightly better field profile.

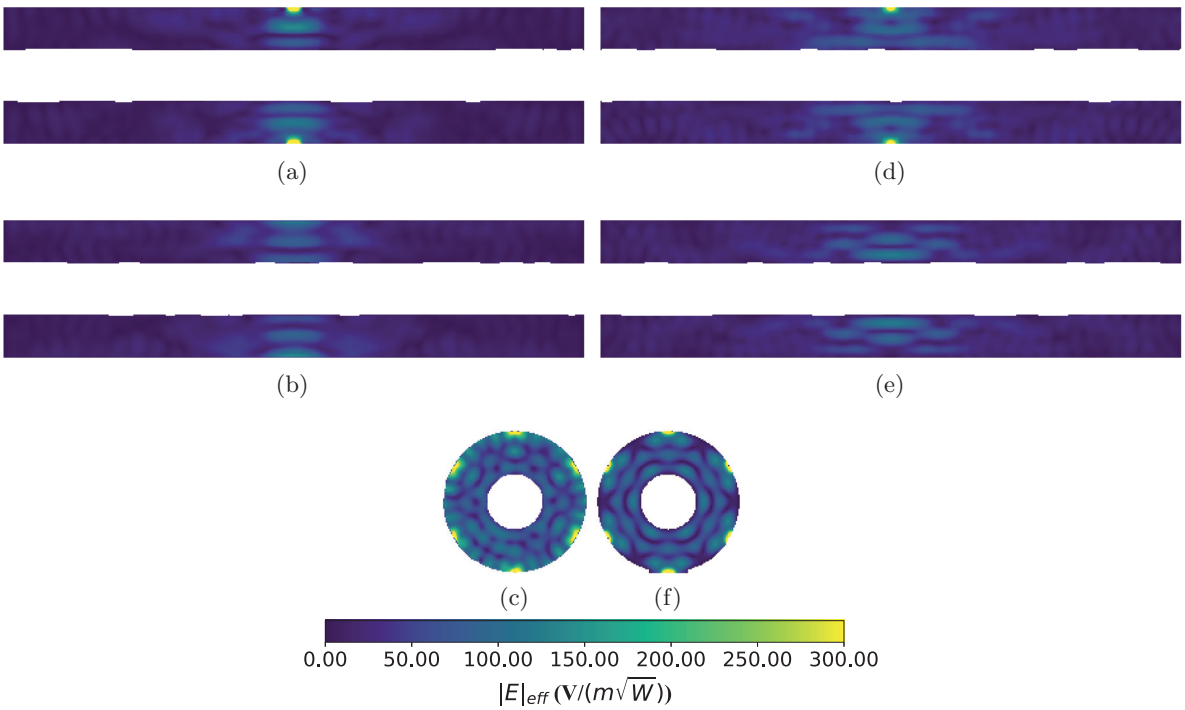

Figure 5.29: Super position of sources at 2.45 GHz with all excitations in phase and same magnitude: (a) XZ, (b) YZ, and (c) XY plane cuts a_z and (d) XZ, (e) YZ, and (f) XY plane cuts for a_y orientation.

5.6 Feeding the Microwave Cavity

Feeding the microwave cavity comes down to the desired type of source and coupling mechanism. Through the use of full-wave simulation software it is simple to drive a cavity and observe an excitation with minimal impact on the source itself, matching to any input or characteristic impedance. Section 5.5 observed driving a electrically large cavity with a double-ridge waveguide, without being concerned with the proper design of a transition. Fortunately, transitioning from a coaxial source to a double-ridged waveguide is relatively simple. The impedance of the double-ridged waveguide can range anywhere from 3 to 250 Ω depending on the ridge gap and width [86]. The low impedance allows for direct transition from a coaxial connector without any matching. These transitions can either be inline or at a right angle depending on the desired topology. For increased bandwidth, design of mode conversion networks and tapering to the height of the ridges can be employed [87].

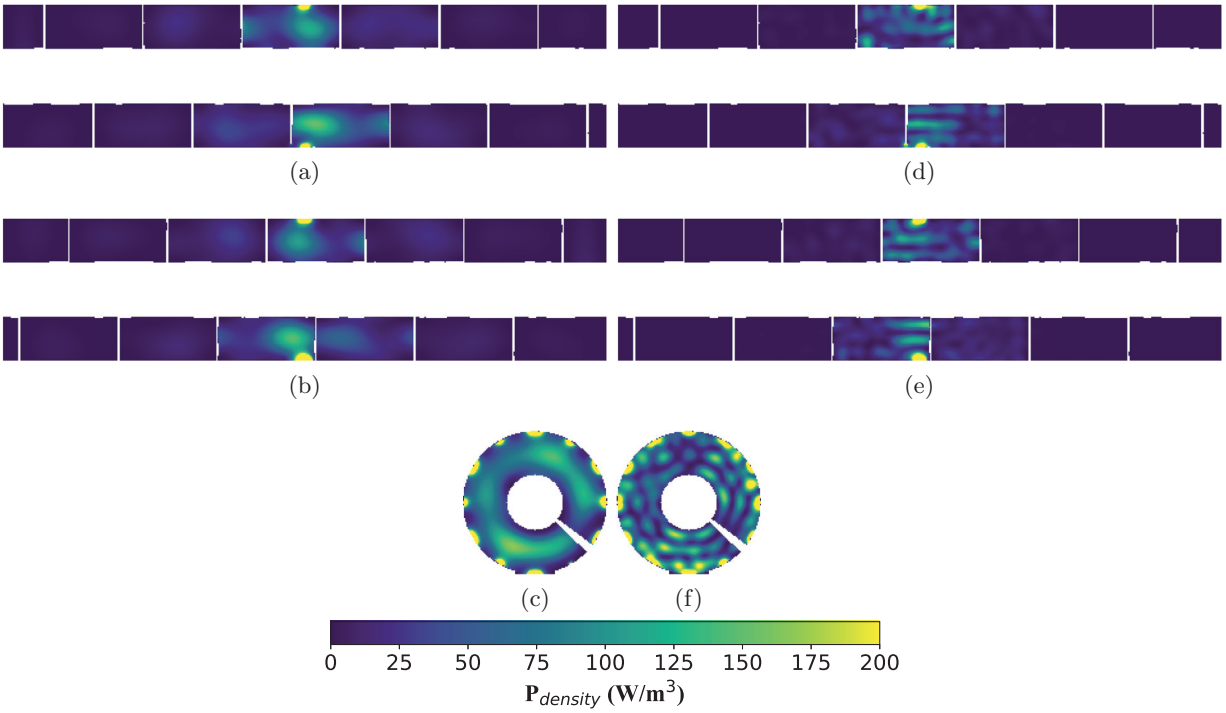

Figure 5.30: Super position of sources for alternating a_z and a_y orientations with all excitations with the same magnitude: (a) XZ, (b) YZ, and (c) XY plane cuts at 915 MHz in phase and (d) XZ, (e) YZ, and (f) XY plane cuts at 2.45 GHz with alternating 0 and 180° relative phasing.

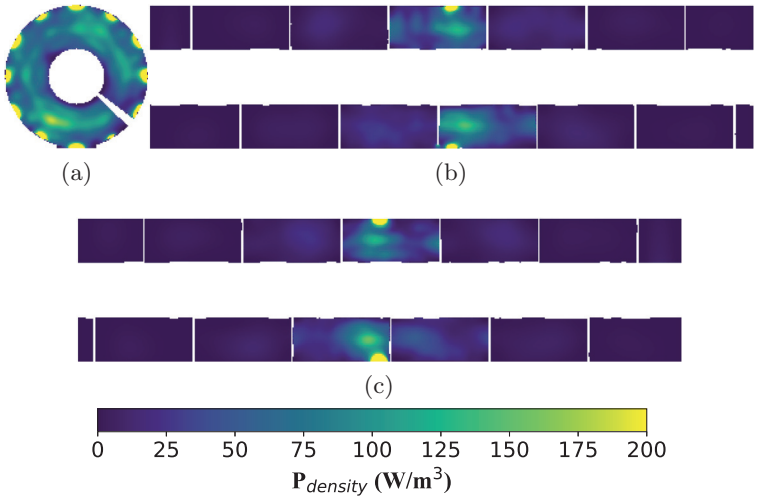

Figure 5.31: Super position of sources for alternating a_z and a_y orientations and combined with 915 MHz and 2.45 GHz with time interleaving.

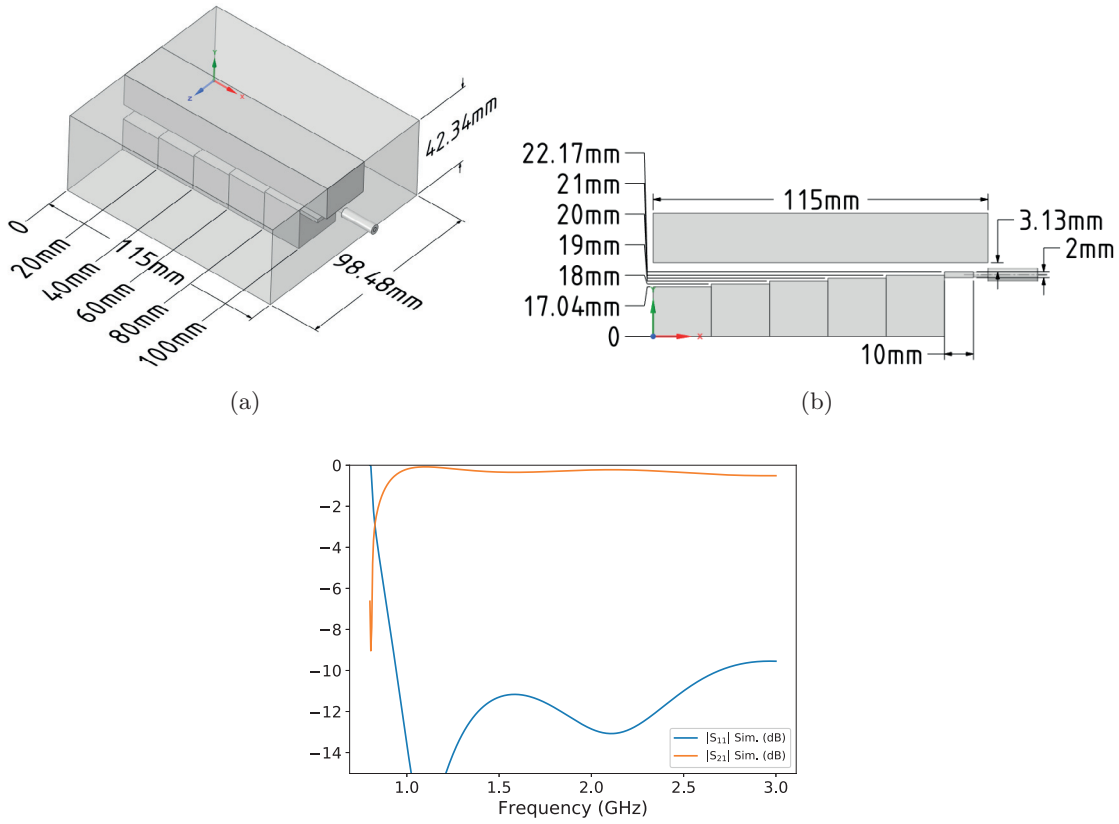

(a) (b)

(c)

Figure 5.32: Dimensions of the coaxial to double ridge-waveguide transition (a) perspective view and (b) plane view. (c) Simulated s-parameters of the designed transition.

This design will convert from a 50 Ω air coaxial line with a 2 mm center pin to the WRD-970U36 double-ridged waveguide and then connect to the electrically large cavity after a short waveguide section. In practice, the air coaxial line can be replaced with a connector with a dielectric with a small redesign due to the size of the center pin.

The design of the transition can be seen in Fig. 5.32 to contain 5 taper elements until a short mode conversion element, and then the center PEC conductor of the connector. Each taper element is 20 mm x 24.613 mm and increases the height of the ridge by 1 mm until the last taper element which is 21 mm tall. This height is chosen to be close to the radius of the coaxial connector, for smooth transition. The next small element is a 10 mm x 24.613 mm x 2 mm mode conversion box which converts from the radial electric field of the coaxial connector to one that is purely vertical of the waveguide. The largest challenge with this transition is operation near 915 MHz

Setup	Low-Loss 915 MHz Z_{in}	High-Loss 915 MHz Z_{in}	Low-Loss 2.45 GHz Z_{in}	High-Loss 2.45 GHz Z_{in}
a_z Cyl. Cavity	42.2+27.5j	175.4+122.8j	126.6+104.6j	176.9-92.2j
a_z Coax. Cavity	52.8+25.6j	174.4+127.1j	143.3+92.7j	176.8-91.7j
a_y Cyl. Cavity	31.1+3.4j	107.2+99.9j	32.9+0.9j	54.0+49.2j
a_y Coax. Cavity	46.7+14.7j	105.3+102.9j	39.1+1.9j	54.0+49.2j

Table 5.8: Input impedance for the coaxial to double-ridged waveguide transitions under various loading conditions and cavity setups.

due to its proximity to the cut-off frequency of the waveguide. Decreasing the insertion loss with this topology at a frequency lower than 1 GHz is difficult without increasing the impedance of the coaxial connector to be closer to the impedance of the waveguide at that frequency. The simulated s-parameters of the transition, Fig. 5.32c, show a 0.33 dB insertion loss and 11.33 dB return loss at 2.45 GHz. As expected, with this simple topology, the insertion loss is higher, 0.69 dB, due to the high impedance and return loss of 8.31 dB. As the setup changes, the input impedance varies quite a bit, as shown in Table 5.8. There is a benefit and drawback to this conclusion. The large difference in impedance allows for a high sensitivity for sensing the load, however, this now presents a huge issue for maintaining an efficient amplifier.

5.7 Conclusion

This chapter presents an analysis on the process and possibilities of creating an electrically large cavity targeting the heating, and eventual burning, of materials. By working from the initial analysis of the eigenmodes that are supported inside of the cavity, the structure can be designed with lower computational resources compared to a driven excitation. Additionally, a driven excitation only gives a small idea of the true characteristics of the microwave cavity, especially in a lossy medium where the energy will not fully excite a mode. The addition of a center PEC cylinder creates a coaxial cavity which lowers the over volume of the cavity, making it sightly easier to improve the heating. A double-ridged waveguide is determined to be the best overall excitation due to its wide-band capabilities, allowing it to excite both 915 MHz and 2.45 GHz modes without modifying

the feed. This will later allow for more interesting excitations as a switch could alternate between amplifiers. With the double-ridged waveguide excitation, the excitations can be compared to the eigenmode analysis to ensure that the excitation is in fact correct. With the creation of the coaxial cavity, the efficiency of the excitation increases by 20-30% depending on the orientation of the feed. To further improve the efficiency of the excitation, and to mix both the modes and the material itself, an auger is developed that would rotate around the center PEC cylinder. This auger can be made of any material that has a high melting temperature compared to the filled material. This chapter analyzes the use of both a metal and a ceramic auger. The benefits of a ceramic auger compared to a metal auger is the minimal effect on the field at low frequencies and some effect on the field at higher frequencies while still mixing the material and physically moving it along the cavity. With a larger system, this auger could be made of various materials along the length cavity. With smaller systems, the overall size can decrease, with the pitch of the blade affecting how much impact the auger will have on the field. The last portion of the field analysis shows that a superposition of sources can obtain a more homogeneous result, and generally increasing the efficiency of the field excitation slightly. The greatest benefit of superposition will be a time interleaved excitation which would allow for a more homogeneous result using both 915 MHz and 2.45 GHz excitations. The multiple frequencies would allow for different heating of the material given the electrical properties and the thermal properties will be different for each frequency. Lastly, an actual feed is developed as an inline coaxial to double-ridged waveguide transition. An inline transition is chosen to increase the number of possible excitations that would fit around the circumference of the cavity.

Chapter 6

Conclusion and Future Work

Contents

6.1 Summary and Contributions

This thesis presents the analysis and design of electromagnetic structures to improve on the field homogeneity inside of dielectric filled waveguides and cavities, from medical imaging to microwave heating. Even though waveguides and cavities are different structures, the systems that can be utilized to improve homogeneity are fairly similar. This conclusion summarizes the contributions of each chapter and then provide a path for future work.

Chapter 2 presents the development of an excitation scheme for small-bore research 16.4 T magnetic resonance imaging. The specifics of the probe design is explored for the excitation of a waveguide below cutoff loaded with different homogeneous imaging volumes. Boundary structures are developed to improve the coupling and the field distribution inside two different imaging volumes. This is necessary due to the placement of different sized patches inside of the waveguide.

The specific contributions are:

- Design of a new type of probe, a circular-polarized electrically small patch for traveling-wave imaging in a 16.4 T small-bore MRI.
- Traveling-wave excitations are compared to a current method and show a significantly different field structure due to the difference between exciting the waveguide and near-field coupling.
- With low signal-to-noise ratio and coupling to the phantom, an approximation of an electrically hard surface is developed and demonstrated an increase in SNR by 7 times and improve the field distribution inside of the imaging volume.
- Higher SNR allowed for imaging using a spin-echo pulse sequence. The spin-echo sequence requires a higher flip angle compared to the GRE pulse sequence and is able to compensate for system imperfections. This is the first traveling-wave spin-echo measurement.
- Analysis is extended to a shorter phantom to demonstrate the effect of distance on the coupling to the phantom.
- Paper accepted and presented at the International Microwave Symposium 2015 [19].

Chapter 3 expands on the 16.4 T small-bore work to a wide-bore 7 T MRI. With a wide-bore system, the waveguide is closer to cut-off and the propagation of the wave improves allowing for a closer look at the methods shown in Chapter 2. The specific contributions are:

- A study of the effect of distance on the SNR of the image. While obvious, there is an optimal distance between a large near-field effect and destruction of the circular polarization, and the reduction of the SNR because of waveguide attenuation.
- Further investigation of the use of an approximation to an electrically hard surface and showing different effects based on the placement of the copper strips over the imaging volume. This result showed that there are two main effects, the increase in coupling and the modification of the boundary around the imaging volume.

- The use of multiple probes for transmit and receive confirmed reciprocity between the transmit and receive profiles, a phenomenon not often seen due to the near-field nature of typical MRI RF excitations.

- Initial use of relative phasing (B_1 shimming) with traveling-wave excitations to confirm that previously used techniques and methods in MRI are applicable.

- Measurement and simulation of two different excitations on a small phantom at 10.5 T wide-bore imaging. This investigation showed that the primary mechanism determining the field structure inside of the imaging volume at high-field MRI is not the excitation itself, but the boundary and combining of the excitations.

- Computational analysis of various different boundary conditions placed on the simulation setup to show how much of the bore and gradient coil combination must be modeled for an accurate solution in order to speed up the solution.

- Published in IEEE Transactions Microwave Theory and Techniques [69] and poster at ISMRM 2016 highlighting the effects of the boundary structure improvements.

Chapter 4 takes the important information developed at 7 T and expands on the methodology and boundary structures to improve the homogeneity at 10.5 T. As of the time the measurements were taken, the 10.5 T scanner had been operational for a little over two years. As the same imaging volume as the previous chapter becomes electrically larger, the field profile becomes spatially much more complex. The specific contributions are:

- First traveling-wave images at 10.5 T, using a circular polarized patch and interdigitated capacitor probe array. Current excitation methods in literature up to the point of this thesis are either near-field dipoles placed directly on the imaging volume [25] or re-tuned 7 T coils.

- Demonstrated the use of a combination circular patch and a traveling-wave probe array as opposed to the more common method using microstrip lines.

- Utilized undriven helices to improve the coupling and improve field homogenization.
- Demonstrated the use of approximations of both electrically hard and soft surfaces to further improve the field homogenization.
- Measured two inhomogeneous imaging volumes to observe effect of a more realistic imaging volume on the excitation.
- Expanded the analysis to an anatomically correct human body model to observe possible methods of improving the field homogeneity around the brain.
- Published in IEEE Transactions Microwave Theory and Techniques title "Excitation and Field Control of a Human-Size 10.5-T MRI System" [88]. Currently unassigned to a specific edition as of the writing of this thesis. Initial designs presented at the International Microwave Symposium 2017 [78].

The last chapter, Chapter 5, switches topics to explore how the analysis can be transferred to electrically large cavities for a different application, that of burning nonuniform waste material. In this case, instead of optimizing homogeneity of the B1+ field, the goal is to obtain homogeneous distribution of the E-field since heating is proportional to $\sigma|E|^2$. The analysis begins with a simple look at a cylindrical and coaxial cavity, two well explored concepts [89]. The specific contributions are:

- Detailed analysis of a loaded, electrically large cavity using both eigenmode and driven solvers.
- Development of a auger system to mix modes and mix the material to provide improved homogenization of the physical material. The mixing of the material is a critical aspect of the solution to the problem and the physical mixing of the material will lead to improved functionality.
- Application of material mixing formulas, specifically Maxwell Garnett mixing formula and the upper and lower Wiener Bounds, commonly used in optics, to microwave applications.

- Apply a proposed MRI technique [85] of time interleaving modal structures to improve the field homogeneity inside of the heating volume.
- Lay the foundation of ground work to begin modifying the boundary conditions of the cavity to improve the field homogeneity and heating further.

6.2 Future Work

6.2.1 Ultra-High Field Magnetic Resonance Imaging

The methods developed for homogenization of the magnetic field show promise for improving and tailoring the field distribution over a given area of an imaging volume. The work presented in this thesis can be extended in a few directions. First, the traveling-wave interdigitated capacitor probes currently use resistors to balance the current. Simulations showed that it was possible to remove them with adequate loading, as such, a slight redesign could improve SNR and image quality.

Second, this thesis presented an engineering approach towards exploring different options for improving the field homogeneity at the cost of complexity. More complex solutions could possible improve the results. Looking further at inhomogeneous, or an ASTM phantom, would highlight benefits and drawbacks to each solution. By modeling an anatomically correct human body model, the simulation setup and results highlighted how different patients or imaging volumes will effect the result with a large effect if the structures are close to the volume. The metallic structures are fairly simple and increasing the complexity is likely to result in a more uniform field across different volumes by using tunable structures.

Lastly, if the approach with electrically hard and soft metallic structures were to become adopted for *in vivo* imaging, considerations would need to be put in place to keep the metal from burning the skin. Theory and analysis are likely to show that the structures can be placed away from the imaging volume with decreased effectiveness. By placing an intermediary dielectric between the metal and the skin, much of the heat would be dissipated in the dielectric and not affect the

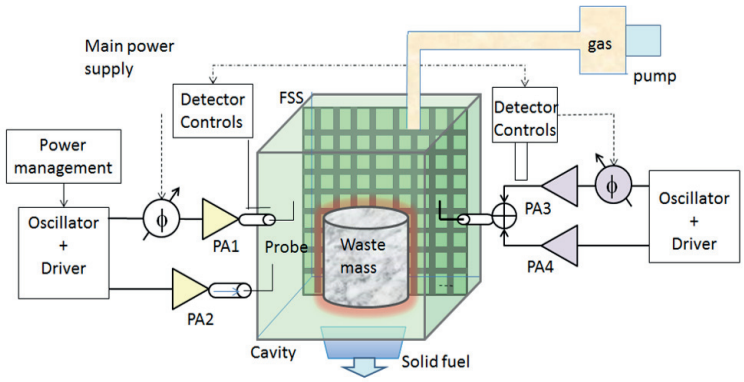

Figure 6.1: Microwave waste-to-fuel system diagram showing potential directions to further control the field.

patient/animal. However, this method could still be applicable to *in vitro* imaging as the heating would not be an issue.

6.2.2 Electrically Large Cavities for Scalable Waste to Fuel Conversion

This project is in it's beginnings and the cavity simulations presented in chapter 5 are a natural extension of the work in ultra-high field MRI. The complete system is shown in Fig. 6.1, showing a generalized approach for adaptive heating of a material mixture using multiple feeds. Each feed is connected to high-efficiency microwave source and relative phasing between the sources is expected to be helpful in improving heating uniformity. Initial work in examining relative phasing is described in chapter 5 for only two frequencies and a similar analysis that includes frequency, amplitude, and phase variations is a promising future direction. Adaptivity can be added by sensing the reflection coefficient at strategic places to improve heating and efficiency of the sources which is important for protecting the final high-power amplifier stages from unwanted high reflections. While this can be accomplished with a circulator, it is also possible to reduce the loss in the dummy load by instead using a pair of load-modulated amplifiers. In the latter case, relative phasing between the amplifiers can compensate for load mismatches dynamically [90], while combining the power of two lower-power and therefore more efficient amplifiers.

The cavity design itself has many different directions for improvement in manipulating the field

distribution. A simple cylindrical cavity is necessary to start with for analysis, however, it is not the only method. A tapered approach along the length of the cavity as the material will heats and the size and density is reduced could prove beneficial. The material change as it heats will be a large concern that must be considered. For the coaxial cavity, the material, shape, width, and height of the auger are also different variables that can be leveraged to help alleviate concern. There is no reason the auger itself must maintain the same shape throughout the cavity. This thesis shows an initial design of the auger where more parameters can be varied to improve the performance.

The modeling of the material could increase in simplicity with the addition of an added known material. The bounds of high-loss and low-loss material both can create an issue with the design and operation of the cavity. The low-loss material requires a substantial amount of power to heat a similar amount compared to the high-loss material. Unfortunately, with just the materials listed in the Navy study [79], the high-loss is also coupled to high-permittivity, reducing the overall penetration of the field inside of the cavity. The addition of a known material, such as distilled water (medium-loss, high permittivity) to the low-loss case or oil (low-loss, low-permittivity) to the high-loss case could place the effective mixture at an operating point for optimal heating and field coupling. A study on the variation of fill factor on the field distribution and the loading of the feed is possibly a necessary step towards homogenization. This parameter, however, is something that is easily controlled and could be another parameter for the homogenization of the field and heating of the material.

A further method to improve the heating and field homogeneity is by modifying the boundary conditions of the microwave cavity, similar to what was presented in chapters 2-4. The addition of a fire brick, or other high temperature co-fired ceramic, would isolate the internal material from the outer metal walls. The giant metal wall of the cavity and the internal conductor will operate as a heatsink, reducing the effectiveness of the heating. The addition of a fire brick would also serve as a dielectric to modify the field around the walls of the cavity. The feed itself would need to be placed further in the cavity for its effectiveness to not be reduced by the high-loss fire brick, enabling more options for modes that can be excited by a given feed. With the feed placed on

the wall of the cavity, at lower frequencies, the feed can only excite the H-field as the tangential E cannot exist near the feed.

The power sources are an essential part of the system from Fig. 6.1 and are closely related to cavity scaling, both in terms of power and size. For lower power, smaller cavities, solid-state sources are a reasonable approach for high-efficiency. At UHF frequencies, LDMOS transistors can provide kilowatts of power at efficiencies above 70%. At microwave frequencies, GaN HEMTs are the most promising technology. In appendix A, an above 60% PAE 70 W GaN HEMT is described for small scale microwave heating. This power is scalable to 2 kW at 1 GHz for L-band radar and above 700 W for 2 GHz base stations. For higher-power levels and larger systems, magnetrons are an obvious solution, however, there are drawbacks. The efficiency can be anywhere from 40-70% [91], but if the load differs too greatly, the frequency of the oscillation can shift. Frequency stability will be a large issue with a heavily loaded cavity and coupling between sources. The use of a solid-state power-combined PAs could alleviate some of these concerns due to inherent frequency stability, as the oscillator is farther back in the chain. By sacrificing power of each individual PA, its efficiency can reach 80% and combining a larger number can increase the power out.

Bibliography

[1] I. I. Rabi, J. R. Zacharias, S. Millman, and P. Kusch, "A new method of measuring nuclear magnetic moment," *Phys. Rev.*, vol. 53, pp. 318–318, Feb 1938. 5

[2] R. Damadian, "Tumor detection by nuclear magnetic resonance," *Science*, vol. 171, no. 3976, pp. 1151–1153, 1971. 6

[3] P. Mansfield and P. K. Grannell, "NMR 'diffraction' in solids?" *Journal of Physics C: Solid State Physics*, vol. 6, pp. L422–L426, 1973. 6

[4] E. Haacke, R. Brown, M. Thompson, and R. Venkatesan, *Magnetic Resonance Imaging.* John Wiley & Sons Ltd, 2014, ch. 1,27, pp. 4,827–858. 7, 10, 38

[5] E. Lucano, M. Liberti, G. G. Mendoza, T. Lloyd, M. I. Iacono, F. Apollonio, S. Wedan, W. Kainz, and L. M. Angelone, "Assessing the electromagnetic fields generated by a radiofrequency mri body coil at 64 mhz: Defeaturing versus accuracy," *IEEE Transactions on Biomedical Engineering*, vol. 63, no. 8, pp. 1591–1601, 2016. 11

[6] P. Roemer, W. A. Edelstein, C. E. Hayes, S. P. Souza, and O. M. Mueller, "The NMR phased array," *Magn. Reson. Med.*, vol. 16, no. 2, pp. 192–225, 1990. 10

[7] J. T. Vaughan, H. P. Hetherington, J. O. Otu, J. W. Pan, and G. M. Pohost, "High frequency volume coils for clinical NMR imaging and spectroscopy," *Magn. Reson. Med.*, vol. 32, no. 2, pp. 206–218, 1994. 10

[8] R. H. Caverly, "MRI fundamentals: RF aspects of magnetic resonance imaging (MRI)," *IEEE Microwave Mag.*, vol. 16, no. 6, pp. 20–33, July 2015. 10

[9] K. Haines, J. A. Muniz, I. S. Masad, E. Semouchkina, M. Lanagan, A. Webb, and S. Grant, "MR microimaging with a cylindrical ceramic dielectric resonator at 21.1T," presented at the 51st ENC Experimental Nuclear Magnetic Resonance Conf., Daytona Beach, Fl, April 18-23, 2010. 11

[10] R. Fu, W. Brey, K. Shetty, P. Gor'kov, S. Saha, J. Long, S. Grant, E. Chekmenev, J. Hu, Z. Gan *et al.*, "Ultra-wide bore 900 MHz high-resolution NMR at the national high magnetic field laboratory," *Journal of magnetic resonance*, vol. 177, no. 1, pp. 1–8, 2005. 11

[11] V. Schepkin, W. W. Brey, P. L. Gor'kov, and S. C. Grant, "Initial in vivo rodent sodium and proton MR imaging at 21.1T," *Magn. Reson. Imaging*, vol. 28, no. 3, pp. 400–407, 2010. 11

[12] K. Ugurbil, "Magnetic resonance imaging at ultrahigh fields," *IEEE Trans. Biomed. Eng.*, vol. 61, no. 5, pp. 1364–1379, May 2014. 11

[13] U. Food and D. Administration, "Fda clears first 7t magnetic resonance imaging device," October 2017. [Online]. Available: https://www.fda.gov/NewsEvents/Newsroom/PressAnnouncements/ucm580154.htm 12

[14] B. Wu, C. Wang, D. A. C. Kelley, D. Xu, D. B. Vigneron, S. J. Nelson, and X. Zhang, "Shielded microstrip array for 7t human mr imaging," *IEEE Transactions on Medical Imaging*, vol. 29, no. 1, pp. 179–184, Jan 2010. 12

[15] I. R. Connell, K. M. Gilbert, M. A. Abou-Khousa, and R. S. Menon, "Design of a parallel transmit head coil at 7t with magnetic wall distributed filters," *IEEE transactions on medical imaging*, vol. 34, no. 4, pp. 836–845, 2015. 12

[16] S. M. Sohn, L. DelaBarre, A. Gopinath, and J. T. Vaughan, "RF head coil design with improved RF magnetic near-fields uniformity for magnetic resonance imaging (MRI) systems," *IEEE Trans. Microwave Theory Tech.*, vol. 62, no. 8, pp. 1784–1789, Aug 2014. 12, 13

[17] B. Wu, C. Wang, J. Lu, Y. Pang, S. J. Nelson, D. B. Vigneron, and X. Zhang, "Multi-channel microstrip transceiver arrays using harmonics for high field MR imaging in humans," *IEEE Trans. Med. Imaging*, vol. 31, no. 2, pp. 183–191, Feb 2012. 12

[18] A. J. Raaijmakers, M. Italiaander, I. J. Voogt, P. R. Luijten, J. M. Hoogduin, D. W. Klomp, and C. A. van den Berg, "The fractionated dipole antenna: A new antenna for body imaging at 7 Tesla," *Magn. Reson. Med.*, vol. 75, no. 3, pp. 1366–1374, 2016. 12

[19] P. Bluem, A. Tonyushkin, D. Deelchand, G. Adriany, P. F. V. de Moortele, A. J. M. Kiruluta, and Z. Popovic, "Travelling-wave excitation for 16.4T small-bore MRI," in *Proc. IEEE MTT-S Int. Microwave Symp. (IMS)*, May 2015, pp. 1–4. 12, 35, 41, 130

[20] D. Brunner, N. D. Zanche, J. Frohlich, J. Paska, and K. P. Pruessmann, "Travelling-wave nuclear magnetic resonance," *Nature*, vol. 457, no. 7232, pp. 994–998, Feb. 2009. 12, 13, 14, 39, 54, 65

[21] J. Hoffmann, G. Shajan, J. Budde, K. Scheffler, and R. Pohmann, "Human brain imaging at 9.4 T using a tunable patch antenna for transmission," *Magn. Reson. Med.*, vol. 69, no. 5, pp. 1494–1500, 2013. 12, 14

[22] G. Shajan, J. Hoffmann, D. Z. Balla, D. K. Deelchand, K. Scheffler, and R. Pohmann, "Rat brain MRI at 16.4T using a capacitively tunable patch antenna in combination with a receive array," *NMR in Biomedicine*, vol. 25, no. 10, pp. 1170–1176, 2012. 12

[23] A. Andreychenko, H. Kroeze, V. O. Boer, J. J. W. Lagendijk, P. R. Luijten, and C. A. T. van den Berg, "Improved steering of the rf field of traveling wave MR with a multimode, coaxial waveguide," *Magn. Reson. Med.*, vol. 71, no. 4, pp. 1641–1649, 2014. 12, 14

[24] G. Adriany, P.-F. Van de Moortele, F. Wiesinger, S. Moeller, J. P. Strupp, P. Andersen, C. Snyder, X. Zhang, W. Chen, K. P. Pruessmann, P. Boesiger, T. Vaughan, and K. Ugurbil, "Transmit and receive transmission line arrays for 7 Tesla parallel imaging," *Magn. Reson. Med.*, vol. 53, no. 2, pp. 434–445, 2005. 12

[25] M. A. Ertürk, X. Wu, Y. Eryaman, P.-F. Moortele, E. J. Auerbach, R. L. Lagore, L. DelaBarre, J. T. Vaughan, K. Uğurbil, G. Adriany *et al.*, "Toward imaging the body at 10.5 Tesla," *Magnetic Resonance in Medicine*, vol. 77, no. 1, pp. 434–443, 2017. 13, 72, 131

[26] F. Geschewski, D. Brenner, J. Felder, and N. J. Shah, "Optimum coupling and multimode excitation of traveling-waves in a whole-body 9.4T scanner," *Magn. Reson. Med.*, vol. 69, no. 6, pp. 1805–1812, 2013. 14

[27] A. Andreychenko, H. Kroeze, D. W. J. Klomp, J. J. W. Lagendijk, P. R. Luijten, and C. A. T. van den Berg, "Coaxial waveguide for travelling wave MRI at ultrahigh fields," *Magn. Reson. Med.*, vol. 70, no. 3, pp. 875–884, 2013. 14

[28] A. G. Webb, C. M. Collins, M. J. Versluis, H. E. Kan, and N. B. Smith, "MRI and localized proton spectroscopy in human leg muscle at 7 Tesla using longitudinal traveling waves," *Magn. Reson. Med.*, vol. 63, no. 2, pp. 297–302, 2010. 14

[29] A. Tonyushkin, J. A. Muniz, S. C. Grant, and A. J. M. Kiruluta, "Traveling wave mri in a vertical bore 21.1-T system," presented at the Int. Society Magnetic Resonance in Medicine, Melbourne, Australia, May 5-11, 2012. 14

[30] A. Tonyushkin, N. Konyer, M. Noseworthy, and A. J. M. Kiruluta, "Imaging with dielectric waveguide approach for 3T MRI," presented at the Int. Society Magnetic Resonance in Medicine, Melbourne, Australia, May 5-11, 2012. 14

[31] J. A. Tang, G. C. Wiggins, D. K. Sodickson, and A. Jerschow, "Cutoff-free traveling wave NMR," *Concepts in Magnetic Resonance Part A*, vol. 38A, no. 5, pp. 253–267, 2011. 14

[32] W. Koning, J. J. Bluemink, E. A. J. Langenhuizen, A. J. Raaijmakers, A. Andreychenko, C. A. T. van den Berg, P. R. Luijten, J. J. M. Zwanenburg, and D. W. J. Klomp, "High-resolution MRI of the carotid arteries using a leaky waveguide transmitter and a high-density receive array at 7T," *Magn. Reson. Med.*, vol. 69, no. 4, pp. 1186–1193, 2013. 14

[33] O. Ipek, A. J. E. Raaijmakers, D. W. J. Klomp, J. J. W. Lagendijk, P. R. Luijten, and C. A. T. van den Berg, "Characterization of transceive surface element designs for 7 Tesla magnetic resonance imaging of the prostate: radiative antenna and microstrip," *Phys. Med. Biol.*, vol. 57, no. 2, p. 343, 2012. 14

[34] C. Gabriel, "Compilation of the dielectric properties of body tissues at rf and microwave frequencies." KING'S COLL LONDON (UNITED KINGDOM) DEPT OF PHYSICS, Tech. Rep., 1996. 14

[35] K. S. Cole and R. H. Cole, "Dispersion and absorption in dielectrics i. alternating current characteristics," *The Journal of chemical physics*, vol. 9, no. 4, pp. 341–351, 1941. 14

[36] M.-C. Gosselin, E. Neufeld, H. Moser, E. Huber, S. Farcito, L. Gerber, M. Jedensjö, I. Hilber, F. Di Gennaro, B. Lloyd *et al.*, "Development of a new generation of high-resolution anatomical models for medical device evaluation: the virtual population 3.0," *Physics in medicine and biology*, vol. 59, no. 18, p. 5287, 2014. 15, 20, 82

[37] "Coke manufacturing," in *Pollution Prevention and Abatement Handbook*. World Bank Group, July 1998. 15

[38] Heyl & Patterson Inc, "The roles of coal and coke in steelmaking," in *Heyl & Patterson Blog*, July 2014. 15

[39] L. Koottungal, "2010 worldwide refining survey," in *Oil & Gas Journal*, December 2010. 16

[40] E. O. Oluyede and J. N. Phillips, "Fundamental impact of firing syngas in gas turbines," in *ASME Turbo Expo 2007: Power for Land, Sea, and Air*, May 2007, vol. 3. 16

[41] S. Gonzalez-Cortes, D. R. Slocombe, T. Xiao, A. Aldawsari, B. Yao, V. Kuznetsov, E. Liberti, A. Kirkland, M. Alkinani, H. Al-Megren *et al.*, "Wax: A benign hydrogen-storage material that rapidly releases h 2-rich gases through microwave-assisted catalytic decomposition," *Scientific reports*, vol. 6, p. 35315, 2016. 16, 18

[42] T. M. Lenton and N. E. Vaughan, "The radiative forcing potential of different climate geoengineering options," *Atmospheric Chemistry and Physics*, vol. 9, no. 15, pp. 5539–5561, 2009. 16

[43] C. S. Alig, L. Koss, T. Scarano, and F. Chitty, "Control of plastic wastes aboard naval ships at sea," *Activities Report of the R and D Associates (USA)*. 16

[44] V. Vaughn. (2002, July) How do you take the trash out at sea? [Online]. Available: http://www.navy.mil/submit/display.asp?story_id=2712 16

[45] *Marpol Annex V*, ch. Garbage Disposal Restrictions. 16

[46] J. Johndro. (2011, May) Stennis waste management saves money, environment. [Online]. Available: http://www.navy.mil/submit/display.asp?story_id=60265 17

[47] A. of Mathematical, P. S. U. N. S. Board, and N. R. C. U. C. on Shipboard Pollution Control, *Shipboard Pollution Control: U.S. Navy Compliance with MARPOL Annex V*. National Academy Press, ch. Waste handling on Submarines, pp. 41–56. 17

[48] D. Davis, "Waste-to-energy mmachine reveals power of trash," April 2016. 17

[49] A. Austin, "Us army invests $1.5 million to develop mobile pyrolysis system," Biomass Magazine. 17

[50] J. Palmer, "Energy-from-waste powers US army," BBC News, October 2009. 17

[51] Department of the Army, "Guidelines for field waste management," September 2006. 17

[52] A. Austin, "Trash tactics in iraq." 17

[53] P. L. Spencer, "Prepared food article and method of preparing," Aug. 30 1949, uS Patent 2,480,679. 18

[54] S. Carr and C. Moser, "The use of microwave technology for dry ashing procedures," in *CEM Corporation, presented at Pittsburgh Conference*, 1991. 18

[55] W. G. Voss, "Factors affecting the operation of high-power microwave heating systems for lumber processing," *IEEE Transactions on Industry and General Applications*, no. 3, pp. 234–243, 1966. 18, 91, 94

[56] D. Bluhm, G. Fanslow, and S. Nelson, "Enhanced magnetic separation of pyrite from coal after microwave heating," *IEEE Transactions on Magnetics*, vol. 22, no. 6, pp. 1887–1890, November 1986. 18

[57] V. V. Yakovlev, "Frequency control over the heating patterns in a solid-state dual-source microwave oven," in *Microwave Symposium (IMS), 2015 IEEE MTT-S International*. IEEE, 2015, pp. 1–4. 19

[58] Carbonscape. [Online]. Available: http://www.carbonscape.com 19

[59] US Food and Drug Administration, "performance standards for microwave and radio frequency emitting products," in *J–Radiological Health*, April 2017, ch. 1030.10 Microwave Ovens. 19

[60] Nasimuddin, X. Qing, and Z. N. Chen, "Compact circularly polarized symmetric-slit microstrip antennas," *IEEE Antennas and Propagation Magazine*, vol. 53, no. 4, pp. 63–75, Aug 2011. 26

[61] X. L. Bao and M. J. Ammann, "Compact annular-ring embedded circular patch antenna with cross-slot ground plane for circular polarisation," *Electron. Lett.*, vol. 42, no. 4, pp. 192–193, Feb 2006. 29, 40

[62] S. Ramo, J. R. Whinnery, and T. V. Duzer, *Fields and Waves in Communication Electronics*. John Wiley & Sons Ltd, 1994, ch. 8, p. 430. 39, 63

[63] I. A. Elabyad, A. Omar, T. Herrmann, J. Mallow, and J. Bernarding, "Travelling wave approach for high field magnetic resonance imaging," in *IEEE 3rd Int. Symp. Applied Sciences Biomedical and Communication Technologies (ISABEL)*, Nov 2010, pp. 1–5. 39

[64] E. Lier and P. S. Kildal, "Soft and hard horn antennas," *IEEE Trans. Antennas Propag.*, vol. 36, no. 8, pp. 1152–1157, Aug 1988. 41, 42, 73

[65] G. Ruvio, P. S. Kildal, and S. Maci, "Modal propagation in ideal soft and hard waveguides," in *Proc. IEEE Antennas and Propagation Soc. Int. Symp.*, vol. 4, June 2003, pp. 438–441 vol.4. 42, 72, 73

[66] O. Dietrich, J. G. Raya, S. B. Reeder, M. F. Reiser, and S. O. Schoenberg, "Measurement of signal-to-noise ratios in MR images: Influence of multichannel coils, parallel imaging, and reconstruction filters," *J. Magn. Reson. Imaging*, vol. 26, no. 2, pp. 375–385, 2007. 45

[67] A. J. M. Kiruluta, "The emergence of the propagation wave vector in high field NMR: analysis and implications," *J. Phys. D: Appl. Phys.*, vol. 40, no. 10, p. 3043, 2007. 54

[68] R. K. S. Kwan, A. C. Evans, and G. B. Pike, "MRI simulation-based evaluation of image-processing and classification methods," *IEEE Trans. Med. Imaging*, vol. 18, no. 11, pp. 1085–1097, Nov 1999. 57

[69] P. Bluem, A. Kiruluta, P. F. V. de Moortele, A. Duh, G. Adriany, and Z. Popovic, "Patch-probe excitation for ultrahigh magnetic field wide-bore mri," *IEEE Transactions on Microwave Theory and Techniques*, vol. 65, no. 7, pp. 2547–2557, July 2017. 60, 65, 72, 73, 131

[70] NIST. ISMRM/NIST system phantom. [Online]. Available: http://www.hpd-online.com/system-phantom.php 63

[71] V. L. Yarnykh, "Actual flip-angle imaging in the pulsed steady state: a method for rapid three-dimensional mapping of the transmitted radiofrequency field," *Magnetic resonance in Medicine*, vol. 57, no. 1, pp. 192–200, 2007. 64

[72] P.-F. Van de Moortele, C. Snyder, L. DelaBarre, G. Adriany, J. Vaughan, and K. Ugurbil, "Calibration tools for RF shim at very high field with multiple element RF coils: from ultra fast local relative phase to absolute magnitude B1+ mapping," in *Proc Intl Soc Mag Reson Med*, vol. 15, 2007, p. 1676. 65

[73] P. Van de Moortele and K. Ugurbil, "Very fast multi channel B1 calibration at high field in the small flip angle regime," in *Proceedings of the 17th Annual Meeting of ISMRM, Honolulu, Hawaii, USA*, 2009, p. 367. 65

[74] G. J. Metzger, E. J. Auerbach, C. Akgun, J. Simonson, X. Bi, K. Uğurbil, and P.-F. van de Moortele, "Dynamically applied B1+ shimming solutions for non-contrast enhanced renal angiography at 7.0 tesla," *Magnetic resonance in medicine*, vol. 69, no. 1, pp. 114–126, 2013. 65

[75] A. Munir and E. K. Sari, "Printed traveling wave antenna composed of interdigital capacitor structure for wireless communication application," in *2015 International Seminar on Intelligent Technology and Its Applications (ISITIA)*, May 2015, pp. 441–444. 66

[76] Y. M. Madany, D. A. Mohamed, and B. I. Halim, "Analysis and design of microstrip antenna array using interdigital capacitor with CRLH-TL ground plane for multiband applications," in *The 8th European Conference on Antennas and Propagation (EuCAP 2014)*, April 2014, pp. 922–926. 66

[77] R. Schmidt and A. Webb, "Improvements in RF shimming in high field MRI using high permittivity materials with low order pre-fractal geometries," *IEEE Transactions on Medical Imaging*, vol. 35, no. 8, pp. 1837–1844, Aug 2016. 72

[78] P. Bluem and Z. Popovic, "10.5-t mri volume excitation using traveling-wave microstrip probes," in *2017 IEEE MTT-S International Microwave Symposium (IMS)*, June 2017, pp. 1396–1399. 88, 132

[79] "Overall military waste - city of san diego waste characterization study," 2013. 91, 135

[80] "Xii. colours in metal glasses and in metallic films," *Philosophical Transactions of the Royal Society of London A: Mathematical, Physical and Engineering Sciences*, vol. 203, no. 359-371, pp. 385–420, 1904. 91

[81] P. L. Dulong and A.-T. Petit, *Recherches sur quelques points importans de la theorie de la Chaleur*, 1819. 92

[82] D. Hill, "Motivation for statistical approaches," in *Electromagnetic Fields in Cavities*. Wiley, 2009, ch. 5, pp. 78–79. 94

[83] M. N. Sadiku, *Numerical techniques in electromagnetics*. CRC press, 2000, ch. 4, p. 275. 96

[84] R. E. Collin, *Field theory of guided waves*. McGraw-Hill, 1960, ch. 5, pp. 362–384. 97

[85] S. Orzada, S. Maderwald, B. A. Poser, A. K. Bitz, H. H. Quick, and M. E. Ladd, "Rf excitation using time interleaved acquisition of modes (tiamo) to address b1 inhomogeneity in high-field mri," *Magnetic resonance in medicine*, vol. 64, no. 2, pp. 327–333, 2010. 105, 123, 133

[86] S. B. Cohn, "Properties of ridge wave guide," *Proceedings of the IRE*, vol. 35, no. 8, pp. 783–788, Aug 1947. 124

[87] Y. Zhou, E. Li, G.-F. Guo, T. Yang, and L.-S. Liu, "Design of millimeter wave wideband transition from double-ridge waveguide to coaxial line," *Journal of Infrared, Millimeter, and Terahertz Waves*, vol. 32, no. 1, pp. 26–33, Jan 2011. 124

[88] P. Bluem, P. V. de Moortele, G. Adriany, and Z. Popovic, "Excitation and rf field control of a human-size 10.5-t mri system," *IEEE Transactions on Microwave Theory and Techniques*, pp. 1–13, 2018. 132

[89] R. N. Bracewell, "Charts for resonant frequencies of cavities," *Proceedings of the IRE*, vol. 35, no. 8, pp. 830–841, Aug 1947. 132

[90] C. Sánchez-Pérez, D. Sardin, M. Roberg, J. de Mingo, and Z. Popović, "Tunable outphasing for power amplifier efficiency improvement under load mismatch," in *Microwave Symposium Digest (MTT), 2012 IEEE MTT-S International*. IEEE, 2012, pp. 1–3. 134

[91] R. J. Meredith, *Engineers' handbook of industrial microwave heating*. Iet, 1998, no. 25, ch. 9, pp. 254–268. 136

Appendix A

Microwave Sources for High Power Applications

A.1 Microwave Sources

Microwave sources for high power come in many different shapes and sizes depending on the chosen application. Depending on the frequency and required power, typical options include solid-state, magnetron, inductive output tube, traveling-wave tube, and klystron. Commercial counter-top microwave ovens often use a single magnetron due to simplicity and cost. Unlike the other examples, magnetrons are an oscillator and only require a high voltage input. Solid-state devices and many tubes require an additional oscillator and driver stages to drive the power amplifier stage and will increase the cost and complexity of the system. Recently, developments in III-V technology has enabled the fabrication of high efficiency, high power devices.

For initial testing of a small scale cavity, a 70 W power amplifier is designed to work at 2.45 GHz. The device chosen is the Qorvo QPD1015L. This device is capable of outputting 70 W up to 3 GHz while remaining at above 60 % efficiency and contains no prematching, enabling design at a wider range of frequencies compared to a prematched device. The design criteria for the device is fairly

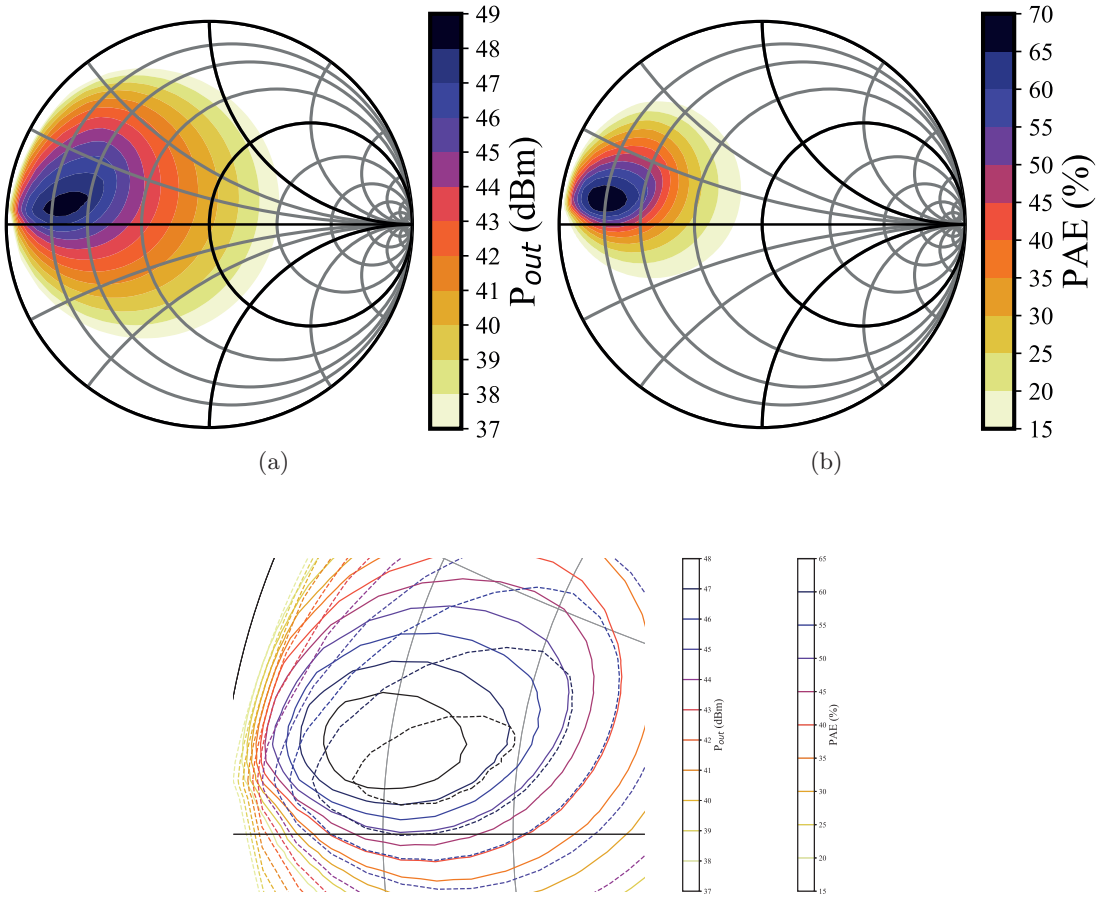

(a) (b)

(c)

Figure A.1: Loadpull contours at 2.45 GHz for a 65 mA Idq and 33 dBm input power showing (a) Pout, (b) PAE, (c) zoomed in contours where solid is PAE and dashed is Pout

relaxed as it is more of a proof of concept as opposed to the end design. The first goal was to design a reasonably high power, single-ended amplifier with greater than 60 % power added efficiency (PAE) in order to compete with the efficiency of a magnetron. Loadpull is done using a Modelithics model in AWR Microwave Office to determine the best gamma to obtain both high efficiency and high power output for class AB operation. This operating point is chosen as a low quiescent current will lead to greater efficiency and is also where the model is validated. The loadpull data can be seen for the fundamental in Fig. A.1 to have a small region of overlap with greater than 65 % PAE and 48 dBm (63 W) output power in Fig. A.1c.

To increase efficiency, a 0.1 pF capacitor is placed near the drain to improve the location of the

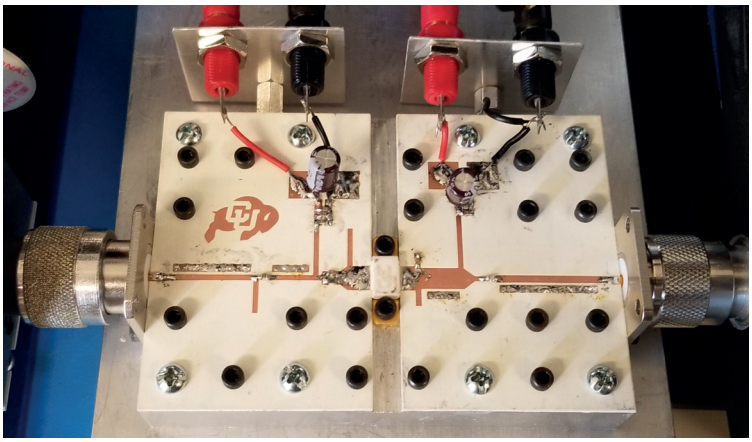

(a)

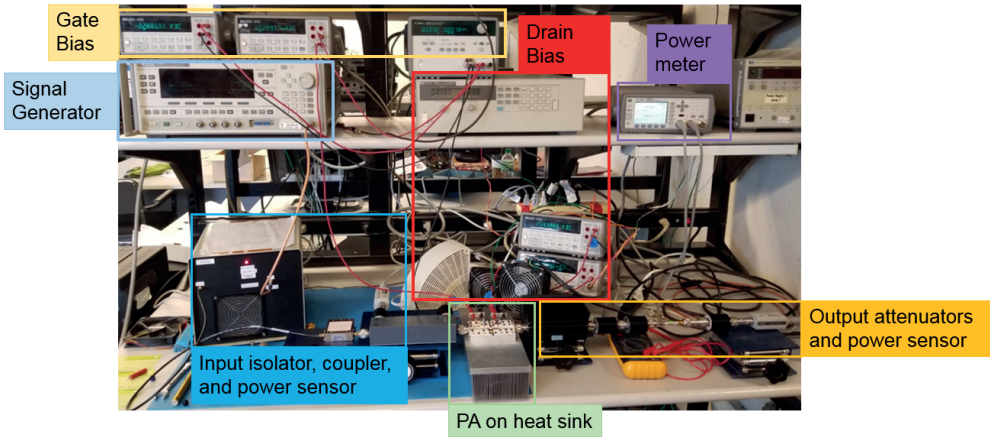

(b)

Figure A.2: (a) Fabricated power amplifier and (b) measurement setup.

second harmonic impedance. Wide lines are employed on the gate and drain of the same dimensions as the device to ensure an even current distribution on the gate and drain. The matching involves wide lines and stub matching as high bandwidth is not necessary. Additionally, a parallel RC circuit for stability is used on the gate to improve the low frequency stability. EM 2.5D simulations are performed using Axiem to simulate the coupling of close elements and the ensure that the circuit itself should perform properly when it is fabricated. The amplifier is fabricated on 32 mil thick Rogers 4360 (ε_r=6.4) in order to reduce the reduce the impedance of a line width matching the width of the gate and drain tab of the packaged amplifier. This also reduces the significantly, requiring a long line length to reach the end of a 10 cm aluminum heat spreader, however, the loss is low on this substrate (tanδ=0.0036) so the impact is fairly minimal. The extra line can be used

beneficially by adding extra lines shorted to ground are used on the input and output of the device in case tuning was necessary. This also enables more space for a mount for the gate and drain DC supplies to reduce the strain on the banana plug connectors.

The measurement setup is shown in Fig. A.2b. Each passive device is characterized using S-parameters and an input and output model over frequency is created in order to calibrate the setup. The setup is all controlled by GPIB such that the frequency and input power can be modified and then measured using the power meters. Performance of the power amplifier can be seen in Fig. A.4 to have about 2 dB lower gain at the desired operation frequency of 2.45 GHz. However, the amplifier is still able to reach 70 W output power at above 60% PA with an increase in input power. By shifting the frequency of the input signal, the amplifier begins to operate closer to the simulated expectation. In order to determine why this is the case, the return loss is measured using a network analyzer and shown in Fig. A.3d along with the simulated s-parameters.

The input match of the power amplifier has slightly shifted to a higher frequency, where the return loss at 2.45 GHz is now only about 5 dB. This can be somewhat corrected for by adding a small resistance (0.3 Ω) and inductance (0.15 nH) to the source of the device model. This effect can be physically seen and deviation was expected with the necessary addition of a small trench in the aluminum heatspreader. Due to the large package size, a cut in the aluminum was required to match the height of the RF substrate and the gate and drain tabs of the transistor. The extra path length between the RF ground of the substrate and the RF ground of the packaged device will result in some offset compared to the ideal simulation. In future designs, this can be accounted for as now the measured effect and be translated into an equivalent circuit.

Thermally, this device performs relatively poorly due to the small size of the . At the operating point of this device of 70 W and for 65 % drain efficiency, the dissipated power will be calculated by,

$$P_{diss} = \frac{1 - \eta_d}{\eta_d} P_{out} \tag{A.1}$$

to be 37.7 W. This dissipated power will result in a thermal resistance between the junction and

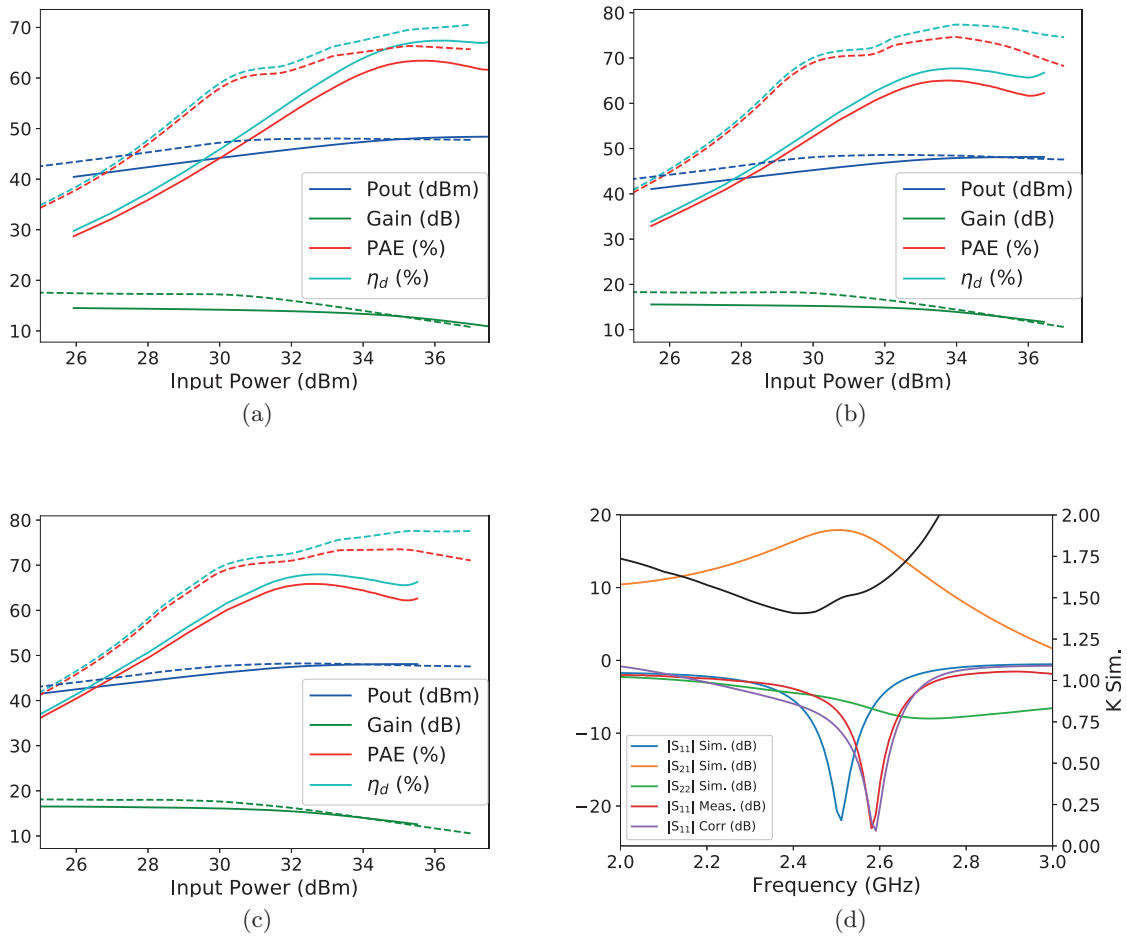

Figure A.3: 70 W power amplifier large signal parameters showing simulated (dashed) and measured (solid) for (a) 2.4 GHz, (b) 2.45 GHz, and (c) 2.5 GHz. (d) Small signal s-parameters simulated, measured, and input match corrected.

the case of 4.5 °C/W. To remain below the 250 °C reliability point, the case must remain at 80 °C. This point, however, will result in a lower maximum gate current, and as such, a lower operating power. For reasonable efficiencies this will not be a problem, however, it could lead to issues if gain drops or as the loading in the cavity changes.

To observe how the PA operates over CW operation, a Pico Technology TC-08 thermocouple datalogger is used to measure the temperature rise on the PA and heatsink and simulate the results with Ansys Mechanical thermal simulations. The setup, Fig. A.4a shows the location of the various thermocouples. These thermocouples operate on an internal 'cold junction' compensation to output

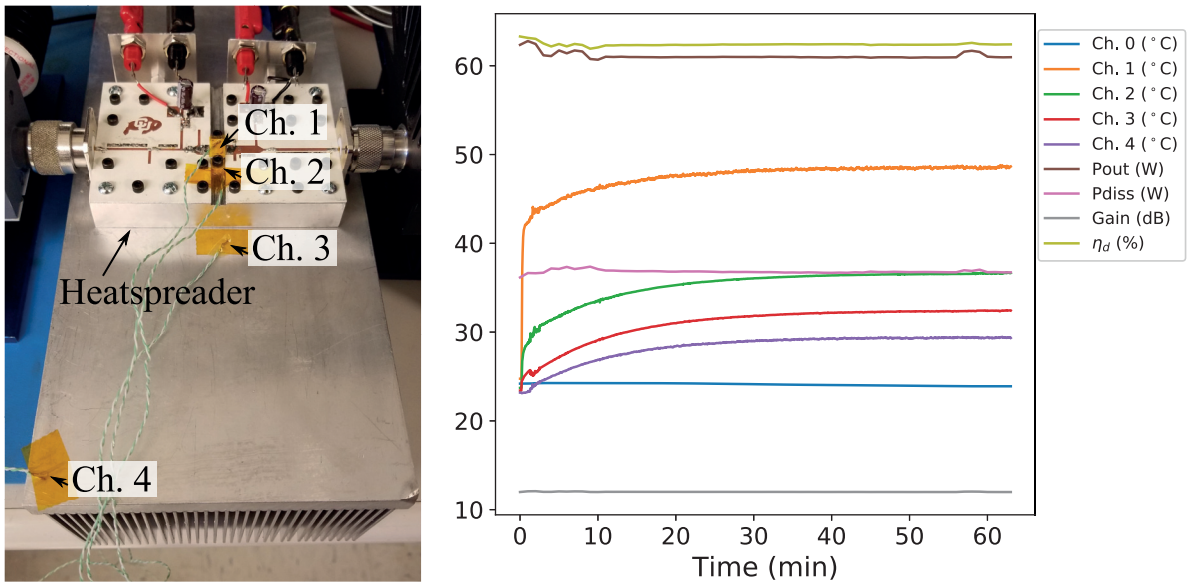

(a) (b)

Figure A.4: (a) Thermocouple setup and (b) temperature and power results over a 60 min test.

absolute temperature measurements based on the room temperature measurement of Ch. 0. The other channels are placed strategically on the power amplifier to observe the temperature gradient. The ceramic package is expected to become fairly hot due to the lack to heat sinking on the top of the package. The important thermocouple measurements are next to the flange on the package, the edge of the heat spreader, and the edge of the heatsink. The results, Fig. A.4b, show a relatively stable power performance after 10 minutes of heating, and reaches the maximum temperature after about 45 minutes of operation. The power amplifier was operated slightly in back off, which resulted in lower efficiency operation with still a high amount of power dissipated in the heatsink. Overall, this result shows temperature stability over time and gain flatness with enough heat dissipation on the power amplifier.

For a qualitative analysis of how the temperature changes over the entire board, infrared images are taken using an early version of FLIR Lepton camera (1.5) on a PureThermal 2 development board. The thermal images are shown in Fig. A.5 directly after turning on, after an hour, and a higher observation point. The resolution of the imaging camera is 80 x 60 pixels and requires a depth of field of 10 cm. Overall, the camera is able to image with a pixel resolution of 1.2x1.2 mm^2.

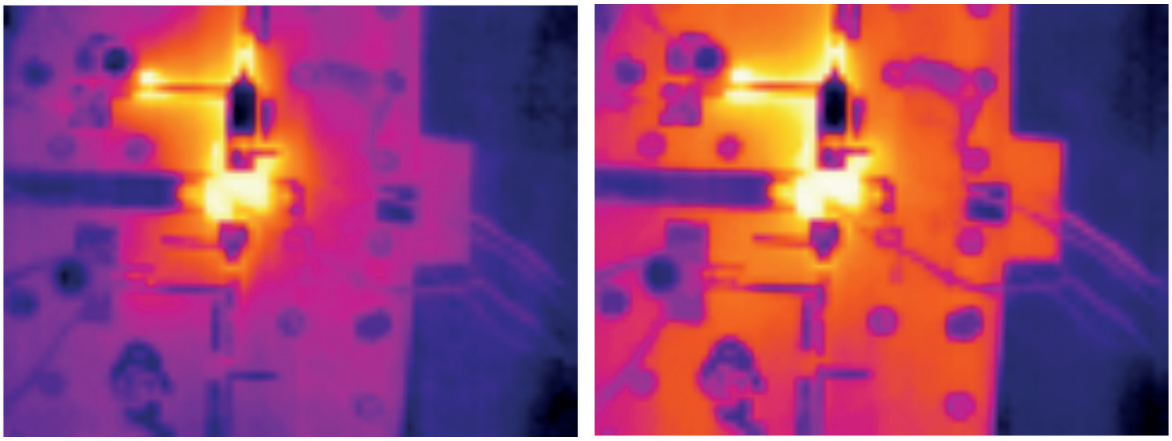

(a) (b)

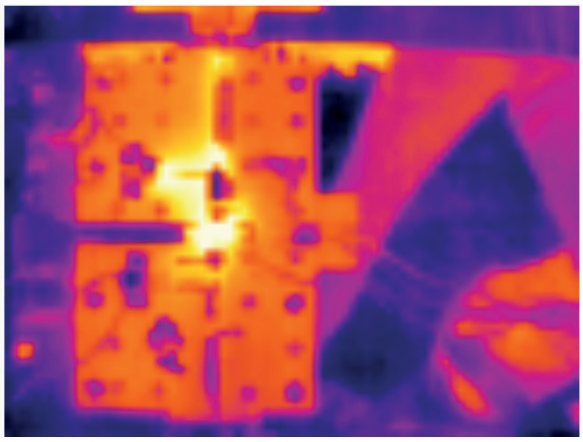

(c)

Figure A.5: FLIR Lepton thermal camera (a) immediately after turning the amplifier on, (b) after 60 minutes, and (c) after 60 minutes at a higher observation point.

The result is more qualitatively of interest as it does not factor in emissivity differences, as such, the metal conductor does not show a high temperature and the image is heavily post-processed and filtered with the dev-board provided software. Over time, the dielectric begins to heat due to the loss. Not surprisingly, the output matching network shows the highest temperature rise relatively quickly due to the large amount of current flowing through the network. Interestingly, the termination on the bias line to short the RF also becomes relatively hot fairly quickly due to loss in the capacitors and overall low resolution.